Hybrid Light Emitting Diodes and Photodetectors Using Polymers and Perovskites Via Electrospraying and Ink-jet Printing

by

Xiaohang GUO

THESIS PRESENTED TO ÉCOLE DE TECHNOLOGIE SUPÉRIEURE
IN PARTIAL FULFILLMENT FOR THE DEGREE OF
DOCTOR OF PHILOSOPHY
Ph.D.

MONTREAL, "AUGUST, 14, 2023"

ÉCOLE DE TECHNOLOGIE SUPÉRIEURE
UNIVERSITÉ DU QUÉBEC

BOARD OF EXAMINERS

THIS THESIS HAS BEEN EVALUATED

BY THE FOLLOWING BOARD OF EXAMINERS

Prof. Sylvain G. Cloutier, Thesis supervisor
Electrical Engineering Department, École de technologie supérieure

Prof. Nicole R. Demarquette, President of the board of examiners
Mechanical Engineering Department, École de technologie supériure

Prof. Ricardo Izquierdo, Member of the jury
Electrical Engineering Department, École de technologie supérieure

Prof. Ricardo Zednik, Member of the jury
Mechanical Engineering Department, École de technologie supérieure

Prof. Joshua Byers, External independent examiner
Chemistry Department, Université du Québec á Montréal

THIS THESIS WAS PRESENTED AND DEFENDED

IN THE PRESENCE OF A BOARD OF EXAMINERS AND THE PUBLIC

ON "JUNE, 27, 2023"

AT ÉCOLE DE TECHNOLOGIE SUPÉRIEURE

ACKNOWLEDGEMENTS

At the very beginning, I would like to thank my advisor Prof. Sylvain G. Cloutier for his excellent support, advice and guidance on both my PHD. study and daily lives. It would simply be impossible for me to complete this thesis without his help. Especially during COVID while I was stuck back in China.

I would like to thank my thesis committee members, Prof. Éric David, Prof. Vahé Nerguizian and Prof. Nicole R. Demarquette for sharing their valuable opinions and time upons finishing my thesis.

I would like to thank Dr. Xin Ma for her help on getting started with LED farbication and characterization; Dr. Debika Banerjee for her ideas and support on different projects; Dr. Jaime Benavides for his support on electrospraying setup and chemical related issues; Luis Felipe Gerlein for his support on many project and lab related matters including but not limited electroluminescent characterization, shadow mask fabrication and computer software and hardware supports; Dr. Charles Trudeau for his support on Raman characterization and inkjet printing; Ivy Mawusi Asuo for her support on perovskite materials synthesis; Arjun Wadhwa for his guidance on Ceradrop inkjet printer operation; François-Xavier Fortier for his support on circuit and characterization equipment setup, as well as writing Abstract in French; Nelson Landry for his support on project related materials purchases and characterization equipment setup; Alain Picard and Paul Fourmont for their knowledge sharing and creating a relax working environment.

In the end, I would like thank all my family members especially my parents and girlfriend for their mental support allowing me to leave them this long time to pursuit and fulfill my goals.

Diodes électroluminescentes hybrides et photodétecteurs utilisant des polymères et des via pérovskites

Xiaohang GUO

RÉSUMÉ

Cette thèse se concentre sur la fabrication de dispositifs optoélectroniques, y compris les DELs et les PD utilisant des matériaux hybrides organiques/inorganiques, notamment la pérovskite à trois cations, les polymères conjugués et le Si de type n par des techniques de fabrication d'enduction centrifuge, d'électrofillage et d'impression à jet d'encre.

Une revue de littérature approfondie explique les matériaux primaires (pérovskite, polymères), les dispositifs (LED, photodétecteurs), les techniques de fabrication (électrospraying, impression jet d'encre), les méthodes expérimentales et de caractérisation. Premièrement, pour la fabrication de dispositifs, les performances des DEL de pérovskite à trois cations par électrofillage ont été étudiées. Lors de la fabrication, des techniques de modification de la cristallinité ont été utilisées pour améliorer les performances du dispositif. Cependant, le dispositif émet une longueur d'onde spécifique à moins que le processus de cuisson ne soit modifié. Deuxièmement, des polymères conjugués conducteurs et fluorescents sont ajoutés pour modifier la longueur d'onde d'émission des DEL, et ce en contrôlant leur proportion. En raison des limites de la technique d'enduction centrifuge dans la formation d'une architecture multicouche, l'électrofillage a été implémenté pour surmonter ces difficultés. En utilisant l'électrofillage comme nouvelle technique de fabrication, des DEL à couleur réglable sont fabriquées et caractérisées. Même si l'électrofillage présente de nombreux avantages par rapport à l'enduction centrifuge, la stabilité du processus et son contrôle précis sont encore difficiles à atteindre. L'impression à jet d'encre pourrait être une méthode pour améliorer la technique de fabrication avec les avantages d'un contrôle de déposition de matériaux efficace, stable et précis. Enfin, des photodétecteurs à base de silicium fabriqué par la technique d'impression à jet d'encre sont démontrés. Dans l'ensemble, cette thèse représente une voie favorable vers la fabrication efficace et rentable de dispositifs optoélectroniques.

Mots-clés: DEL, pérovskite, polymère, électrofillage, impression à jet d'encre, photodétecteur

Hybrid Light Emitting Diodes and Photodetectors Using Polymers and Perovskites Via Electrospraying and Ink-jet Printing

Xiaohang GUO

ABSTRACT

This dissertation focuses on the opto-electronic devices fabrication, including LEDs and PDs using organic/inorganic hybrid materials including triple-cation perovskite, conjugated polymers, and n-type Si via spin-coating, electrospraying and ink-jet printing fabrication techniques.

Followed by an extensive literature review about the primary materials (perovskite, polymers), devices (LED, photodetectors), and fabrication techniques (electrospraying, inkjet printing), experimental and characterization methods are explained.

For device fabrication, firstly, we investigate the performances of the LEDs fabricated with triple-cation perovskite by spin-coating. During the fabrication, crystallinity modification techniques are used to improve the device performances. However, the emission wavelength is fixed for this kind of devices unless the perovskite cooking recipe is modified. Secondly, conductive and fluorescent conjugated polymers are introduced to alter the emission wavelength of the LEDs by controlling their ratio of mixture. Because of the limitations of the spin-coating technique in forming multi-layered architecture, we have implemented electrospraying to overcome such difficulties. Using electrospraying as the new fabrication technique, color-tunable LEDs are fabricated and characterized. Even though, electrospraying has many advantages compared to spin-coating, the stability of the electrospraying process and its precise control are still hard to achieve. Ink-jet printing could be a method to improve the fabrication technique with the advantages of material efficient, stable and precise control. In the end, silicon-based photodetectors fabricated by ink-jet printing are demonstrated.

Overall, this thesis represents a favorable route towards efficient and cost-effective opto-electronic device fabrication.

Keywords: LED, Perovskite, Polymer, Electrospraying, Ink-jet Printing, Photodetector

TABLE OF CONTENTS

LIST OF TABLES

LIST OF FIGURES

LIST OF ABBREVIATIONS

CCD	Charge-coupled Device
CIE	Commission Internationale de I’Eclairage
EHD	Electrohydrodynamic
EL	Electroluminescence
ETS	École de Technologie Supérieure
EQE	External Quantum Efficiency
ETL	Electron Transport Layer
DOD	Drop-on-demand
FWHM	Full Width at Half Maximum
GDM	Galvanic Displacement Method
GPIB	General Purpose Interface Bus
HF	Hydrogen Fluoride
HOMO	Highest Occupied Molecule Orbital
HTL	Hole Transport Layer
IV	Current-Voltage
LED	Light-emitting Diodes
LSP	Localized Surface Plasmon
LUMO	Lowest Unoccupied Molecular Orbital
NIR	Near Infrared Reflectance

OLED	Organic Light Emitting Diode
PDs	Photodetectors
PIV	Power-Current-Voltage
PLQY	Photoluminescence Quantum Yield
PVD	Physical Vapour Deposition
RGB	Red-Green-Blue
SEM	Scanning Electron Microscope
UV	Ultraviolet
UV-VIS	Ultraviolet–visible
XRD	X-ray powder diffraction

LIST OF SYMBOLS AND UNITS OF MEASUREMENTS

$CaTiO_3$	Calcium Titanate
$BaTiO_3$	Barium Titanate
MA^+	Methylammonium
FA^+	Formamadium
Cs^+	Cesium ion
$SrTiO_3$	Strontium Titanate
$MAPbI_3$	Methylammonium Lead Tri-iodide
$FAPbI_3$	Formamidinium Lead Iodide
$CsPbI_3$	Cesium Lead Iodide
Cl	Chlorine
Br	Bromine
I	Iodine
C	Carbon
TPD	N,N’-Bis(3-methylphenyl)-N,N’-diphenylbenzidine
Alq_3	Tris(8-hydroxyquinoline)
Mg	Magnesium
Au	Gold
Ag	Silver
Al	Aluminum

$DIWater$	Deionized Water
TFB	Poly(9,9-dioctylfluorene-alt-N-(4-sec-butylphenyl)-diphenylamine)
$F8BT$	Poly(9,9-dioctylfluorene-alt-benzothiadiazole)
$MEH-PPV$	Poly[2-methoxy-5-(2'-ethylhexyloxy)-1,4-phenylene vinylene]
PFO	Polydioctylfluorene
$PEDOT:PSS$	poly(3,4-ethylenedioxythiophene) polystyrene sulfonate
Ca	Calcium
Si	Silicon
$GaAs$	Gallium Arsenide
We	Weber Number
Re	Reynolds Number
Oh	Ohnesorge Number
THF	Tetrahydrofuran
$F8$	Poly(9,9-di-n-octylfluorenyl-2,7-diyl)
PEA	Phenethylamine
Rb	Rubidium
Pb	Lead
Sn	Tin
PbI_2	Lead(II) Iodide
$PbBr_2$	Lead(II) Bromide

FAI	Formamidinium Iodide
$MABr$	Methylammonium Bromide
MAI	Methylammonium Iodide
$DMSO$	Dimethyl Sulfoxide
DMF	N,N-Dimethylmethanamide
MoO_3	Molybdenum Trioxide
PPV	Poly-phenylenevinylene
THF	Tetrahydrofuran
Ge	Germanium
$PEDOT$	Poly(3,4-ethylene-dioxy thiophene)
Pt	Platinum
SiO_2	Silicon Dioxide
HF	Hydrogen Fluoride
HNO_3	Nitric Acid
N_2	Dinitrogen
HBr	Hydrogen Bromide
PI	Polyimide
PEN	Polyethylene Naphthalate
PET	Polyethylene Terephthalate

CHAPTER 1

INTRODUCTION

1.1 Organic-inorganic Halide Perovskite Materials

The term perovskite originates from a calcium titanium oxide mineral composed of calcium titanate ($CaTiO_3$) which was discovered in 1839 and named after the Russian mineralogist, L.A. Perovski [noa (m)]. Today, this name also applies to a class of compounds with the same crystal structure, such as $CaTiO_3$, with the general molecular formula ABX_3 [Wenk & Bulakh]. The perovskite is based on the A cations occupying the cavity in the center and corner-sharing of 8 (BX_6) octahedral as it is shown in Figure 1.1. Due to superconductivity and high ferroelectricity [Park], oxides (such as $BaTiO_3$ and $CaTiO_3$) are the most commonly studied perovskites [Johnsson & Lemmens]. In addition, a variety of cations can be embedded into this perovskite structure to accelerate the developments of diverse engineered materials [Szuromi & Grocholski].

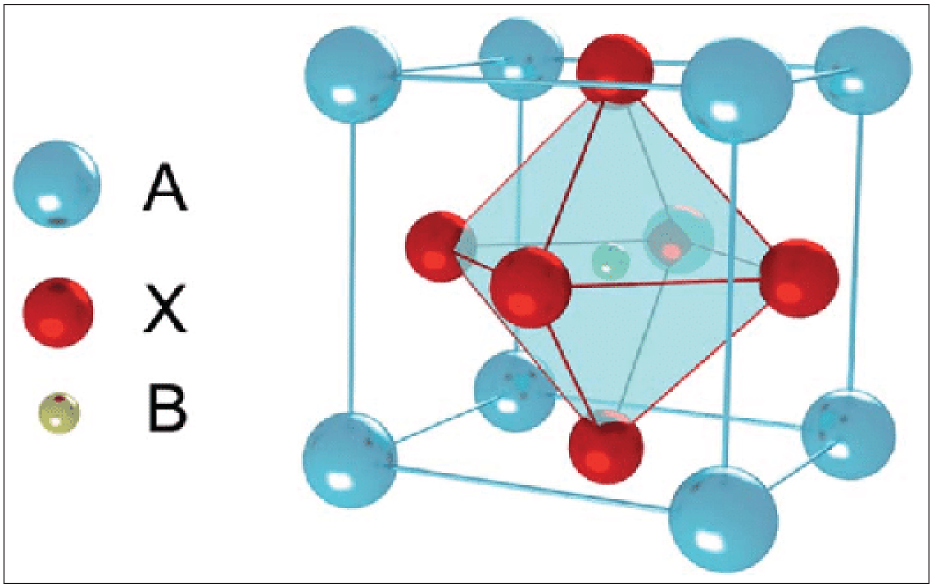

Figure 1.1 General perovskite structure with a formula of ABX_3. A site cation is surrounded by 8 (BX_6) octahedras [Chen *et al.* (d)].

For hybrid organic-inorganic perovskites, a cation or an organic molecular anion is introduced to replace one of the key building blocks [B. Mitzi] [Frost *et al.*]. Methylammonium-lead halides are one of the most commonly studied perovskites for the development of optoelectronic applications due to their solution-based process. The first organo-metal halide perovskite-based-photovoltaic cells were reported in 2009 [Kojima, Teshima, Shirai & Miyasaka] despite of the first synthesis of methylammonium-lead iodide perovskite was reported as early as 1938 [Weber].

Organic-inorganic halide perovskites are divided into organic type or inorganic type. Organo-metal halide perovskites are classified by the number of Site A cations, including single cation (A = Methylammonium (MA^+), $CH_3NH_3{}^+$, or A = Formamadium (FA^+): $CH(NH_2)$+ or Cs^+) [Jeon *et al.*] [Chen *et al.* (e)], double cation (A = MA^+ and FA^+ [Yang *et al.* (b)] or A = MA^+ and Cs^+ [Wu *et al.* (b)] or triple cation (A = FA^+, MA^+ and Cs^+) [Arora *et al.* (b)][Asuo *et al.* (a)]. The crystal geometry of the perovskite can be greatly influenced by the compositional engineering of the A site cation. The first study on the effect of the ionic size upon the perovskite crystal geometry was reported in 1926 [Goldschmidt]. In this study, the crystallographic geometry of the perovskite crystal (degree of distortion) is determined by the tolerance factor (t) which can be described by Equation 1.1 assuming pure ionic bonding.

$$a = \sqrt{2}\,(r_A + r_X) = 2\,(r_B + r_X) \tag{1.1}$$

The lattice parameter a in an ideal cubic perovskite can be represented by the equation below:

$$t = \frac{(r_A + r_X)}{\sqrt{2}\,(r_B + r_X)} \tag{1.2}$$

Where r_A, r_B, and r_X are the ionic radii of the A site cation, the B site cation, and the X anion respectively as shown in Figure 1.1. From Equation 1.2, the tolerance factor (t) can be directly influenced by the size of the $A - site$ cation. $SrTiO_3$ has an ideal cubic perovskite structure, where the tolerance factor (t) equals to 1 [Raengthon, McCue & Cann]. In general, perovskites with tolerance factors between 0.9 and 1.0 are treated as ideal cubic structures [Goldschmidt]. Slightly distorted perovskites due to tilted octahedra have tolerance factors between 0.71 and 0.9. While the tolerance factors below 0.71 and above 1.0, are labelled as none-perovskite structures [Goldschmidt]. This rule is developed for oxide perovskite; however, inorganic-organic hybrid halide perovskites are also valid [Stoumpos & Kanatzidis]. For inorganic-organic hybrid halide perovskites, they tend to form hexagonal structures ($t > 1$), cubic structures ($0.8 < t < 1$), and orthorhombic structures ($t < 0.8$). [Li *et al.* (b)]. Depending on the preparation techniques and temperature, more than one structure is usually discovered for a perovskite material.

Temperature can also affect the crystalline structure of the perovskite materials. For example, $MAPbI_3$ has a tetragonal structure even though its tolerance factor is 0.91 at room temperature (26.8^oC), and it turns to cubic structure when temperature exceeds 57^oC [Whitfield *et al.*][Breternitz, Tovar & Schorr]. $MAPbI_3$ is one of the most commonly used perovskite materials for optoelectronic device fabrications [Frolova *et al.*][Kim *et al.* (b)]. $FA/MA/Cs$ perovskites can crystallize into two different phases, non-photoactive non-perovskite hexagonal δ-phase (yellow phase) and photoactive perovskite α-phase (black phase) [Stoumpos, Malliakas & Kanatzidis][Eperon *et al.*][Lee, Seol, Cho & Park (c)]. The yellow phase impurities limit the charge collection by affecting the morphology and crystal growth of the perovskites that need to be avoided [Saliba *et al.*]. However, the tolerance factor can be altered to stabilize the photoactive perovskite α-phase (black phase) with suitable combinations of MA^+, FA^+ and/or Cs^+ cations [Dong, Wang & Liao (a)]. The success mixture of MA/FA indicates that small cation MA can act as a stabilizer for the black phase of the FA perovskites [Pellet *et al.*]. Comparing to the ionic radius of MA (2.70Å) and FA (2.79Å), Cs has the smallest of 1.81Å [Amat *et al.*]. Moreover, the incorporation of Cs into FA perovskite has shown improved structural stability and stimulated black phase crystallization because of the entropic stabilization [Yi *et al.*].

Despite many advantages of organic-inorganic halide perovskites, the stability due to the surrounding environment including light [Jung, Shin, Seo, Kim & Seok], heat [Conings *et al.*], oxygen [Aristidou *et al.*] and moisture [Han *et al.*], is highly critical for perovskite-based devices.

Moisture is the most important parameter for the perovskite degradation, while light, oxygen and heat will accelerate the moisture-induced degradation [Ahn *et al.*] because of the hygroscopic nature of the A site organic cations [Christians, Miranda Herrera & Kamat][Merdasa *et al.*]. Inorganic cations, such as CS^+ [Bella, Renzi, Cavallo & Gerbaldi] or Rb^+ [Zheng *et al.* (c)], can be used to reduce the moisture sensitivity. By adding CS^+ cations, other degradation mechanisms including bias-induced ion migrations, phase transitions, and light-induced trap state formations can be reduced[Bella *et al.*]. Tuning the X-site anion composition can also reduce the perovskite moisture-induced degradation [Boyd, Cheacharoen, Leijtens & McGehee]. For lead halide perovskite, the formation of H-halide bonds after the break up of lead-halide bonds is caused by the moisture-induced degradation [Svane *et al.*]. As higher energy is required for the formation of $H - Cl$ and $H - Br$ bonds comparing to $H - I$. As such, the addition of other halide anions such as Cl and Br can improve the perovskite stability against moisture [Noh, Im, Heo, Mandal & Seok]. What's more, different compositions and/or types of halides can also affect the optical bandgap of the perovskites causing tunable light emission for LED applications [Adjokatse, Fang & Loi]. It is because the orbitals of the halide ions can affect the perovskite valence- and conduction-band positioning [Adjokatse *et al.*]. Therefore, halides with different ionic radii would principally change the perovskite bandgap [Umebayashi, Asai, Kondo & Nakao]. Figure 1.2 shows an image of perovskite $CsPbX_3$ nano-crystals with different colors suggesting different bandgaps based on different compositions of $X = Cl, Br, I$.

1.2 Conductive Fluorescent Polymer Materials

Highly conductive and fluorescent polymer materials joined the OLED materials family shortly after the discovery of the first OLED based on small molecules [Tang & VanSlyke]. Polymer, as a small molecule material, its conductivity is based on the p-orbital conjugation induced de-localization of the electron-wave function as in Figure 1.3a [noa (a)][Ma]. Compared to the low solubility of the small molecules in solvents, long polymer chains attached with different side groups can be easily dissolved in the solvent [Kumar & Sharma]. Therefore, solution deposition techniques including spin-coating and ink-jet printing could be used in thin film fabrication.

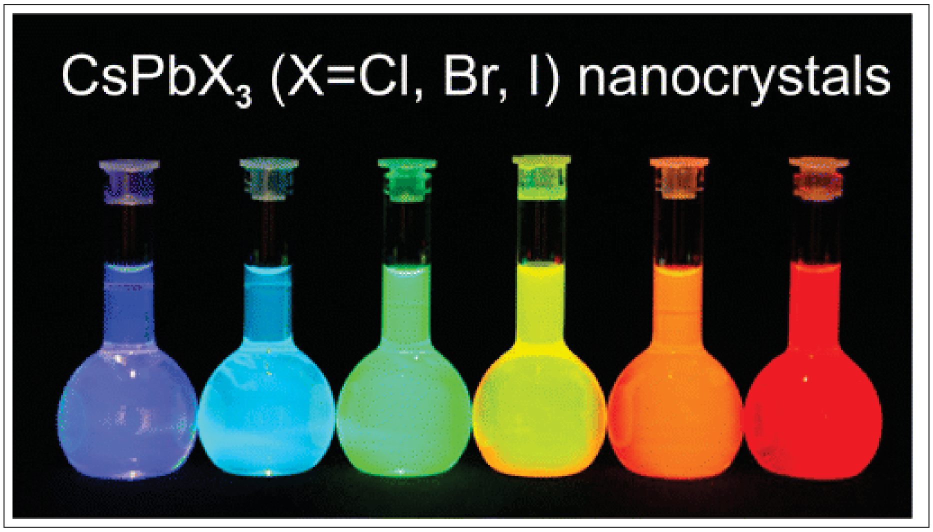

Figure 1.2 Images for color tunable colloidal $CsPbX_3$ nano-crystals [Protesescu *et al.*].

Solution deposition techniques can be used for industrial manufacturing based on their low cost and large-area scalability. Moreover, ink-jet printing is a low-cost and easy-patterning technique that avoids those complicated and costly patterning processes, including shadow masking and lithography. The possibilities of tailoring the electrical and mechanical properties and emission wavelength of the conjugated polymers by changing their side chains [Cacialli *et al.*], cross-linking various monomers [Veinot & Marks] and/or forming polymer networks are also very attractive for optoelectronic devices fabrication [Pérez–Gutiérrez *et al.*].

The basic structure of the semiconducting or conducting organic materials is shown in Figure 1.3b [noa (l)]. The essential structure is a continuous series of double bonds that fills the length of the molecule, and a molecule containing this structure is called "conjugated" [Ma]. Each C atom in the backbone has a half-filled p-orbital for pi bonding [Ma]. Additionally, each C atom also has one available bond for functional group attachment which brings high adjustability to the conjugated polymers. The optical and electrical properties of the conductive polymers are determined by the gap between the lowest unoccupied molecular orbital (LUMO) and the highest occupied molecular orbital (HOMO) [Waltman, Bargon & Diaz][Brédas, Heeger & Wudl]. Besides the linear chain structure, the aromatic ring is another form the p-orbital conjugation

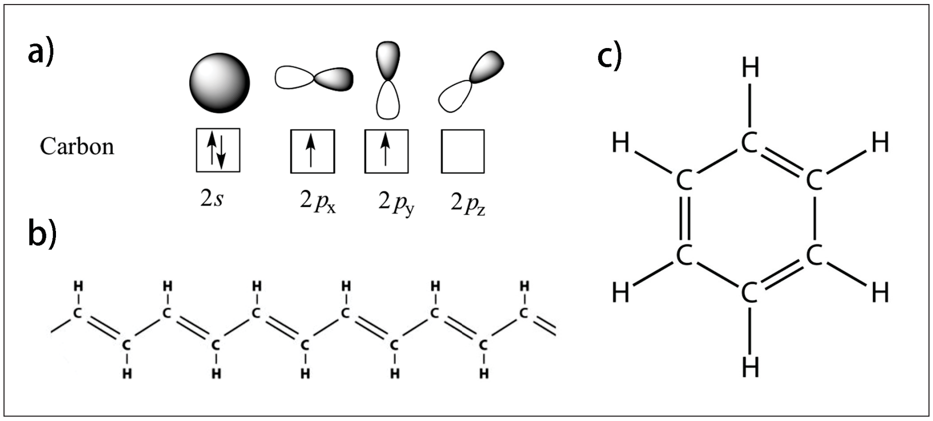

Figure 1.3 Description of conjugation in organic polymer. (a) Electron orbitals of a single carbon atom [noa (a)]. (b) Conjugated carbon chain [noa (l)]. (c) Aromatic carbon ring [noa (u)].

as it is shown in Figure 1.3c [noa (b)]. Both structures offer good conductive properties to the polymers; however, aromatic ring formation has weaker chain distortion providing more efficient dielectric transitions between HOMO and LUMO. Therefore, aromatic rings-formed polymers have higher fluorescence efficiency [roc].

The half-filled neutral dangling bond is highly reactive [Gardos]. If an original electron is removed from the dangling bond, it leaves a hole. On the contrary, if a dangling bond accepts an electron, an origin electron would be left behind resulting in a negative charge in this segment of the polymer [Zhang & Wei]. The current is formed in the polymer films because these formed charges can diffuse along the polymer backbone or jump to another chain [Ma]. Exciton, a basic energy state of a pair of electron and hole bonded by electrostatic Coulomb force, is formed when a hole and electron meet together. In general, polymers have much stronger exciton binding energies comparing to inorganic materials because of related chain distortion separating electron-hole pairs in the polymer [Blom, Mihailetchi, Koster & Markov (b)]. For polymer materials, it is harder to separate electron-hole pair once an exciton is formed making them more applicable for light-emitting applications rather than photovoltaic devices. Excitons in conductive and fluorescent polymers can be generated by either electron excitation or photon excitation [Morteani, Sreearunothai, Herz, Friend & Silva]. Electron excitation is the carrier injection from metal electrodes and photon excitation is the absorption of photon energy higher than the energy gap [Morteani *et al.*]. The formed excitons can be decayed radiatively, resulting in electroluminescence and photoluminescence or non-radiatively causing energy loss as heat [Morteani *et al.*]. The formed excitons can also be dissociated to free electrons and holes in the polymer or transferred to another organic or inorganic material nearby [Morteani *et al.*]. For LED design, radiative exciton decay should be maximized to achieve high efficiency.

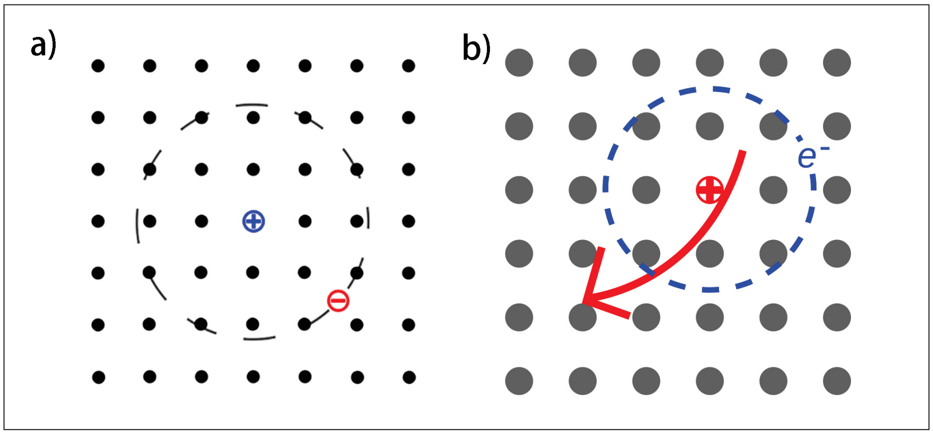

Figure 1.4 Exciton spatial distribution in different materials [noa (e)] . The "+" and "-" symbols in the figure represent "electron" and "hole" respectively. (a) Frenkel exciton in organic material. (b) Wannier-Mott exciton in inorganic semiconductor materials.

HOMO/LUMO levels in organic materials can be generally considered equivalent to valence band maxima and conduction band minima in solid-state physics [Sze & Lee]. Nonetheless, organic and inorganic materials have tremendous differences in carriers, exciton transports, and mechanical properties because of their bonding states in the material matrix. For polymer materials, the charged carriers only interact with the nearest repeating unit on the polymer chain [Köhler *et al.*]. This weak interaction along the polymer chain is not sufficient to form a real energy band as in an inorganic periodic lattice structure; therefore, polymer materials generally have lower carrier mobilities [Köhler *et al.*]. In addition, the carrier mobility in polymer materials is further lowered by the disordering of HOMO/LUMO levels and local trappings of the lower energy states [Pope & Swenberg]. As for exciton properties, polymer materials have high binding energies due to the chain distortion and low electron screen effect [Zhu, Yi, Chen & Shuai (a)]. Excitons with strong bonding energy 0.1 to 1 eV are referred as Frenkel excitons [Pope & Swenberg]. On the contrary, the electron screen effect in organic materials reduces Coulomb interactions causing their exciton binding energies on the order of 0.01eV which is referred as Wannier-Mott excitons [Wannier]. Figure 1.4 shows schematics of Frenkel and Wannier-Mott excitons respectively [noa (e)]. At last, for the mechanical properties, polymer materials have weaker van der Waals bonds between chains resulting in soft and flexible characteristics offering great substrate compatibility even for flexible substrates [Ma].

1.3 Semiconductor LEDs

In modern society, light sources are one of the most important electronic components taking part in many aspects including general lighting, telecommunications, sensors, displays, remote control, and so on [Nardelli, Deuschle, de Azevedo, Pessoa & Ghisi]. Based on the light source type, today's market is divided into compact fluorescent lamps (CFLs), incandescent, halogens, and light emitting diodes (LEDs); among which the LEDs segment is expected to have the highest growth rate [noa (h)]. This growth is attributed to its rapid growth in applications with advantages of low energy consumption, small size, long lifetime, fast switching speed, and low cost [Massa, Kim, Wheeler & Mitchell][Baleja *et al.*].

The semiconductor LED was first reported in the 1920s by Lossev based on the discovery and understanding of semiconductor materials and properties [Lossev]. The working mechanism of semiconductor LEDs is essentially the light emission by radiative recombination of electrons and holes within the semiconducting materials [Sze & Lee]. During the device operation, electrons (injected from the cathode into the n-type semiconductor) and holes (injected from the anode into the p-type semiconductor) meet at the interface of the junction and recombine to emit light. To facilitate such electron & hole injection and spatially confine the recombination process, forming a depletion region at the interface between n-type and p-type semiconductors is important [Ma].

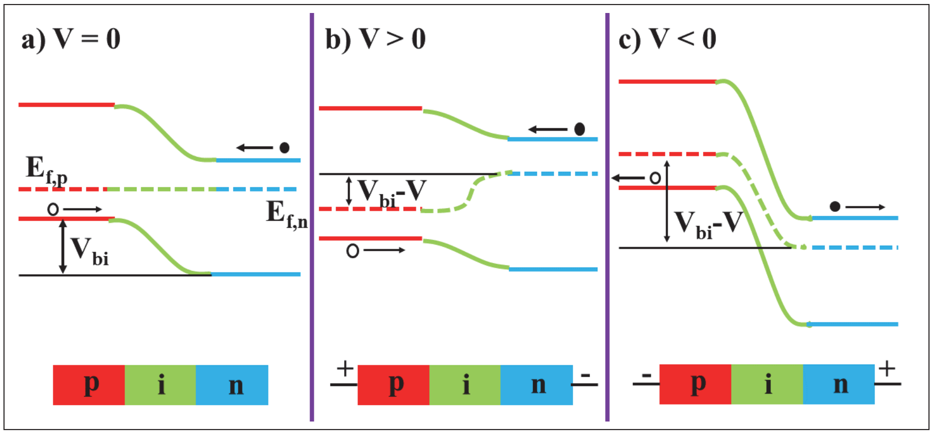

Figure 1.5 $P - i - n$ junction. (a) no applied voltage, (b) forward applied voltage, (c) reverse applied voltage. Adapted from [Sze & Lee]

Figure 1.5 shows schematics for a typical $p - i - n$ junction for semiconductor materials under equilibrium, forward bias and reverse bias respectively. When the device is under thermal equilibrium, the Fermi levels of the p and n-doped materials are aligned. Under the forward bias (Figure 1.5), the current-density versus voltage ($J - V$) characteristics in the log scale can be classified into 3 regimes, such as leakage (I), diffusion (II), and drift (III) current regime as it is shown in Figure 1.6 [Lv *et al.*]. In region (I), the current density is linearly dependent on the applied voltage. When the applied voltage is smaller than the built-in potential (V_{bi}), the diffusion current regime is entered because charge carriers are diffusely attracted by the concentration of the opposite carriers. The diffused current is described by the Shockley diode equation [Sze & Lee]:

$$J = J_0 \left[\exp\left(\frac{qV}{\eta kT}\right) - 1 \right] \tag{1.3}$$

Where J_0 represents the saturation current, q is the electron charge, k is the Boltzmann's constant, T is the temperature, V is the applied voltage and η is the exponential ideality factor.

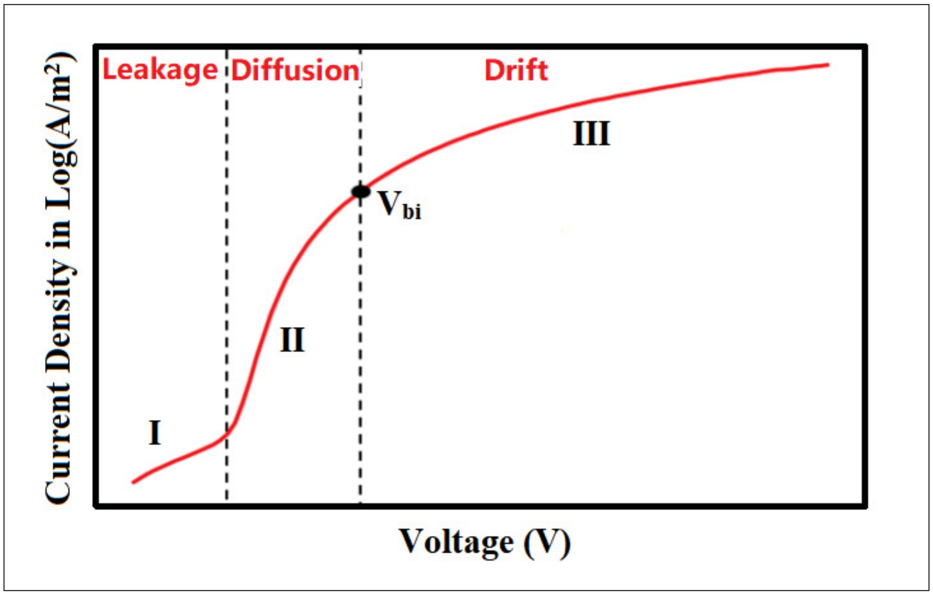

Figure 1.6 Regimes for diode under forward bias. The y-axis is the log10 scale of the current density. Adapted from [Lv *et al.*]

When the applied voltage exceeds the V_{bi}, drift current is created and it is space-charged limited. It is because the relatively low carrier mobility of the organic materials limits the carrier flow under high voltage. As last, no current flows through the junction under reversed bias.

In general, the emission wavelength of the semiconductor LED mainly depends on the bandgap of the semiconductor material. Despite of the advantages, inorganic semiconductor LEDs manufactures are limited by the low throughput and high cost of epitaxial growth in the commercial market. Nowadays, novel conductive, fluorescent organic materials and organic-inorganic perovskites have promoted semiconductor LEDs into a completely new era [Ma]. Conjugated polymers and perovskite materials could offer a wider emission spectrum, a much lower cost, a more flexibility on substrate requirements, and ink-jet printability; many of which are beyond the conventional semiconductor-based technologies [Braun] [Wei *et al.* (b)].

1.3.1 Perovskite LEDs

The first organic electroluminescent device has a single-layer architecture which consists of a small molecules layer sandwiched between two electrodes [Bernanose, Comte & Vouaux][Bernanose]. In 1987, the first practical OLED structure was reported where a multi-layer structure is developed, which is hole transport layer (HTL), TPD, and emissive electron transport layer (ETL), Alq_3, are sandwiched between transparent ITO anode and Mg cathode [Tang & VanSlyke]. Multi-layer structures have many advantages against single-layer structures: 1) improve the carrier transportation by reducing the device resistance, 2) balance the electron and holes injection, 3) confine the electron and holes in the emissive layer by implementing electron and holes blocking layers, and 4) reduce the exciton quenching rate by restricting the recombination region away from the metallic cathode [Nuyken, Jungermann, Wiederhirn, Bacher & Meerholz]. OLEDs are multilayered devices with their luminescent material sandwiched between electron and hole injection layers. Electroluminescence is the process of the radiative recombination of the charge carriers in the emissive material; a p-n junction is formed when negatively and positively doped semiconducting materials are brought into contact [Geffroy, le Roy & Prat]. Perovskites have features belonging to both organic and inorganic semiconductors. Organometal/metal halide perovskites have undergone remarkable developments because of their excellent electrical and optical properties, including tunable bandgap, high charge-carrier mobility, high photoluminescence quantum yield and long free-carrier diffusion length, and solution-processability [Van Le, Jang & Kim][Chen, Zhou, Jin, Li & Zhai (b)][Zhang, Eperon & Snaith (b)][Li *et al.* (c)]. After the successful of using perovskite materials in solar cell fabrication, their excellent properties also facilitate the developments for high efficient LED applications.

Generally, the structure of a perovskite-based LED (Figure 1.7a) is: anode/HTL/perovskite/ETL/cathode where at least one electrode is required to be transparent for light emission [Guo *et al.* (a)]. When a bias voltage is applied, holes injected from the anode through HTL and electrons injected from the cathode through ETL are radiatively recombined at the perovskite layer. Figure 1.7b represents an ideal energy band-diagram of a typical

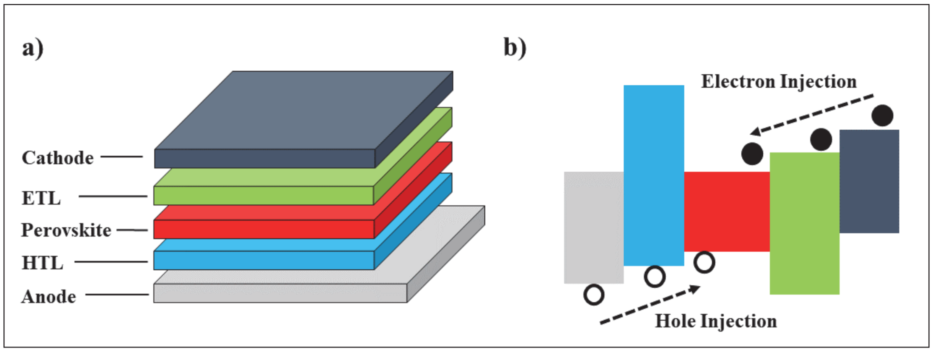

Figure 1.7 (a) Schematic for the general perovskite based LED structure. (b) An ideal energy band-diagram Guo *et al.* (a).

perovskite-based LED [Guo *et al.* (a)]. Proper values for $HOMO$ and $LUMO$ levels need a carefully design, so that there are no barriers during the charge injections. Additionally, large barriers are necessary for holes at $perovskite/ETL$ and electron at $perovskite/HTL$ interfaces respectively [Pan, Shao, Zhang, Shen & Wang (a)]. Therefore, HTL and ETL can act as blocking layers preventing holes from entering the cathode and electrons entering the anode. As a result, electrons and holes are confined within the perovskite film which can significantly increase the carrier recombination rate [Pan *et al.* (a)]. Both inorganic and organic materials can be used as ETL and HTL. Some of the common materials for ETL and HTL and their $HOMO$ and $LUMO$ values can be found in Figure 1.8 [Fang *et al.*]. As for the materials of the electrodes, gold(Au), silver(Ag), copper (Cu), and aluminum (Al) are commonly used as metal electrodes. FTO and ITO, graphene, carbon nanotubes, ultra-thin metal films, and nanowire mesh are the common conductive and transparent electrodes [Cao, Li, Chen & Xue].

1.3.2 Polymer Based LEDs

Ever since the first successfully demonstration of conjugated polymer light emitting diodes (PLEDs) in 1990 [Burroughes *et al.*], PLEDs have attracted tremendous attentions for new generations of low-cost solid state lighting, due to their unique advantages including solution-based fabrication process, high power efficiency, large area scalability and high flexibility [Ma

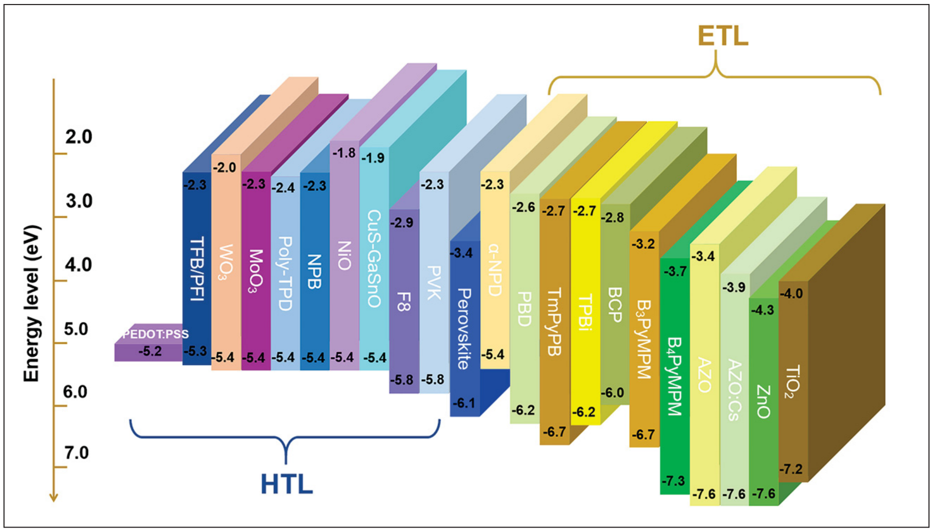

Figure 1.8 Energy levels of some common HTL and ETL materials for perovskite based LED Fang *et al.*

et al.]. In order to achieve a high efficiency for polymer based LEDs, a multilayer structure is generally inevitable [Kasparek & Blom]. However, multilayer architectures can be achieved easily through spin-coating for perovskite-based LEDs; however, it is a lot harder to achieve such structures for polymer-based LEDs. It is because the conjugated polymers generally have similar solubility in common organic solvents; therefore, the deposited bottom layers will often be dissolved and then blended with the layer atop, destroying the multilayer architecture. PPV is one of the few polymers that can be used in fabricating multilayer polymeric structures [Lee *et al.* (c)]. It becomes insoluble after high-temperature thermal annealing by forming a cross-linked network; thus, further solution deposition atop of PPV is feasible [Lee *et al.* (c)]. Unfortunately, most conjugated polymers are sensitive to annealing temperature creating additional difficulties in fabricating multilayer structures even by using PPV [Lee *et al.* (c)].

Given the many difficulties associated with multilayered polymer LED fabrication, polymer blends are mostly used where good device performances can be achieved by controlling the phase separation in polymer blends [Ma *et al.*] For polymer-based photovoltaic devices, the small domain size is preferred because richer heterojunction interfaces could improve the chance for exciton dissociation before they recombine radiatively [Lee *et al.* (a)]. On the contrary, large domain suits better for LED devices due to in-time carrier recombinations before dissociating to the interfaces of other domains [Ma *et al.*]. Since the diffusion length of an exciton is on the order of approximately $10nm$ for the polymers generally used for LED fabrication, phase separation greater than this range is beneficial in preventing exciton from breaking-up at the interfaces before recombination for blended polymer LED applications [Mikhnenko, Blom & Nguyen].

Due to the relatively low electron mobilities of the conjugated polymer materials, the I-V characteristics of such devices are usually bulk-limited other than injection-limited at low driving voltage [Blom *et al.* (b)]. Bulk-limited refers to the metal contact as the main limiting factor for the current flow [Chiu (2014)]. When carriers are injected into the polymer thin-film, the formation of the built-in electromagnetic field would interfere with later carrier injections [Chiu (2014)]. The polymer field-dependent carrier mobility is also a factor in describing the current densities in polymer-based LEDs [Kabra, Lu, Song, Snaith & Friend]. Combining Mott-Gurney Law with field-dependent mobility, a device with single carrier injection can use the simple device I-V model [Kabra *et al.*]:

$$J_{SCLC}^{PF} = \frac{9}{8}\varepsilon\mu_0\frac{V^2}{L^3}\exp\left(\beta\frac{V}{L}\right) \tag{1.4}$$

Where J_{SCLC}^{PF} represents the current density, μ_0 is the carrier mobility at zero fields, ε is the permittivity of the polymer which can be calculated by $\varepsilon = \varepsilon_0\varepsilon_r$, β is the field effect mobility coefficient and it depends on the trap depths in the organic semiconductors [Kabra *et al.*], L is the polymer film thickness and V is the applied voltage..

The general structure, working mechanism, and energy level of a PLED are illustrated in Figure 1.9. When a bias voltage is applied, electrons and holes are injected from the cathode and anode to the polymer layer by overcoming the barriers of the interfaces. The electrons move towards $LUMO$ of the ETL while the holes move towards $HOMO$ of the HTL. Then the external electrical field-motivated charge carriers are transported toward the emission layer for recombination. Finally, the formed excitons jump from the excited state to the ground state resulting in light emission in the emissive layer (EL), Figure 1.9a [Peng, Sun, Weng & Fang]. The emission color of a PLED depends on the energy differences between the LUMO and HOMO of the fluorescent polymer materials. The emission color can be tuned covering the entire visible spectrum by changing or mixing the active polymer materials [Guo][Tasch *et al.*]. Table 1.1 shows HOMO, LUMO, and function values for some commonly used light-emitting polymer and electrode materials .

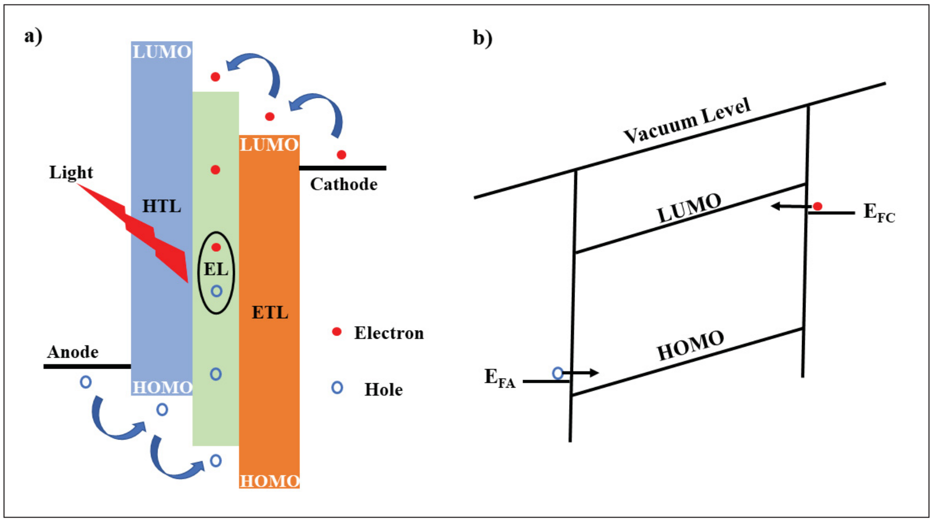

Figure 1.9 (a) Schematic of PLED structure and its illustration towards the working mechanism. (b) PLED's energy level

Table 1.1 HOMO, LUMO and work function values for some common light emitting polymer and electrode materials, adapted from Santos & Gozzi

Materials	**LUMO (eV)**	**HOMO (eV)**	**Emission Color**	**Work Function (eV)**
TFB	2.3	5.3	blue	-
F8BT	3.3	5.9	green	-
MEH-PPV	3.0	5.3	red	-
PFO	3.0	5.8	-	-
ITO	-	-	-	4.7 4.8
Ca	-	-	-	2.87 3.0
Al	-	-	-	4.06 4.41
Au	-	-	-	5.1 5.47
Ag	-	-	-	4.26 4.74

Forming Ohmic contact between the electrodes and the polymer layers, and balanced charge carrier injection are important for effective carrier injection and transportation [Sze & Lee]. It is crucial for achieving high luminous efficiency and low driving voltage. An interface contact can be called an Ohmic contact refers to the well match between metal work function and organic material energy level. [Sze & Lee]. However, it is generally hard to form a good Ohmic contact between the electrode and the organic semiconducting material because of the present of mismatch [and & and]. There are two possible ways to make a metal-semiconductor contact closer to an ohmic contact, narrower the barrier and/or lowering the barrier height [noa (k)]. An ohmic contact is attractive for optoelectronic devices including LEDs, solar cells, and photodiodes [Campbell, Bradley & Antoniadis]. However, the situation is rather complicated for LEDs. It is because both positive and negative charge carriers need to be balanced when they are injecting into the emissive region; as well as the recombination zone needs to be away from the cathode to avoid exciton quenching [Bradley][Grüner, Remmers & Neher]. The mobilities of positive and negative carriers, mu_p and mu_n, are invariably different (generally mu_p » mu_n); The charge distribution can be strongly influenced by the flow of carriers of one sign to that of carriers of the opposite sign [Redecker, Bradley, Inbasekaran & Woo][Malliaras & Scott]. Using multilayer device with a range of carrier mobilities and/or internal barriers are the solutions [Nakazawa *et al.*][Giebeler, Antoniadis, Bradley & Shirota]. A two-layer device using polymers with different ionization potentials can buildup the positive carriers at the internal interface, forcing the emissive region away from the cathode; therefore, the negative carrier transport is improved by making most applied bias fall across the polymer layer beneath the cathode [Campbell *et al.*]. If one type of charge carrier (electrons or holes) is outnumbered, the interactions between excitons and excess charge carriers can lead to nonradiative recombination resulting in lower efficiency [Hung & Chen]. There are several techniques to improve the charge-carrier balance, such as optimization of charge-carrier selective contacts (e.g., modification by additive doping [Chen *et al.* (c)], optimization of post-annealing process [Shao, Xiao, Bi, Yuan & Huang] or utilization of innovative materials [Li] and incorporation of carrier selective contacts [Malinkiewicz *et al.*] [Yuan *et al.*].

The process of transferring charges from high to low conductive material is called charge carrier injection [Sze & Lee]. When the mobility of the charges in the organic material is low, the current is limited by the intrinsic properties of the material itself. It is called the space charge limited current[Sze & Lee]. Figure 1.9b represents the energy level diagram of a PLED. E_{FA} and E_{FC} describe the Fermi level of the anode and cathode respectively. The work function is defined as the difference between the Fermi level and vacuum level [Sze & Lee]. Generally, the Fermi level lies below the $LUMO$ and above the $HOMO$ where it creates an energy barrier [Sze & Lee]. When a bias voltage is applied and increased further, the $HOMO$ ($LUMO$) of the organic semiconducting material would become more and more bent so that more carriers (electrons, holes) can pass through until the applied voltage is way too high to break the device [Sze & Lee].

1.4 Photodetectors

The Photodetector is one of the critical components in optoelectronic devices. Digital processing carrying valuable information requires fast and efficient light detection (X-ray to infrared). Nowadays, photodetectors comprise an enormous market (1.3 billion US by year 2026) [ReportLinker] and their applications include but not limited fibre-optic communication, remote sensing, spectroscopy, images and many others [Zhao, Xu, Niu, Zhang & Zhang (d)]. A photodetector (PDs) is an optoelectronic device that converts incident light or other electromagnetic radiation in the infrared, visible, and UV spectral regions into electrical signals [Nguyen, Luong, Pham, Nguyen & Dang (b)].

Photodetectors are generally divided into two categories: thermal- and photo-detectors [Rogalski]. Thermal detectors detect thermal radiation and generate photocurrent due to either change in device temperature or resistance [Downs & Vandervelde]. The physical principle of the photodetector is the generation of the photovoltage or photocurrent within the device which can be processed further by readout electronics upon the absorption of light [Zhao, Li & Shen (c)]. Many factors can influence the efficiency of a photodetector, such as charge extraction, charge carrier separation & transport, and optical absorption [Keivanidis, Ho, Friend & Greenham].

1.4.1 Photodetector Structures

Typically, a Photodetector has a vertical configuration. Generally, incoming light is first traveling through the detection layer on the top of the device as shown in Figure 1.10a. However, there are some cases where the incident light passes through the substrate initially and the detector layer at the end (Figure 1.10b). For this kind of device, the substrate should be thin and transparent to improve the light absorption of the device. For both top or bottom illuminated devices, incident light must be easily coupled into the photodetector active area [Kimukin].

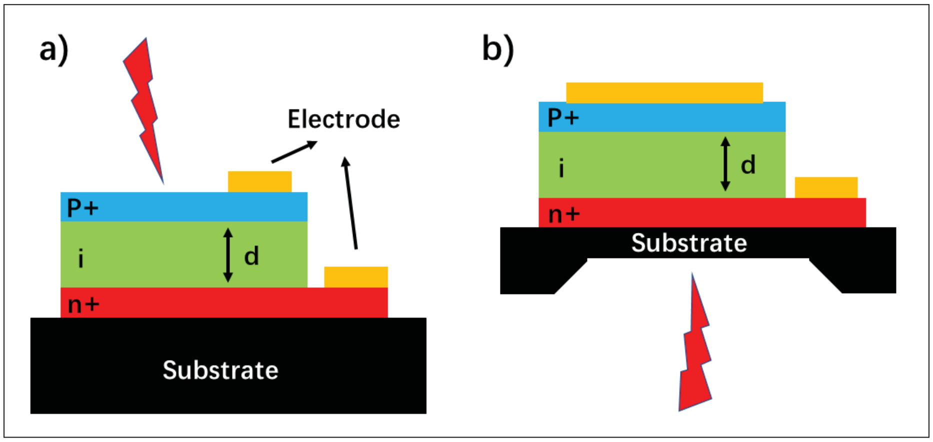

Figure 1.10 Cross-section of the vertical configuration of the photodetector under illumination, adapted from [Kimukin].

In addition to the vertical configuration, illumination from the edge of the device is another possible architecture (Figure 1.11). For this configuration, coupling of the incident light through a waveguide is the key. The small thickness of the waveguide is required for its operation in the single mode [Kimukin]. During the operation, electron and hole pairs are generated as the coupled light traveling along the waveguide. Longer length is preferred for maximum power absorption in the waveguide and the loss due to the contact metal absorption must be minimized [Kimukin].

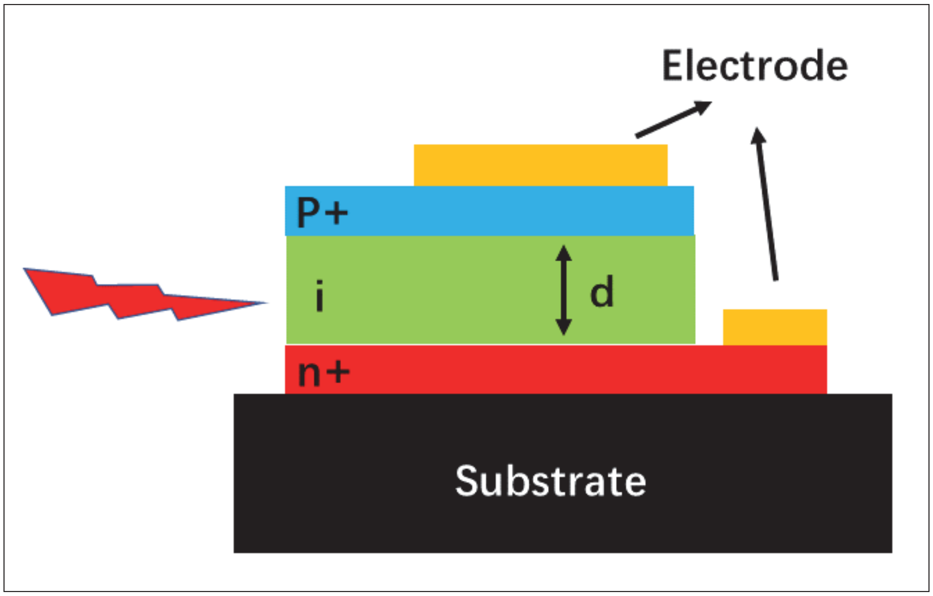

Figure 1.11 Cross-section of the edge configuration of the photodetector under illumination, adapted from [Kimukin].

1.4.2 Photodetection Mechanism

A photodetector contains a high electric field depleted region [Sze & Lee]. Charged carriers are generated inside the depletion region when photons are absorbed. The photogenerated electron/holes travel along the opposite directions until they recombine or reaching a highly doped contact layer [Kimukin]. A potential difference is created while the charges move across the depletion region, which induces a current flow in the circuit when the photodetector is connected. The resulting current density is proportional to the incident optical power [Sze & Lee]. At zero bias, an ideal photodetector has a low power dissipation with minimal dark current, Figure 1.12. Whereas, photodetectors typically operate at reverse biases. Under reverse bias, the current will only flow through the circuit when there is incident light applied. Its typically IV characteristic (red curve) is shown in Figure 1.12.

Most popular ways of forming the depletion region are the metal-semiconductor and $p-n$ junctions [Kimukin]. Photodetector using a $p-n$ junction is called a $p-i-n$ photodetector. Its energy band diagram is shown in Figure 1.13. In this architecture, a lightly doped layer is

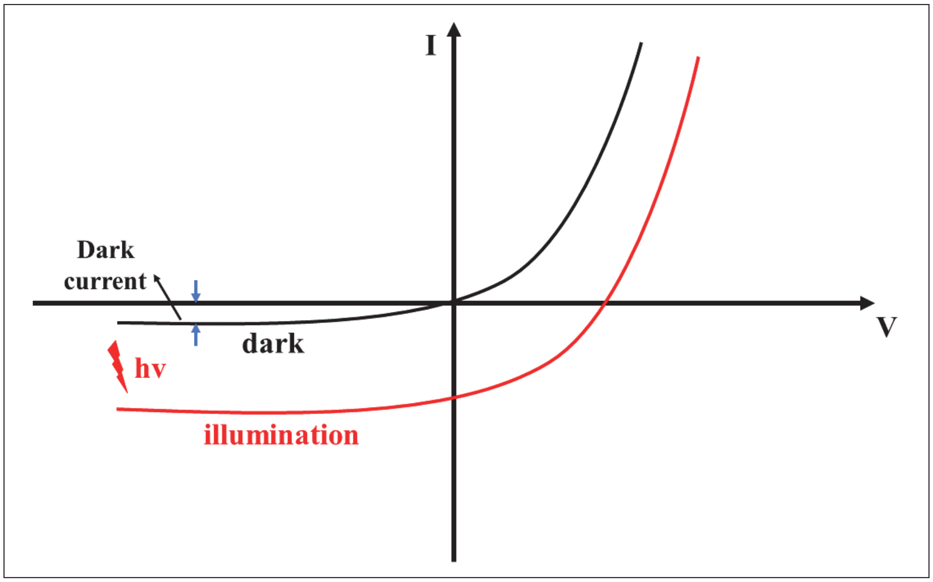

Figure 1.12 IV characteristics of a photodetector in dark and under illumination

sandwiched between two highly doped layers, where ohmic contacts are created. The width of the depletion region can be influenced by the applied voltage and the doping concentration. For highly doped layers, they have a larger energy band than the intrinsic layer so that the *i*-layer absorbs all the incident light [Kimukin]. Therefore, none of the photogenerated carriers diffuse in the highly doped layers, and junction capacitance and transit time are the only limiting factors for the photodetector operating speed [Kimukin]. The degree of band discontinuities is important for such a heterojunction. If the band discontinuity is high, charges trapped at the interfaces would degrade the performance of the photodetectors [Kimukin].

The current in a $p-i-n$ photodetector IV characteristics is the sum of generation-recombination and diffusion currents within the intrinsic region. The current density can be calculated using the equation below [Kimukin]:

$$J = \left(\frac{qD_p n_i^2}{L_p N_D} + \frac{qD_n n_i^2}{L_n N_A}\right)\left[\exp\left(\frac{qV_A}{kT}\right) - 1\right] + \frac{qWn_i}{2\tau}\left[\exp\left(\frac{qV_A}{2kT}\right) - 1\right] \tag{1.5}$$

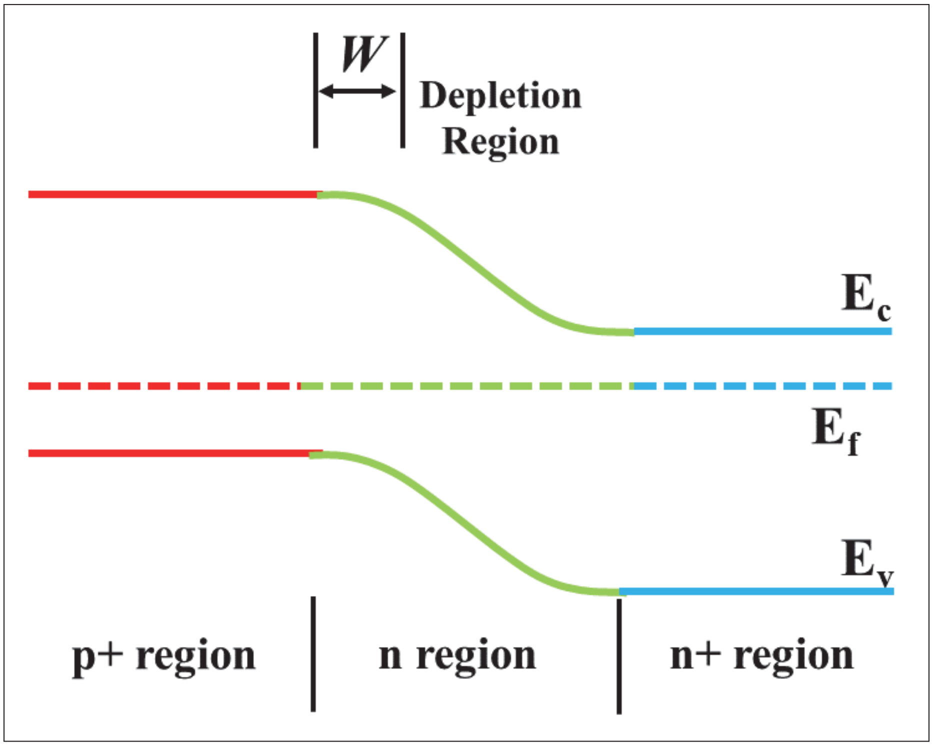

Figure 1.13 Energy band diagram of a $p-i-n$ photodetector.

Where q is the electron charge, τ is the carrier lifetime, W is the depletion region width, n_i is the concentration of the intrinsic carrier, N_d and N_a are the doping concentration, L_n and L_p are the diffusion lengths and D_n and D_p are the diffusion coefficient of the minority carriers in the $n+$ and $p+$ regions respectively. In general, the diffusion current can be ignored since the values of N_a and N_d are very high [Kimukin]. The forward current shows an exponential dependence with respect to the biasing voltage. The dark current (no illumination, Figure 1.12) can be calculated by [Kimukin]:

$$J_{G-R} = \frac{qWn_i}{2\tau} \tag{1.6}$$

Where q is the electron charge, W is the depletion region width, n_i is the intrinsic carrier concentration and τ is the carrier lifetime.

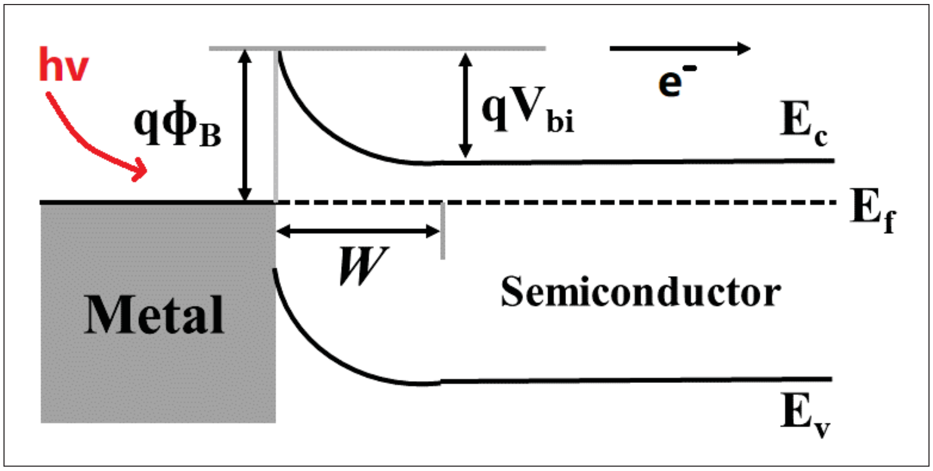

Figure 1.14 Energy band diagram of a Schottky photodetector adapted from [Kimukin].

In contrast, a Schottky-junction photodetector includes a metal-semiconductor junction and a depletion region. Figure 1.14 shows the energy band diagram of such Schottky photodetector under equilibrium. When a metal and a semiconductor material are brought together, electrons at the semiconductor conduction band flow into the metal because of this higher energy. The free electron concentration near the metal-semiconductor boundary is reduced as the electron flows. This electron flow keep happening until their Fermi levels are aligned. The width of this depletion region can be calculated as follows [Sharma]:

$$W = \sqrt{\frac{2\varepsilon}{qN_d}(V_{bi} - V)} \tag{1.7}$$

Where ε is the semiconductor dielectric constant, q is the electron charge, N_d is the density of the ionized donor, V_{bi} is the built-in potential and V is the bias voltage. As the electrons move from semiconductor to metal, ionized donor atoms induced positive charges are left behind. As a result, mobile electrons get depleted near the contact region of the semiconductor. These charge create a negative field. The built-in potential (V_{bi}) caused by this created electrical field can be represented by the difference between the work function of semiconductor (Φ_s) and metal (Φ_m) [Sze & Lee], such as:

$$E_{bi} = -qV_{bi} = \phi_s - \phi_m \tag{1.8}$$

Compared to a $p - n$ junction, the majority of carriers are the main components for the current transport at the metal-semiconductor interfaces. There are four mechanisms where the carrier transport can occur: (1) thermionic emission across the barrier, (2) tunneling through the barrier, (3) carrier generation or recombination in the depletion region, and (4) carrier recombination in the semiconductor neutral region [Kimukin]. Generally for Si- and $GaAs$- based devices, process (1) dominates the carrier transport in the Schottky barrier junctions; therefore, ideal diode characteristics are observed. The thermionic emission theory is developed by Bethe for semiconductors with high mobility [Bethe]. For low-mobility semiconductors, Schottky derived its diffusion theory [Schottky]. Equations below represented the ideal J-V characteristics [Kimukin]:

$$J = J_s \left[\exp\left(\frac{qV_A}{nkT}\right) - 1\right] \tag{1.9}$$

$$J_s = A^{**}T^2 \exp\left(-\frac{q\phi_B}{kT}\right) \tag{1.10}$$

Where q is the electron charge, V_A is applied voltage, T is the temperature, ϕ_B is the Schottky barrier height and A^{**} is the Richardson constant.

1.5 Electrospraying

Electrohydrodynamic (EHD) phenomena have attracted tremendous attentions both in academia and industry over the past decades [Jaworek & Sobczyk]. The main applications of the EHD are electrospraying and electrospinning [Jaworek *et al.*]. The main difference between them is the their products, particles or fibers [Jaworek *et al.*]. The first study of the observation of electrically charged fluids can be traced back to the 1600s [Tucker, Stanger, Staiger, Razzaq & Hofman]. The first journal publication about the electrospinning setup was in 1914 by John Zeleny [Zeleny]. In 1960, Geoffrey Taylor developed a mathematical model of the cone in which the charged droplets are formed at the tip of a nozzle [Taylor]. The 'Taylor Cone' is named after him to describe this cone phenomenon during the EHD process.

Electrospraying would be the focus in this thesis instead of electrospinning. Electrospraying is a technique of the continuous production of mono-disperse droplets that is achieved by the introduction of the potential difference between a nozzle and a metal substrate [Jaworek & Sobczyk]. Electrospraying has the advantages of the flexibility for the droplets size and distribution [Panahi *et al.*]; therefore, it can be used in various fields including polymer particle production [Hogan *et al.*][Wu & Clark], micro-encapsulation [Loscertales *et al.*], nano-particle preparation [Lenggoro,I. Wuled, Fernández de la Mora & Tohge][Rahmani *et al.*] and thin-film deposition [Jaworek & Sobczyk].

1.5.1 Electrospraying Modes

Because electrospraying is implemented as a fabrication technique for optoelectronic device fabrication in this work, a stable jet is critical to achieve a good device performance, aw well as a stable device throughput. Therefore, it is important to study and control the different modes which would appear during the electrospraying process. Various EHD modes are characterized based on types of the fluids and intensities of the applied electrical fields. In general, there are two types of fluids: Newtonian fluids including DI water, and viscoelastic fluids [Panahi *et al.*].

Figure 1.15 represents different modes for Newtonian fluids during the electrospraying process. At the beginning, the dripping mode is observed when there is no electrical field presented. As the applied electrical potential start to increase, the frequency of the droplets increases; and the droplets size decreases according to the Strouhal number [noa (r)]. However, the frequency of the droplet is relatively low, and the size of the droplet is relatively large under low electrical potential. When the electrical potential increases further, the droplet size becomes smaller than the diameter of the nozzle for which micro-dripping mode enters [Panahi *et al.*]. This mode could be used for the production of mono-dispersed aerosol [Panahi *et al.*]. During the dripping and micro-dripping mode, satellite drops are observed occasionally. Spindle mode is the next for which thin filaments of fluid are detached from the nozzle [Panahi *et al.*]. When the electrical potential reaches a certain high value, a stable jet is generated and it is named the cone-jet mode [Panahi *et al.*]. This cone-jet mode can be easily distinguished by the formation of a conspicuous conical at the end of the nozzle [Panahi *et al.*]. At last, a multi-jet mode starts to appear when further increases the electrical potential after reaching the cone-jet mode [Panahi *et al.*]. Multiple tiny jets at the annular rim of the cone are observed in the multi-jet mode.

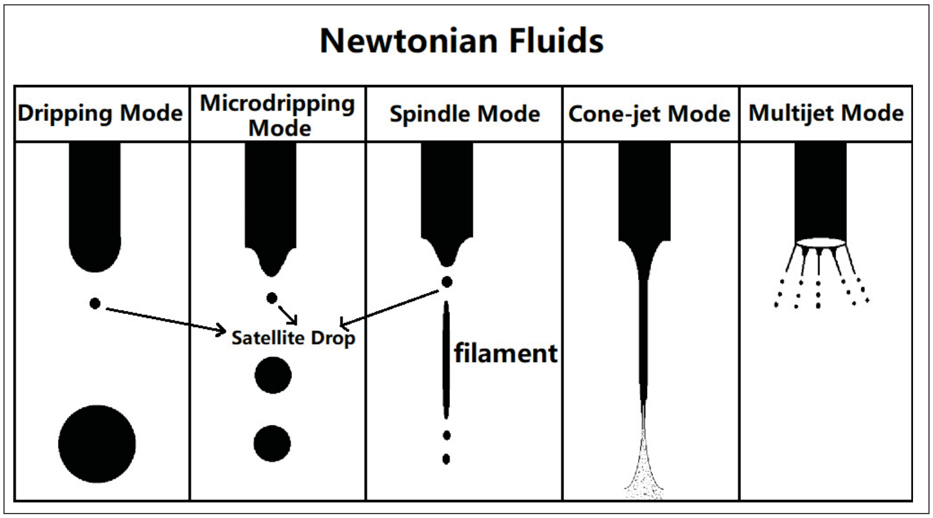

Figure 1.15 Different EHD modes for Newtonian fluids in schematic representation, adapted from [Panahi *et al.*].

The EHD modes for the viscoelastic fluids are schematically represented in Figure 1.16 [Panahi *et al.*]. The first is the dripping mode. For viscoelastic fluids, connection between the droplets and nozzle is considerable stronger than the Newtonian fluids leading to a different breakup process [Panahi *et al.*]. As the applied electrical potential increases, the ejecting droplets tend to adjoin onto a filament (Figure 1.15) due to the elastic properties of the materials themselves. The beads are formed along the string. A cone-shaped jet is obtained when the electrical potential reaches a certain point where the beads are gradually vanished [Panahi *et al.*]. As the electrical potential continuously increase, the jet becomes thinner and it is called the stick jet mode [Panahi *et al.*]. Last, an unstable jet where the cone moves irregularly if the electrical potential is too high [Panahi *et al.*]. The electrosprayed materials are very hard to collect under this mode.

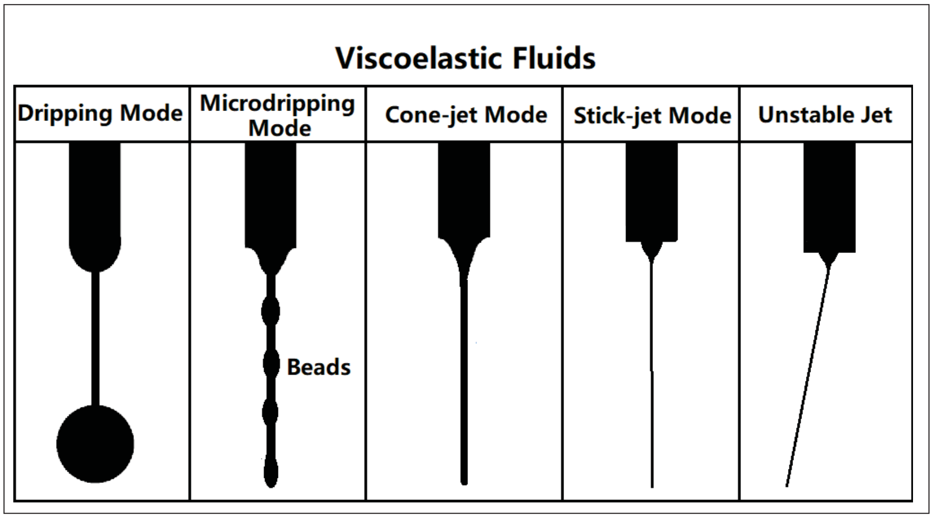

Figure 1.16 Different EHD modes for viscoelastic fluids in schematic representation, adapted from [Panahi *et al.*].

1.5.2 Electrospraying Parameters

There are many parameters can influence the presence the cone-jet mode during the electrospraying process, including applied voltage, flow rate, solution concentration, nozzle gauge, distance between the collector and nozzle, and surrounding conditions [Sındıraç & Akkurt] [Guo].

The applied voltage is a critical parameter in the electrospraying process. The voltage required to generate an electrospray depends on the physical setup of the instruments and the properties of the material/solution being electrosprayed [Kremer]. Equation 1.11 describes the relation between the electric field and the other relevant parameters in electrospraying process [Kebarle & Verkerk]:

$$E_C = 2V_C/[r_C \ln(4d/r_C)] \tag{1.11}$$

Where E_c is the electric field, V_c is the applied voltage, d is the distance between the nozzle and the collector, and r_c is the outer radius of the nozzle. In general, E_c is on the order of $10^6\ V/m$ [Kebarle & Verkerk]. Even though this model is intended for mass spectrometry, not a bulk deposition, it could still be used as a prediction for electrospraying preparation.

The distance refers to the distance from the nozzle to the collector of the electrospraying equipment setup. The distance and the applied voltage are interrelated. Under a constant voltage, a shorter distance would create a stronger electrical field which is advantageous for smaller particle productions; however, it could also cause electric discharge and insufficient time for solvent evaporation resulting in aggregation of wet particles on the collector [Nguyen, Clasen & Van den Mooter (a)]. On the contrary, a longer distance would require a higher voltage to maintain a proper electrical field strength. Additionally, long-distance may cause material loss to the surrounding area especially if there is any air turbulence during the process.

The flow rate describes the velocity of the solution flowing through the nozzle. The unit of the flow rate in this thesis is ml/h and is controlled by a syringe pump. Flow rate also closely tied with the solution viscosity. Under the same solution viscosity, if the flow rate is too high, the spraying behavior would be either stayed within the dripping / micro-dripping mode or enter strong jet mode [Panahi *et al.*]. If the flow rate is too low, the cone shape formed at the nozzle could collapse preventing Taylor Cone from forming [Panahi *et al.*] and multijet mode may occue. In general, high flow rate is required to electrospray the solution with high viscosity.

The electrosprayed material concentration affects the formation of the final products, such as particles or fibers [Yao, Kuang Lim, Xie, Hua & Wang]. When the solution concentration is relatively low, particles are collected at the substrate. As the concentration increases, beads on fibers / clean fibers are produced [Yao *et al.*]. The previous research in our research group indicates the sufficient concentration of the polymer solution is $12 mg/ml$ [Ma] which is not high enough for the fiber formation; therefore, the fibers are not considered in this work. Flow rate and the solution concentration are closely related. In general, higher concentration requires a higher flow rate while lower concentration requires a lower flow rate under the same condition.

The nozzle gauge describes the inner diameter of the nozzle. The inner diameter is inverse proportion to its gauge number; therefore, a larger gauge number has a smaller inner diameter. It is also an important parameter for electrospraying because the inner nozzle diameter determines the size of the base of the Taylor cone [Yarin, Koombhongse & Reneker]. As a result, it can influence the size and the distribution of the deposited particles. [Ghayempour & Mortazavi][Jafari-Nodoushan, Barzin & Mobedi]. Generally, larger inner diameter of the nozzle requires higher flow rate to achieve cone-jet mode.

Temperature and humidity are two parameters that can be relatively important in certain electrospraying processes because they can significantly affect the solvent evaporation rate, as a result, the formation of the final electrospraying products [Fashandi & Karimi][Pelipenko, Kristl, Janković, Baumgartner & Kocbek][Yao *et al.*]. Temperature includes ambient temperature, the surface temperature of the droplet, and substrate temperature [Yao *et al.*][Wilhelm, Mädler & Pratsinis (2003)]. High temperature and low humidity have a positive influence on solvent evaporation; whereas low temperature and high humidity have a negative influence. Okuyama Peclet number can be used as an indicator for particle morphology. The rate of the droplet radius change due to evaporation can be written as a function of the droplet surface temperature. The Okuyama Pe can be written as:

$$Pe = \frac{\frac{\lambda}{c_{\text{vap}}\rho_{LIQ}} \ln\left[1 + \frac{c_{\text{vap}}(T_\infty - T_0)}{L}\right]}{D_{\text{polymer,solvent}}} \tag{1.12}$$

Where T_∞ is the ambient temperature and T_0 is the surface temperature of the droplet. Pe value should be small if smooth spherical particles are desired. To achieve smaller Pe, the diffusion rate of the polymer solution should be increased, or the evaporation rate be reduced [Yao *et al.*]. In the meantime, the difference between the surface temperature T_0 and the ambient temperature T_∞ needs to be minimized. At last, polymer with a high diffusion coefficient in solvent $D_{\text{polymer solvent}}$ would also reduce the Pe value. $D_{\text{polymer,solvent}}$ is the diffusion coefficient of the polymer solvent. It can be calculated using Scheilbel (1954) and Wilke and Chang (1995) equations:

$$D_{\text{solute,solvent}} = \left(8.2 \times 10^{-8}\right) \frac{T}{\mu_B} \left[\frac{1}{V_A^{1/3}} + \frac{(3V_B)^{2/3}}{V_A} \right] \tag{1.13}$$

Where T is the absolute temperature in Kelvin, μ_B is the viscosity of the solvent in centipoise. V_A and V_B are the molal volumes of solute and solvent at normal boiling points.

Because the main focus of the electrospraying technique in this thesis is to implement it into device fabrication; therefore, we are not focusing on the numerical calculation or simulation of the degree of impact for each parameter. As a result, we performed a series of experimental designs to optimize the electrospraying parameters for desired electrosprayed film fabrication. Details about these experimental designs and fabrication results are explained in Chapter 4.2.3.

1.6 Digital Inkjet Printing

Printable electronics refer to electronic devices which could be fabricated via a set of printing techniques on various substrates [Suganuma]. They offer many advantages compared to the traditional micro-electronics fabrication process, including low manufacturing cost, high versatility, possibility towards flexible components, and large-scale production [Tseng]. Flexography, gravure, and screen printing are the main conventional printing technologies [Kwon *et al.*]. These printing techniques generally involve laborious and tiresome patterning or masking processes before the fast and high-scale productions. For example, gravure or flexography are only economically viable on very large batches because of their very expensive startup cost [Sampaio *et al.*][Zavanelli, Kim & Yeo].

Inkjet printing is a rapid growing technology for functional material depositions on various substrate in micro-engineering [Cui & Boland][noa (v)], electronics [Raut & Al-Shamery][Aleeva & Pignataro] and pharmaceutical industries [Daly, Harrington, Martin & Hutchings]. Inkjet printing is a non-invasive (no contact with the substrate) and mask-free technology for functional materials deposition on various substrates including plastic, paper, and metal [Cummins & Desmulliez]. It takes a pattern or image data from the computer and applies it onto the substrate using ink in the form of micro-droplets [Maleki & Bertola]. In non-contact printing, the substrate is only in contact with the printing materials and no mechanical pressure applied to the substrates. It removes the risks of contamination and damage to the pre-patterned substrates. In addition to non-contact printing, inkjet printing also has the advantages of accurate positioning / precision control of the *pico*-liter sized droplets deposition and can be operated under ambient environment [Martin & Hutchings]. FUrthermore, inkjet is cost-effective because it can easily fabricate complex patterns without any physical masks [Yin, Huang, Bu, Wang & Xiong (b)]. Although the reproducibility and performance of the inkjet printed devices and the functional materials availability in the market are still under rated compared to conventional deposition techniques, the versatility of inkjet printing still provides a great implementation to the current production lines [Magdassi]. Table 1.2 summarizes different deposition techniques comparing to the inkjet printing [Maleki & Bertola].

Table 1.2 Comparison of inkjet printing and some typical deposition technologies, adapted from [Maleki & Bertola]

	Spin/dip-coating	Lithography	Vapour Deposition	**inkjet Printing**
Material Waste	High	High	Low	**Low**
Working Area	Medium	Small	Small	**Large**
Pattern Capability	Low	Medium	Low	**High**
Temperature	Low	High	High	**Low**
Mask Required	Yes	Yes	Yes	**No**
Process	Simple	Multi-step	Multi-step	**Simple**
Cost	Low	High	High	**Low**

During the inkjet printing process, ink is delivered to the nozzle heads from the ink reservoir and then micro-droplets are ejected [Singh, Haverinen, Dhagat & Jabbour]. The ejected ink droplets hit the substrate at a specific frequency to perform the printing [Singh *et al.*]. Figure 1.17 shows a schematic of the inkjet printing process [Charles]. The loaded ink is at ambient pressure. A user-controlled digital driving signal is applied to the piezo transducer which controls the jetting of the ink drops [Charles]. Together with the 3D positioning of the nozzles with respect to the substrate, a pattern consisting of a series of ink dots is transferred onto the substrate.

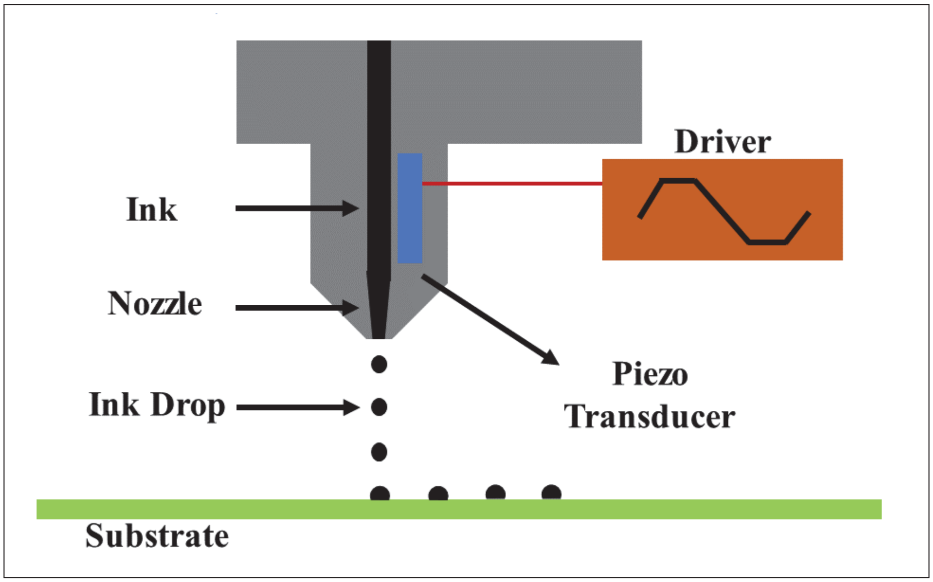

Figure 1.17 A schematic of the inkjet printing process, adapted from [Charles

Generally, the printing heads are fixed while the substrate moves in 3-D directions to avoid any air turbulence which may caused by the moving printing heads.

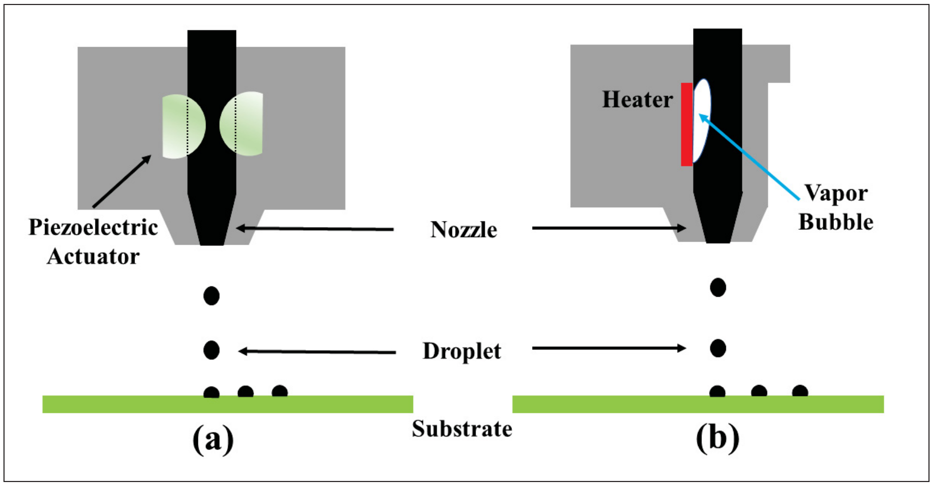

Figure 1.18 A schematic of the piezoelectric inkjet (a) and thermal inkjet (b), adapted from [Maleki & Bertola].

Continuous and drop-on-demand (DOD) are the two main operational modes for inkjet printers. During continuous inkjet printing, a liquid jet is released from the nozzle [Hon, Li & Hutchings].

Because of the its high-speed operation, continuous inkjet printing is normally used in textile labeling and printing [de Gans, Duineveld & Schubert]. DOD mode typically uses two types of actuators: piezo-electric or thermal actuators [Sirringhaus & Shimoda]. In piezo-electric printing, the deformation of the piezo-electric actuator induced by an electric field generates and releases the ink droplets [Jiang & Tan]. A pressure wave is generated by applying a certain electrical potential to the transducer. The generated pressure wave moves to the nozzle and extrudes the ink droplets out, as shown in Figure 1.18a. For a thermal DOD inkjet printer, Figure 1.18b, the ink is heated with a Joule heating unit placed near the nozzle [de Gans *et al.*]. The ink droplets and jetting are generated by the evaporation of tiny amount of ink [de Gans *et al.*]. Therefore, thermal inkjet printers should use volatile solutions, such as water and short-chain alcohols [Maleki & Bertola]. Furthermore, piezo-electric DOD printing has the advantage of a wide variety of ink solvents compared to the thermal DOD printing. Furthermore, the size and flow rate of the jetted droplets can be precisely controlled by regulating applied voltage rather than temperature alternations [Raut & Al-Shamery]. Figure 1.19 shows the ink droplets formation of a DOD inkjet printer. Ink trails (Figure 1.19a) or satellite drops (Figure 1.19b) should be avoided at the printing distance [Charles].

The ink characteristics in the inkjet printing technology should be carefully formulated to obtain specific properties, including density, viscosity, surface tension, and size distribution [Martin, Hoath & Hutchings]. However, all the inks used in this thesis are purchased from commercial suppliers; the characterizations of the inks themselves are not our primary focus in this thesis. The printing conditions are very important to yield stable droplets (Figure 1.19c), besides the ink characterizations. Ink solutions should be prepared with a particular printing condition to obtain ideal interfacial & rheological properties [Maleki & Bertola]. Nanoparticles dispersed in the solutions tend to agglomerate causing particle sedimentation; additionally, nozzle clogging may be induced by the particle agglomerations due to rapid solvent evaporation [Maleki & Bertola]. Consequently, the employments of average particle size less than 1/50th of the nozzle diameter and the addition of dispersing agents are preferred [Sundriyal & Bhattacharya]. The ink surface tension and viscosity have great influences on the dynamic of the droplets, and must be controlled

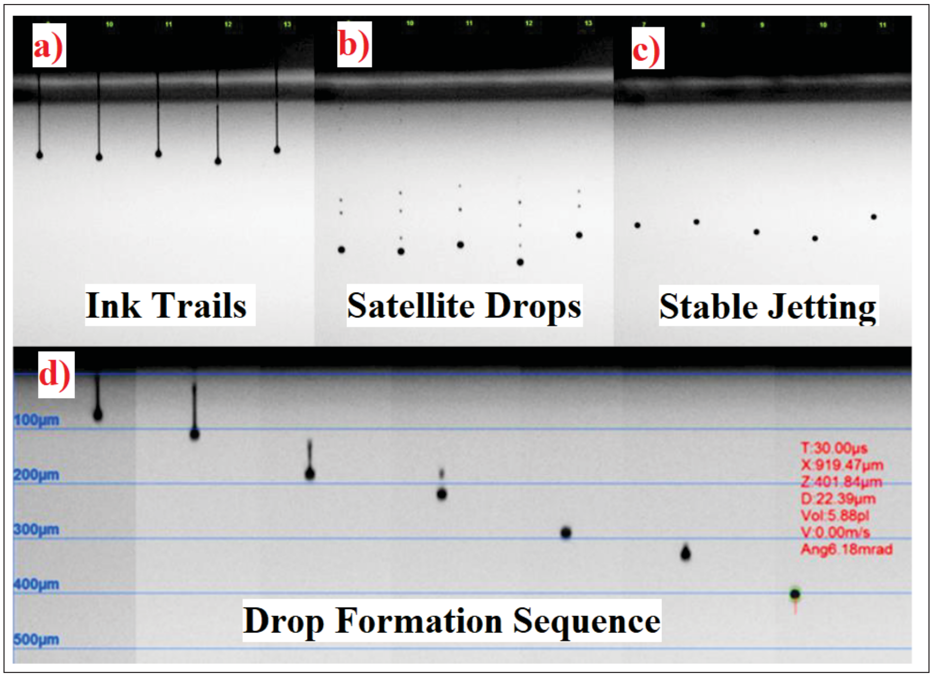

Figure 1.19 Drop formation and jetting ink images of a inkjet printer, adapted from [Charles]. (a) ink trails, (b) satellite drops, (c) stable ink jetting, (d) drop formation sequence from trails to satellite and stable jetting.

and optimized carefully [Maleki & Bertola]. For low viscous inks, unstable droplets may form during the printing resulting in the formation of satellite micro-drops (Figure 1.19b); meanwhile, very high viscous ink solution can not eject smoothly from the nozzle [Cummins & Desmulliez]. Low surface tension could cause air ingestion and droplets dripping, high surface tension obstructs the drop formation [Waasdorp, Heuvel, Versluis, Hajee & Ghatkesar]. Even though viscosity and surface tension are the primary physical properties that resolve the drop size and formation; printing conditions and nozzle size are also important for the jettability of the materials [Mahbubul, Saidur & Amalina]. These parameters are merged into the Weber number (We), Reynolds number (Re), and Ohnesorge number (Oh) as shown below [Mueller, Llewellin & Mader]:

$$We = \frac{\rho V^2 L}{\sigma} \tag{1.14}$$

The Reynolds number (Re) describes the ratio of the inertial force to the viscous force:

$$Re = \frac{\rho V L}{\eta} \tag{1.15}$$

The Ohnesorge number (Oh) is the ratio between the viscous force and the surface tension & inertial forces as:

$$Oh = \frac{\sqrt{We}}{Re} = \frac{\eta}{\sqrt{\rho L \sigma}} \tag{1.16}$$

Here, ρ is the density in kg/m^3, η is the material viscosity in cP, σ is the surface tension in mJ/m^2, V is the droplet velocity in m/s and L is the nozzle diameter in m. The ink suitability for drop formation is predicted by the Z number ($1/oh$) [Fromm]. The ink droplets are printable for a DOD inkjet printer when $1 < Z < 10$ [Derby]. Figure 1.20 shows the defined printable region and drop formation in the Re $vs.$ Oh chart. In the low viscous region ($Z > 10$), satellite droplets will be generated; and the fluid can not turn into droplets when ($Z < 1$). Whereas, the parameter Z only provides an approximation for the ink printability. It is reported that the onset of splashing occurs (dash line in Figure 1.20) when droplet jetting is above a critical point, which is $We^{1/2}Re^{1/4} > 50$ [Stow, Hadfield & Ziman].

After achieving stable a jetting, the interactions between the substrate and printed liquid must be understood to achieve controlled printing by manipulating parameters [Derby]. These are generally referred to as the interaction between the ink and the substrate, and the effects of the ink fluid dynamics [Derby]. The coffee ring effect is named after the characteristic ring-like deposition of a spill of coffee [Larson]. This effect describes the non-homogeneous solvent evaporation where an outward convective flow forces particulates to the edge. [Larson]. The left inset of Figure 1.21 represents a camera image of a coffee ring which includes a densely deposited area (the black outer ring, A) and a sparse area (grey area, B). This coffee ring effect can be reduced by introducing Marangoni flows to counter the outward convective flows

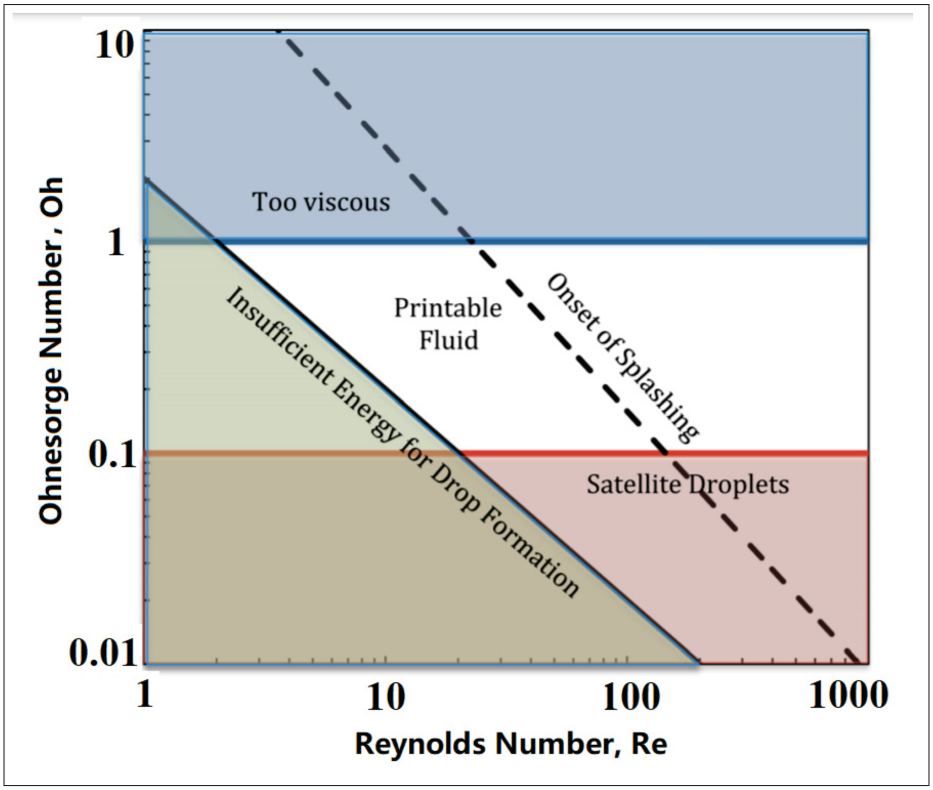

Figure 1.20 Schematic diagram of the inkjet stable operation regime, adapted from [McKinley & Renardy]

[Majumder *et al.*]. The Marangoni flows can be employed via drying atmosphere modification and solvent engineering [Kim, Dhage, Shim & Hahn (a)]. Figure 1.21 shows the difference of the particle distributions between normal dried and Marangoni dried solution drops. In a normal dried situation, particles agglomerate at the edge due to outward convective flow after solvent evaporation [Majumder *et al.*]. On the contrary, the induced Marangoni forces create recirculating flows which homogenize the particle concentration leading to uniform deposition [Majumder *et al.*]. The coffee-ring effect ties to the evaporation of the ink solvent; therefore, it can also be affected by other parameters including the temperature of the printing substrate [Kim *et al.* (a)], the temperature of the printing ink [Soltman & Subramanian] and the solvent boiling point [Sette]. Therefore, post-printing and ink-drying processes are extremely important in controlling the morphology of the deposited materials [Charles].

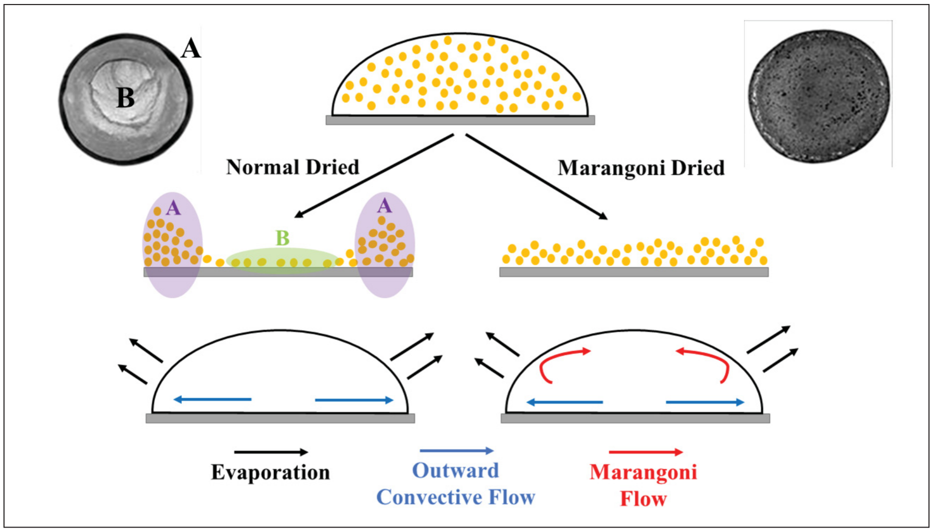

Figure 1.21 A Schematic of the different droplet drying mechanism, non-assisted on the left and Marangoni flow assisted on the right, adapted from [Al-Milaji & Zhao]

Functional devices require continuous tracks or areas to be printed by overlapping individual droplets and the resultant features should be stable and functional [Alamán *et al.*]. The drops of ink coalesce into a single liquid bead when they are deposited along a line [Alamán *et al.*]. This bead is stable if the contact angle is $< 90^o$ [Schiaffino & Sonin]. Figure 1.22 shows printed droplets along a line as the spacing between adjacent drops decreases. When the spacing is large, individual droplets are printed because they do not interact when spreading (Figure 1.22a). As the spacing decreases, the drops tend to coalesce while keeping most of the liquid at their original positions resulting in a scalloped line (Figure 1.22b). When an ideal spacing is reached, a uniform line with clean edges is achieved (Figure 1.22c). Line widening and eventually repeating bulges are formed if the spacing decreases further (Figure 1.22d).

Finally, pre-and/or post-printing processes are necessary to finalize a stable device in addition to the stable jet and drop interactions analysis. The pre-printing process is generally used to modify the surface energy of the substrates. Some of the techniques are UV exposure [Efimenko, Wallace & Genzer], chemical treatments [Bodas & Khan-Malek] and plasma treatments [Ashraf, Mattsson, Fondell, Lindblad & Thungström]. The post-printing processes includes annealing,

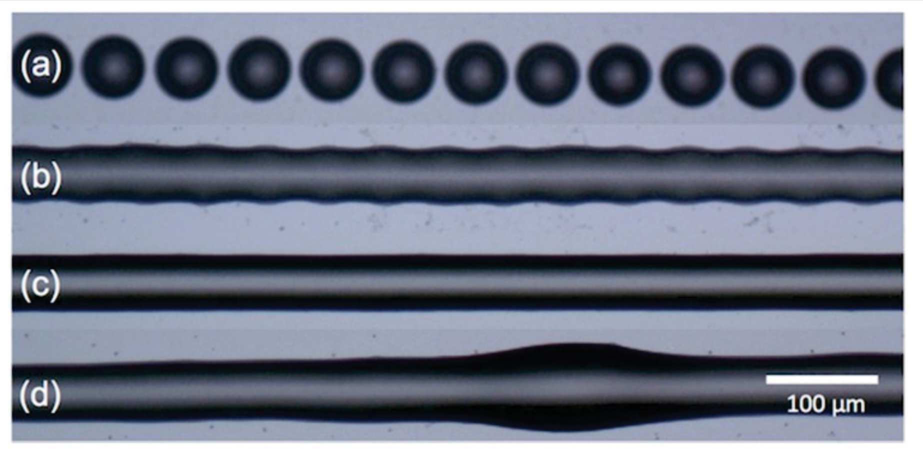

Figure 1.22 Droplets deposition for a line formation with decreased spacing between adjacent drops from a to d. (a) isolated drops, (b) scalloped line, (c) uniform line, and (d) line bulging. [Alamán *et al.*]

sintering and ablation [Mattana *et al.*]. Annealing and sintering are basically the same and it often refers to long conventional heating processes and fast optical processes respectively [Charles]. The ablation treatments often involve using lasers to ablate the printed materials to achieve finer feature sizes [Charles].

1.7 Structure of the Thesis

This dissertation focuses on optoelectronic device fabrication and characterization including LEDs and Photodetectors by using organic/inorganic hybrid materials via different fabrication techniques, including spin-coating, electrospraying and ink-jet printing.

This thesis is divided into 6 chapters. Chapter 1 is the induction chapter including literature reviews on materials, devices, and fabrication techniques. Chapter 2 describes the materials, fabrication techniques, and characterization methods used in this work. In Chapter 3, triple-cation perovskite NIR LEDs are fabricated and characterized. However, the emission wavelength is fixed unless changing the perovskite cooking recipe. Chapter 4 represents the micro-particle PLEDs fabricated using electrospraying. The emission wavelength can be easily tuned by controlling the mixture ratio of the electrosprayed materials. The stability of the device fabrications using electrospraying is hard to control; therefore inkjet printing technique is implemented in Chapter 5. Chapter 5 shows fabrications and characterizations of fully inkjet-printed Si-based photodetectors. Finally, the conclusions of this thesis and the future research prospects are shown in Chapter 6. Figure 1.23 shows the structure of this

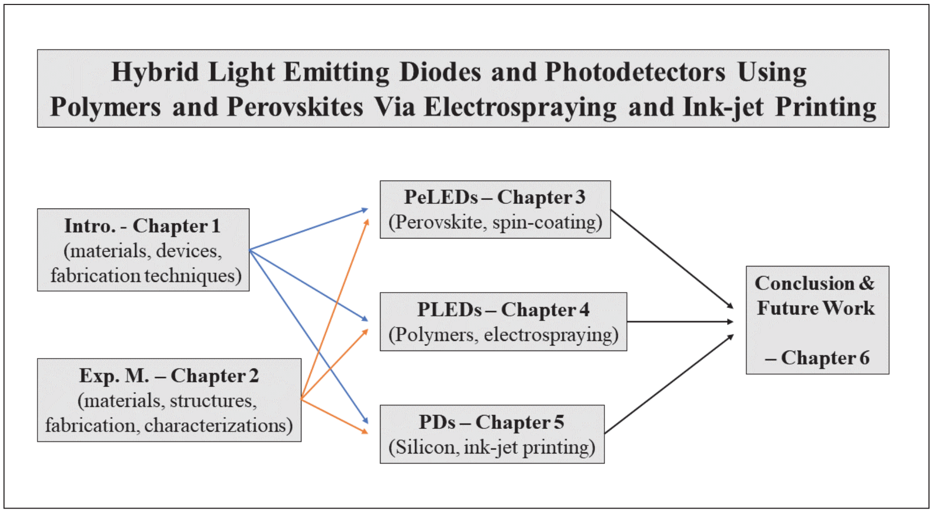

Figure 1.23 Thesis overview and structure

CHAPTER 2

EXPERIMENTAL METHODS

2.1 Materials Used in This Thesis

Two kinds of light-emitting materials are used in device fabrications in this thesis: conjugated fluorescent polymers and perovskites. These conductive fluorescent conjugate-polymers include Poly[(9,9-dioctylfluorenyl-2,7-diyl)-co-(4,4-(N-(4-sec-butylphenyl)diphenylamine)] (TFB), Poly(9,9-dioctylfluorene-alt-benzothiadiazole) ($F8BT$), Poly(9,9-di-n-octylfluorenyl-2,7-diyl) ($F8$) and Poly[2-methoxy-5-(2-ethylhexyloxy)-1,4-phenylenevinylene] ($MEH-PPV$); they are purchased from American Dye Source and Ossila. The perovskite is prepared from chemicals purchased from Sigma Aldrich and Ossila.

2.1.1 Polyfluorene Polymer

Polyfluorene is a class of conjugated polymers that contains fluorine units as represented in Figure 2.1a [noa (o)]. The major part of the conjugated backbone consists of a pair of benzene rings and the octyl side chains contribute to the solubility of the polymers [noa (o)]. TFB, its polymer molecular structure is shown in Figure 2.1b [noa (t)], is a blue light emitting polymer with the highest occupied molecular orbital ($HOMO$) level of $5.3eV$ and lowest unoccupied molecular orbital ($LUMO$) level of $5.3eV$ [noa (t)]. It is used as the hole transport polymer in this thesis because of its well-aligned HOMO level with the ITO anode. For polymer materials in general, their electron mobility is lower than their hole mobility [Guo]. As for the electron transporting polymer, $F8BT$ [noa (f)], $MEH-PPV$ [noa (j)] and $F8$ [noa (n)] are used for different device fabrications. The molecular structure of $F8BT$, $MEH-PPV$ and $F8$ are shown in Figure 2.1(c-e) with the $HOMO/LUMO$ values of 5.9/3.3, 5.3/3.0 and 5.8/3.0 eV respectively.

The solution concentration used in this thesis is measured in weight per volume, mg/ml. A transparent glass vial is used to contain the polymer solution and it is a lot cheaper than a

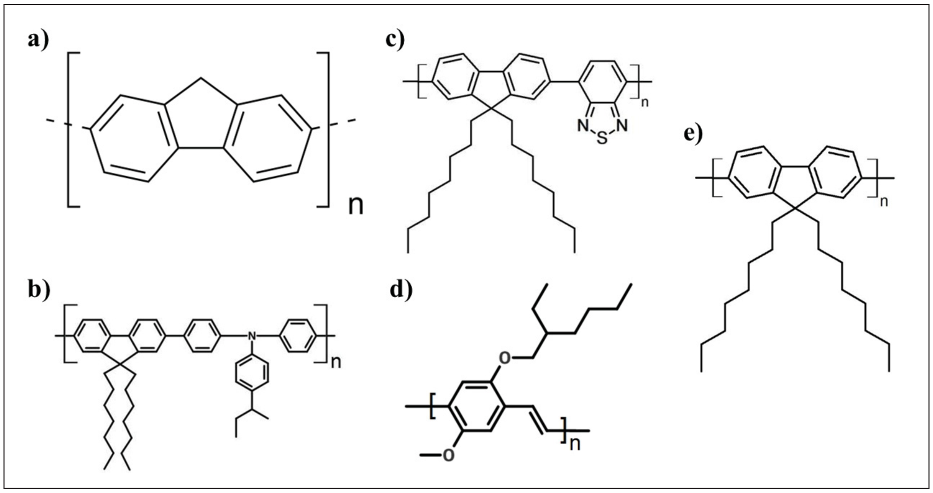

Figure 2.1 Polymer molecular structure. (a) Fluorine unit in polyfluorene. (b) TFB. (c) $F8BT$. (d) $MEH - PPV$. (e) $F8$

amber glass vial. From economic and device efficiency perspectives, the polymer solution is for one-time use and only prepared right before the device fabrication to prevent polymer decomposition due to the ambient UV light. For the solution preparation process, the weight of the vial is first measured on a balance with an accuracy of $0.1mg$ before the balance is re-zeroed. The polymer material is then added into the vial by either a spatula or tweezers while the vial is removed from the balance to prevent the polymer materials from dropping onto the balance affecting the measurement accuracy and contaminating the equipment. Tweezers is more convenient for fiber-like polymers manipulation, such as TFB and $MEH - PPV$. The adding or removing procedures are repeated until reaching the desired value. As the solvents used to dissolve the polymers, THF is used for TFB, $F8BT$, and $MEH - PPV$ while chlorobenzene is used for $F8$. The reason for using THF instead of commonly used solvents, such as chloroform and toluene, is because of its high conductivity and plastic friendliness [noa (s)]; High electrical conductivity offers a an easier control of the electrospraying process. Because the syringes and the tube connecting the syringe and positively connected nozzle are made of plastic, using toluene will destroy these equipment damaging the entire fabrication process. A syringe is used to measure the designed solvent quantity. The solvent is slowly injected into the vial to prevent any splash of either polymer materials or the solvent to maintain the weighting accuracy. After capping, the vial is held in hand and vibrated on a mixer (Maxi-Mix I) to fully dissolve the polymer in the solution. The general batch sizes are about $2 - 5ml$. For a 1-inch square substrate, $0.5ml$ solution is needed for one round of spin-coating. As it is for electrospraying, $2 - 4ml$ is generally required for each deposition and the extra $1ml$ solvent is prepared as a backup. To remove any dust and/or impurity in the solution, all liquid solutions are filtered by a $0.2\mu m$ PTFE filter before device fabrication.

2.1.2 Organic-Inorganic Halide Perovskite

Perovskite is a class of compounds which have the same type of crystal structure, such as ABX_3 (A = organic cation: $CH_3NH_3{}^+$ (MA), $CH(NH_2)_2$ (FA), $C_6H_5(CH_2)_2NH_3{}^+$ (PEA) or inorganic cation: Cs, Rb; $B = Pb$, Sn; $X = I$, Br, Cl) [Le, Jang & Kim (a)]. There have been generated tremendous amount of research and undergone remarkable development due to their excellent properties, including high charge-carrier mobility, high PLQY, solution process and tunable bandgap[Chen, Zhou, Jin, Li & Zhai (a)][Zhang *et al.* (b)][Le *et al.* (b)][Konstantakou & Stergiopoulos][Yin, Yang, Kang, Yan & Wei (a)][Li *et al.* (c)][Zhou, Tang & Yin (a)].

Organic-inorganic halide perovskite can be divided into different groups by their number of cations, such as single-cation, double-cation, and triple-cation. The organic-inorganic halide perovskite material used in this thesis is triple-cation perovskite mainly because of its high stability in the ambient environment [Guo *et al.* (a)]. Details about the triple-cation perovskite compositions and synthesis will be explained in Chapter 3.

2.2 Device Structure

2.2.1 General Device Structure and Design Requirements

Generally, a sandwich structure where thin active layers are sandwiched between two electrodes (Figure 2.2a) is used for these organic and perovskite materials-based devices. The transparent electrode is crucial for the efficiency of these devices because of the in- or out-coupling of light. The most ideal characterization of a such transparent electrode is a combination of low sheet resistance R_s and high transmittance T in the $UV - vis$ to near-IR (NIR) region [Hofmann, Cloutet & Hadziioannou]. Several material classes are used as conductive and transparent electrodes including indium tin oxide (ITO), fluorine tin oxide (FTO), metal nanogrid & nanowires, graphene and carbon nanotubes [Granqvist]. Despite the advantages of these new conductive and transparent materials, ITO and FTO are still the most commonly used in industry for liquid display applications [Choi, Kwak, Park & Sung][Girtan & Negulescu]. The ITO and FTO used in this thesis are purchased from Kintec Company (15 Ω/sq) and Ossila (11 – 13 Ω/sq) respectively. The purchased ITO and FTO generally have a surface roughness around tens of nm. These spikes on the surface could result in a piercing of the active layer [Seeley]. Therefore, a thin layer of $PEDOT : PSS$ is usually deposited first before any organic layer deposition. $PEDOT : PSS$ is a water-based conductive polymer with a work function of 5.0 – 5.1 eV which is slightly higher than the work function of ITO and FTO [Cook, Al-Attar & Monkman]. This work function alignment could greatly facilitate the hole injection from the anode [Cook *et al.*]. The deposition of the $PEDOT : PSS$ layer not only has the advantage of being none-reactive with deposited organic solvents from the top because its water-based characteristic, but also blocks the oxygen ions diffusion from the ITO or FTO layer to the active materials causing degradation [Hwang, Amy & Kahn (a)]. The $PEDOT : PSS$ used in this thesis is PVP Al 4083 which is designed for an LED application ,purchased from Ossila.

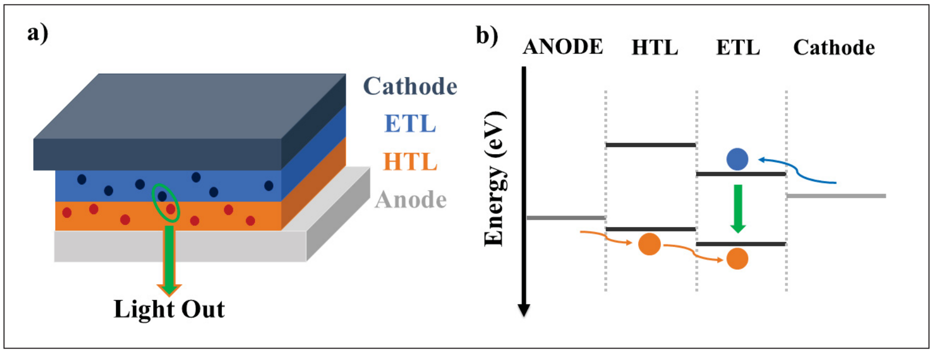

Figure 2.2 The structure of an organic LED. (a) Schematic of a general LED structure. (b) The band alignment of the corresponding LED provided in (a)

The active region atop of the $PEDOT:PSS$ is the place where the holes injected from the anode and electrons injected from the cathode recombine radiatively and emit light. The structural and material design follows the band alignment to achieve smooth electron and hole injection. It also prevents any radiative recombination outside of the active region. The details of the active region design in this thesis will be investigated and discussed according to each specific device.

Finally, a metal cathode is deposited on top of the ETL to inject electrons. A good conduction band alignment between the cathode and ETL is critical to ensure a good electron injection, as well as balanced electron and hole densities within the device [Pan *et al.* (b)][Wu *et al.* (a)]. Figure 2.2b shows a general band alignment for a LED device. As the materials chosen for the cathode, more stable metals including Al, Ag, and Au are generally used instead of better suited low work function metals such as Ca and Mg.

2.2.2 Device Layouts

The substrate of the device is either an ITO or FTO coated glass. A $3mm$ wide area at the top of the substrate is taped with Kapton tape throughout the entire device fabrication. It ensures a good anode contact after its removal for the characterizations by preventing any chemicals from contaminating the substrate. Except for the top cathode electrode, the rest material depositions will cover the entire sample surface. Top cathodes are patterned as multiple 2x2 squares and these overlaps between cathodes and anode define the fabricated devices' areas as is shown in Figure 2.3.

2.3 Fabrication Techniques

2.3.1 Spin Coating

Spin-coating is widely used as a liquid fabrication method for solution-based material deposition [Sahu, Parija & Panigrahi]. Before spin-coating starts, the substrate is placed on a rotational

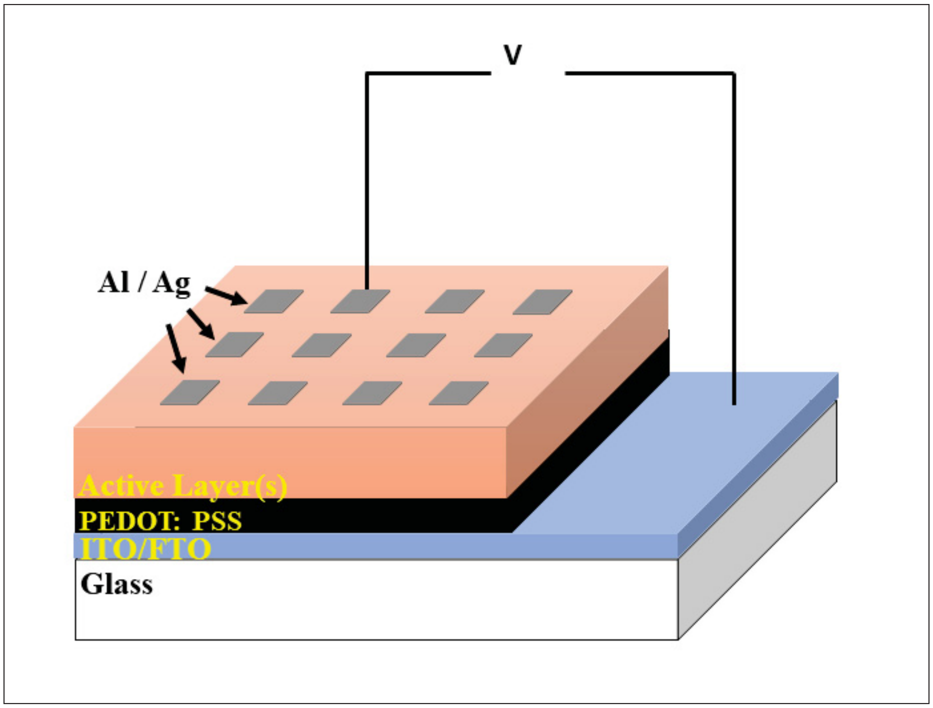

Figure 2.3 A schematic about the general device layout.

stage held by a low vacuum to fix its position during spinning. There are two ways of applying materials in spin-coating, before and during the spinning.

During the spinning process, the solution is pushed to the edges of the substrate under the speed of ~ 500 to 6000 rpm (the speed range varies from different spin-coating machines). In this work, the usual spin-coating time is between 30 s and 120 s for low boiling point solvents, such as chloroform and hexane; and high boiling point solvents, such as water and toluene respectively. The schematic diagram describing spin-coating is shown in Figure 2.4.

To fulfill PLED's potential for high thermal stability, long operation lifetime, and high efficiency, a multi-layer architecture is usually necessary [Guo]. However, the similar solubility of conjugated polymers in common organic solvents generates a great challenge when fabricating multi-layer PLED devices via spin-coating [Guo]. The deposited polymer layers will be dissolved together destroying the multi-layer structure as shown in Figure 2.5. Therefore, we have implemented the electrospraying technique into the PLED fabrication to overcome such difficulties.

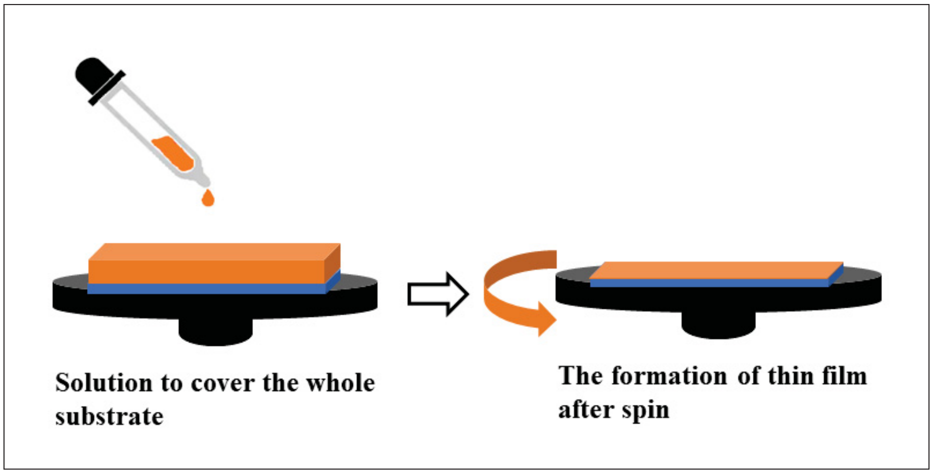

Figure 2.4 Schematic diagram of spin-coating process.

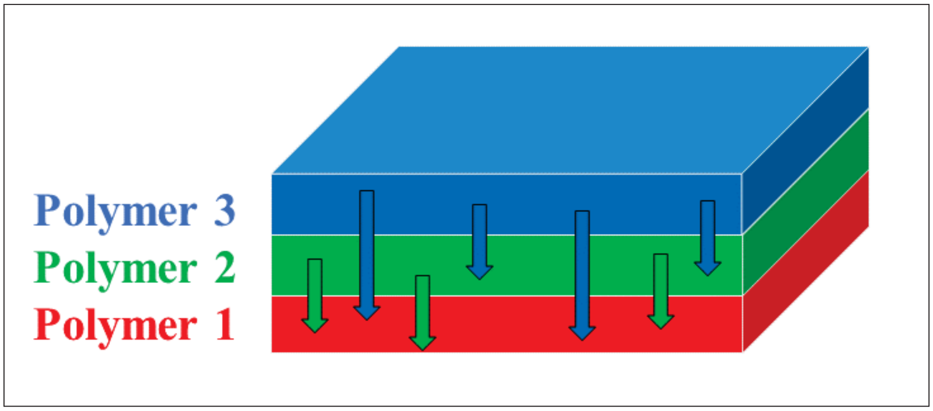

Figure 2.5 Cartoon picture shows what will happen when fabricating multi-layer structure using spin-coating technique.

2.3.2 Electrospraying

Electrospraying is a method of liquid atomization by electrostatic forces to break the surface tension of the solvent under high electrical potential [Jaworek & Sobczyk]. During the electrospraying process, the jet will start after the formation of the "Taylor Cone" at the tip of the nozzle [Jaworek & Sobczyk]. In the process of reaching the grounded metal collector, fast solvent evaporation would result in the collection of particles [Jaworek & Sobczyk].

Figure 2.6a is a cartoon schematic of the electrospraying setup. In this work (Figure 2.6b), the setup includes a syringe pump, an up to 20 kV power supply (Figure 2.6d), and a plastic chamber containing a metal collector. The syringe pump (Figure 2.6c) is used to precisely control the flow rate through the nozzle. The plastic chamber provides protection again high voltage; as well as a controlled environment. In the electrospraying process, the nozzle is connected to the positive end of the power supply and the metal collector is grounded. The distance variation of this setup ranges from 0 – 15 cm. The rotational bell in Figure 2.6b on the bottom is generally used for the fiber deposition which is not necessary for the device fabrication in this thesis.

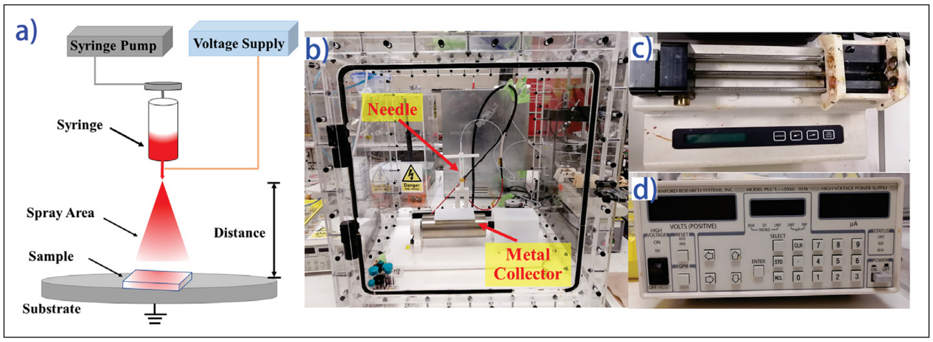

Figure 2.6 (a) A cartoon schematic of the electrospraying setup. (b) our inlab electrospraying setup. (c) syringe pump. (d) power supply up to 20kV.

For the devices fabricated using electrospraying in this thesis, the characteristic of the electrosprayed micro-particle layer can be affected by seven electrospraying parameters. They are flow rate, voltage applied (voltage), distance between nozzle and grounded metal collector (distance), the gauge of the needle (needle gauge), temperature, deposition time (time), and the concentration of the solution (concentration). Detail analysis of these electrospraying parameters are described in Chapter 4.2.3.

2.3.3 Thermal Evaporation of Cathode

Besides printing, metal electrodes can be deposited with both sputtering and thermal evaporation. However, high kinetic energies contained by metal atom spray generated by plasma gas bombardment can cause substantial damage to the polymer materials resulting in low break-up voltage, high device short chances, and unstable device current [Williams]. Much more reliable device performances are obtained via thermal evaporation.

Thermal evaporation is one kind of physical vapor deposition (PVD) which is commonly used for controlled thickness thin film and high quality deposition [Wang, Li, Wu, Wen & Qi (e)]. Figure 2-7a shows the schematic of common thermal evaporator. It contains a pumping system, a vacuum chamber, a substrate holder, crucible containing target material and a crystal monitor. Before the material evaporation, the vacuum chamber will need to go through vacuum procedure twice operated by mechanical (10^{-2} - 10^{-3} torr) and diffusion pump (10^{-6} - 10^{-7} torr) respectively to ensure a good vacuum within the chamber preventing reaction of high temperature material from any air composites. After reaching the desire vacuum level, voltage is applied to the crucible in order to reach the vapor temperature of the target material. The cathode deposition rate can be controlled with altering the applied voltage and the deposition thickness is monitored by the crystal monitor. For the evaporated Al and Ag contacts used for the devices in this thesis, a thickness of 120 - 150 nm is generally used and the deposition rate is controlled around 0.3 Å/s. The thermal evaporator used in our lab is shown in Figure 2-7. The Al (Sigma Aldrich, 99.9999 %) or Ag (Kurt J. Lesker, 99.99 %) is loaded into tungsten filaments.

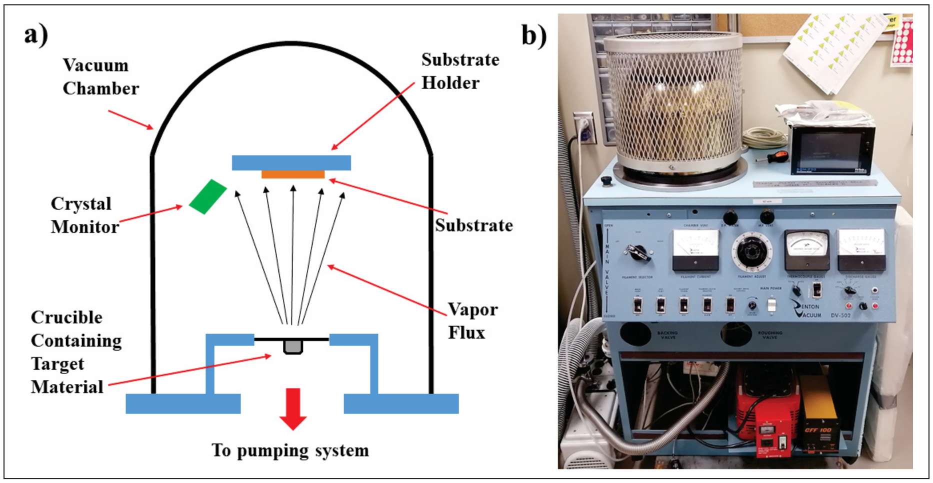

Figure 2.7 Pictures for thermal evaporator. (a) Schematic sketch of a common evaporator, adapted from [Ma]. (b) The evaporator used for metal contacts deposition in this thesis.

2.3.4 Inkjet Printing

The model of the inkjet printer used in this thesis is the CeraPrinter X-Serie as shown in Figure 2.8. It has a high accuracy motion system up to ±1.5 μm on the x and y-axis and ±2 μm on z-axis for stage accuracy. The printheads have a resolution of 5 x 5 µm with the printhead heating up to 60 °C. The substrate holder has a dimension of 305 x 305 mm with a maximum heating temperature of 60 °C. An AdphosNIR post-treatment element is also installed to dry or cure the printed samples.

Figure 2.8 Ceradrop X-serie inkjet printer. [noa (d)]

Firstly, the analysis of the ink drop formation is required to ensure stable printing. The jetting waveform and the temperature of the nozzle are the parameters to control for a stable jetting [Shafiee & Atala]. The waveform is made of intensity and time segments. The intensity refers to the electric-pulse strength sent to the piezo transducer of the printing nozzles [Shafiee & Atala]. The size of the ink-drop volume and its velocity is proportional to the strength of the peak intensity

[Zhang *et al.* (c)]. The time segments refer to the time duration of the positive or negative bias and the transition duration between them. Shorter time segment tends to prematurely cut the ink drops forming smaller drops which could lead to undesired satellite drops [Zhang *et al.* (c)]. Figure 2.9 shows a schematic example of the jetting waveform. The x-axis is the time duration in μs and the y-axis is the bias voltage in V. When the bias voltage is positive, the loaded ink is ejected from the nozzle; when the bias voltage is negative, the ink is filled up. For the temperature of the nozzle, a low temperature is generally beneficial to prevent the nozzle clogging by limiting the solvent evaporation.

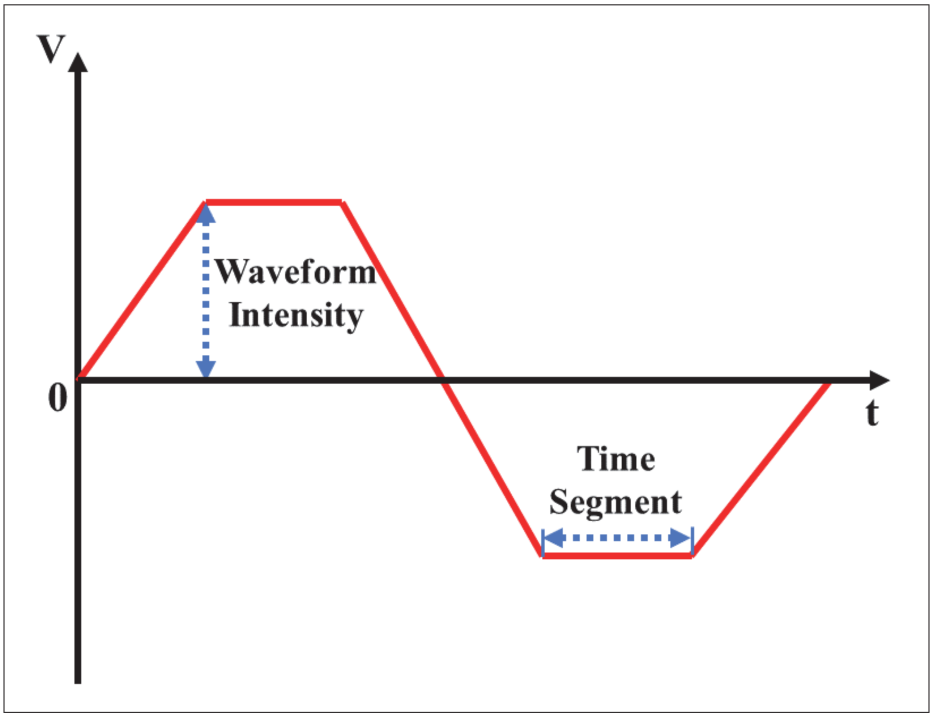

Figure 2.9 A schematic example of the jetting waveform sent to the piezo transducers of the nozzles.

After the formation of the stable jetting as mentioned in Chapter 1.6 by carefully manipulating the waveform, the analysis of the dimension for each drop on the substrate is required. For this analysis, a group of individual drops with a big spacing among them is printed onto the substrate. Typically, at least ten drops are measured and the average value is taken to be the dimension of this ink, which is also called "Splat diameter".

Afterward, a pre-designed file containing the printing pattern is imported to be sliced. For the printing settings for the designed pattern, several parameters are worth mentioning, such as lattice formation, splat diameter, number of layers, printing direction, and post-treatment setup [Sette]. The lattice formation affects the printed droplets' positions concerning the others. A more uniform layer coverage can be achieved by adjusting the lattice formation from the software's built-in settings, including Square, centered square, hexagonal centered, and hexagonal shifted lattice as it is shown in Figure 2.10. The squared lattice is used for the device printing in this thesis. The splat diameter reflects the drop size which has been measured previously. The number of layers is the parameter controlling mainly the thickness in which a larger number of layers generally indicate greater printed thickness. Printing direction is very important, especially in printing lines in either X- or Y-axis direction. The post-treatment setting could control the power and time duration of the NIR exposure, as well as the timing during the printing process. Finally, the actually printing are proceeded with the designed jetting waveform and print distance & frequency settings.

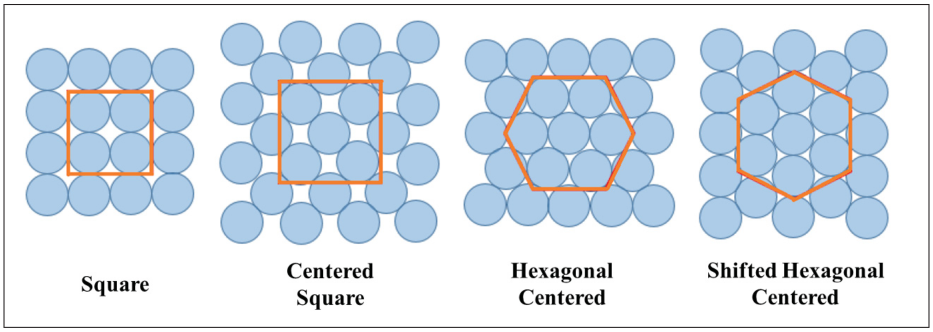

Figure 2.10 A schematic showing different printing lattice [Charles].

2.4 Material and Device Characterization Methods

2.4.1 Ultraviolet-Visible Absorption Spectroscopy

Ultraviolet-visible ($UV - VIS$) absorption or transmission spectrum is the measurement of the attenuation of a light beam after it passes through or reflects from a sample surface [Hameed, Bhatt, Nagaraj & Suresh]. It is a very important tool for material molecular or crystal structure characterizations [Hameed *et al.*]. As for semiconductor materials, enough photon energy is required for electrons to reach their excited state [Sze & Lee]. Electron would jump to higher energy states in the conduction band once photons have provided enough energy to overcome the energy bandgap of the semiconductor materials [Sze & Lee]. Therefore, the energy bandgap of the semiconductor can be determined by the absorption spectrum. Figure 2-11 presents a simple cartoon about the UV-VIS measurement setup.

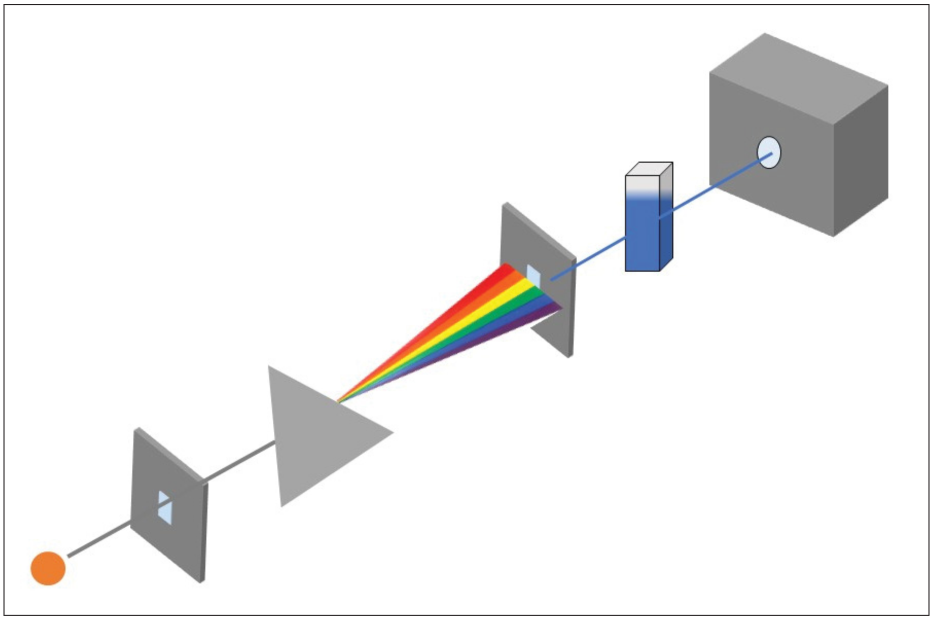

Figure 2.11 Schematic of a UV-VIS measurement setup, adapted [Gohain]

In the process of obtaining the absorption spectrum, light generated from a light source, typically a tungsten or mercury lamp, will pass through a monochromator and illuminates the sample. The transmission spectrum is recorded with a CCD array based on the amount of light transmitted through the sample at each wavelength. In order to obtain an accurate measurement, a baseline calibration is usually performed with a reference sample. Beers Law describes the conversion between the transmission spectrum and absorbance:

$$A = -\log_{10} T = -\log_{10} \frac{I}{I_0}$$

Where A is absorbance, T is transmission, I is transmitted light intensity, I_0 is emitted light intensity.

2.4.2 X-ray Powder Diffraction Analysis

X-ray powder diffraction (XRD) is a common experimental equipment used to determine the atomic and molecular structure of a crystal [Khan *et al.*]. It is based on constructive interference of a crystalline sample and monochromatic X-rays [Khan *et al.*]. When the conditions satisfy Bragg's Law, constructive interference and a diffracted ray are produced by the interaction between the incident rays and the samples [Khan *et al.*]. With a range of 2θ scanning, all possible diffraction directions of the lattice should be attained. Then the different minerals can be identified by the conversion of the diffraction peaks to d-spacing because each mineral has a set of unique d-spacing [noa (w)]. Bragg's Law:

$$n\lambda = 2d\sin(\theta) \tag{2.1}$$

where n is the "order" of the reflection, λ is the incident X-rays wavelength, d is the interplanar spacing of the crystal and θ is the angle of incidencenoa (c). The XRD patterns presented in this thesis were obtained using a Bruker-AXS D8 Advance X-ray diffractometer with $CuK\alpha 1$ ($\lambda = 1.5406$Å).

2.4.3 Steady-State Electroluminescence Spectroscopy

Electroluminescence (EL) is a very important characterization technique to obtain the emission wavelength of a LED. Before each EL measurement, a 532 nm green laser is generally used to calibrate the spectrometer so that the EL spectrum obtained is accurate every time. For the EL measurement, the LED sample is placed at the entrance of the spectrometer ensuring the maximum coupling efficiency from the light collection to the spectrometer. EL spectrum provides important information on the specific emission wavelength, color purity, and brightness of the device [Ma]. For the equipment used in this thesis, a Jobin-Yvon iHR320 triple-grating spectrometer equipped with a Synapse silicon CCD array is used. The laser used to calibrate the setup is a 250 mW 532 nm TORUS laser purchased from Laser-Quantum Inc.

2.4.4 Scanning Electron Microscopy

Scanning Electron Microscope (SEM) is a microscope that produces images by scanning the sample surface with a beam of electrons [Goldstein *et al.*]. The electrons interact with the atoms in the sample producing various signals containing information about the surface morphology and composition of the sample [noa (q)]. The resolution of the acquired image is defined by the diameter of this focused electron beam. SEM can offer a resolution as high as 1 nm depending on the instrument, the electro-optical system, and the energy of the electrons [Sunaoshi, Kaji, Orai, Schamp & Voelkl]. SEM is more convenient and compatible with surface morphology and cross-section measurements and can be used to measure organic thin films. However, the conductivity of the organic sample is still a limiting factor because the electron charging on the measured surface can reduce the image contrast. For SEM observation, a thin film of $PEDOT : PSS$ or perovskite is deposited on a highly conductive substrate, FTO or ITO. The SEM is used to obtain date of the surface and cross-section of the devices in this thesis. The SEM images acquired in this thesis are taken by a Hitachi SU 8230 ultra-high-resolution field emission scanning electron microscope.

2.4.5 Profilometry For Film Thickness Measurement

A profilometer is a measuring instrument used to measure thin film thickness. To prepare the samples for profilometry characterization, the thin film is scratched using a sharp blade to create a clean step. The Dektak XT profilometer measures a step-change by dragging a diamond tipped stylus across the sample surface. The sample surface and cut clean step cause the stylus to move up and down while the movement is measured and recorded electrically by the machine. The measurement height ranges from 10 nm to 66 μm with a resolution of 10 nm.

2.4.6 LED Characterization

The power-current-voltage (PIV) characteristic is the most basic and important parameter for a LED. Many other important parameters can be calculated based on this information, such as EQE (%), luminance (cd), current efficiency (cd/A) and power efficiency ($lumens/W$). The PIV setup includes a Keithley 236 with a GPIB connector, a photodetector (Thorlabs, S120VC, $200 - 1100nm$, $50mW$), and an energy meter module (Thorlabs, model PM100USB). The Keithley 236 and the energy meter module are both connected to a computer where software is installed to record the generated testing data. Figure 2.12 is a cartoon representing the basic setup.

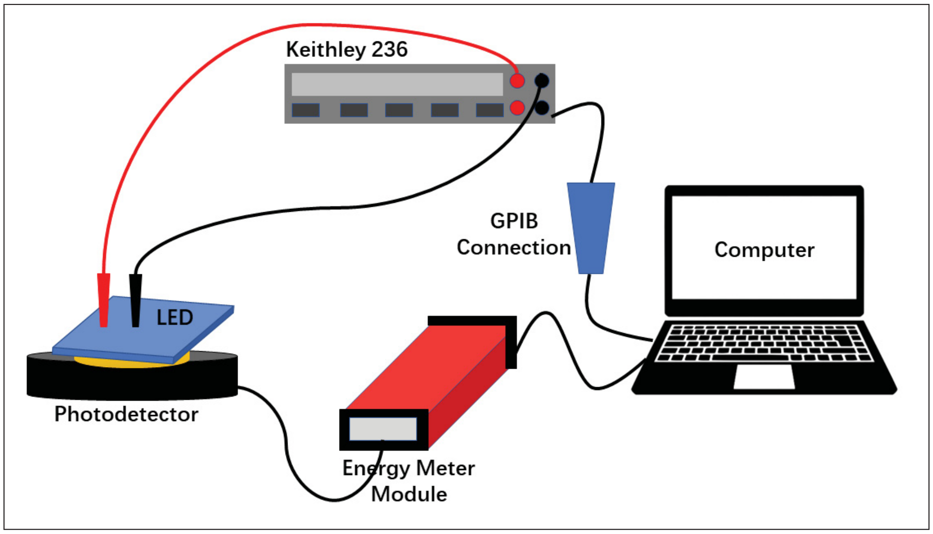

Figure 2.12 Power-current-voltage characterization setup configuration, adapted from [Ma].

After obtaining the PIV data, the EQE of the LED can be converted by the calculation shown in the equation below:

$$EQE = \frac{n_{photon}}{n_{electron}} = \frac{power/E_{photon}}{I/q} \tag{2.2}$$

E_{photon} is the photon energy which can be calculated by using hc/λ where we use the fluorescence peak wavelength λ_{peak} for the λ in the calculation. I is the current obtained from the PIV characteristic and q is the electron charge.

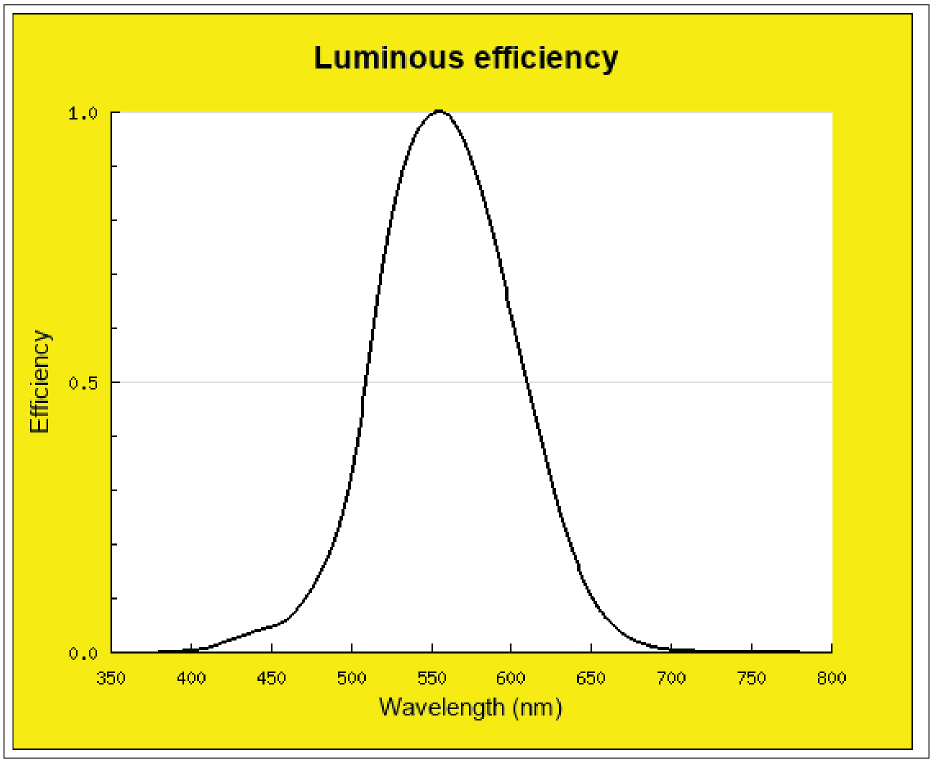

Figure 2.13 Standard luminosity function [noa (i)].

Apart from the EQE, the luminance efficiency is also very important because it provides information about the brightness of a light source concerning human eyes. The sensitivity spectrum for the human eyes is demonstrated by the standard luminosity function [noa (i)] as shown in Figure 2.13. The equation used to convert the output power (W) into luminance (cd) is presented below [Ma]:

$$I_v = \frac{683.002}{2\pi} P_{\text{out}} \int_{380}^{780} \overline{EL(\lambda) \times E_{\text{photon}}(\lambda)} \times \overline{y(\lambda)} d\lambda \tag{2.3}$$

where I_v is the luminance in cd, P_{out} is the device output power in W obtained from the PIV characteristics. $\overline{y(\lambda)}$ is the data from the standard luminosity function, $EL(\lambda)$ is the spectrum measured from the EL setup and $\text{E}_{\text{photon}}(\lambda)$ is the energy of photon at each wavelength.

The current efficiency, η_{current}, in cd/A can be calculated by:

$$\eta_{\text{current}} = \frac{I_{\text{v}}}{I} \tag{2.4}$$

and the power efficiency, η_{power}, in $lumens/W$ is calculated as:

$$\eta_{\text{power}} = \frac{2\pi I_{\text{v}}}{VI} \tag{2.5}$$

where I_v is the luminance in cd, I is the current and V is the applied voltage.

2.4.7 Photodetector Characterization

Comparing to LED devices, photodetector has more characterization values to examine its performance, such as current-voltage (IV) characteristics, rise (T_r) and decay (T_d) time, responsivity (R_λ) and external quantum efficiency (EQE) [Asuo *et al.* (b)].

The IV characteristics of the photodetectors are performed by using a Keithley 2400 source measuring unit (SMU) while under illumination (A.M. 1.5G) with a Newport solar simulator. The voltage applied to the photodetector varies from −4 to 4 V. The photocurrent gain from light to dark at −4 V is calculated as follows:

$$I_{photo}(gain) = \frac{I_{light}}{I_{dark}} \tag{2.6}$$

There are two ways to measure the T_r and T_d for a photodetector, such as excitation by a pulsed laser, or manually periodically turning on and off the solar simulator while recording the responses electrically. It is a measurement of how fast a photodetector can respond to the changes by the input of light intensity. Three to four periods are generally performed during the measurement to ensure the data quality. The measured shape looks similar to a square wave [Asuo *et al.* (b)].

External quantum efficiency (EQE) is a value that indicates how efficient the photogenerated electron-hole pairs are compared to the incident photons. It can be described numerically as the equation below:

$$\eta_{\text{current}} = \frac{\text{\# of electron } - \text{ hole photogenerated pairs}}{\text{\# of incident photons}} = \frac{I_P/q}{P_{in}/hv} \tag{2.7}$$

where I_p is the photodetector output photocurrent, q is the electron charge, and P_in is incident light power to the device. Figure 2.14 shows a cartoon schematic describing the equipment setup for the photocurrent characterization.

Responsivity (R_λ) is an important characteristic of the photodetector which has a close relation to the EQE. It measures the electrical output per optical input [noa (p)]. The equation to calculate the responsivity is:

$$R_\lambda = \frac{I_P}{P_{in}} = \frac{\eta q}{hv} \quad [\text{A/W}] \tag{2.8}$$

where η is the EQE value calculated using Equation 2.7.

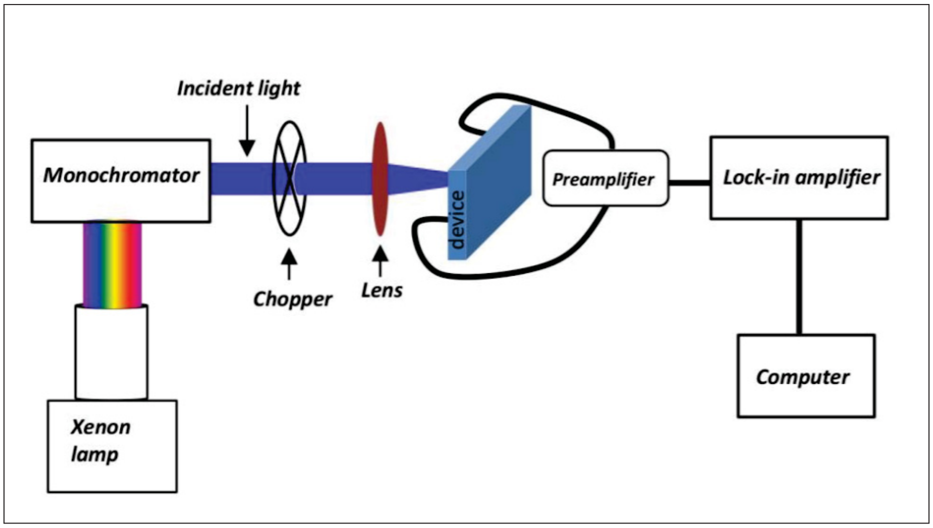

Figure 2.14 A cartoon schematic describes our in lab setup for the photocurrent measurement [Ka *et al.*]

CHAPTER 3

PEROVSKITE LED

3.1 Introduction

Lately, remarkable developments have been realized for solution-based organo-inorganic halide perovskite materials along with ABX_3 as their general chemical formula. It has many promising optical and electrical properties, such as tunable bandgap, long free-carrier diffusion length, high quantum yield and high charge carrier mobility [Chen *et al.* (a)][Zhang *et al.* (b)][Konstantakou & Stergiopoulos][Le *et al.* (a)][Yang *et al.* (d)][Zhang, Kuang & Wu (a)]. After only over a decade since its first development [Kojima *et al.*], perovskite-based solar cells with solution-processed have exceed power conversion efficiency of 25% [Green *et al.*]. Organo-inorganic halide perovskite is regarded as one of the most promising candidates for low-cost renewable energy shortly. These materials can also provide great performance for other optoelectronic applications besides the solar cells, such as LEDs [Liu *et al.* (d)][Shan *et al.*][Ercan *et al.*][Vashishtha *et al.* (b)], photodetectors [Tong *et al.*][Liu *et al.* (a)][Jing *et al.*] and lasers [Dong, Zhang, Liu, Yao & Zhao (b)][Shang *et al.*]. Their excellent properties including low-cost, low exciton binding energies and tunable emission are especially attractive for the fabrication of new generations of LEDs [Wang *et al.* (d)][Zhao, Lee, Roh, Khan & Rand (a)][Sutherland & Sargent][Vashishtha *et al.* (a)][Xu *et al.*][Zhao & Tan]. Perovskite-based LEDs have a general structure of an intrinsic active layer sandwiched between a hole injection layer and an electron injection layer [Sum & Mathews]. The electron and holes are injected into the active layer where they can meet and recombine radiatively under forward bias [Quan, Arquer, Sabatini & Sargent]. Small crystal grain, pinhole-free and uniform- & densely-packed films are necessary to achieve high efficiency [Wang *et al.* (b)][Cho *et al.* (a)][Tsai *et al.*][Xiao *et al.*].

Even though single- double- or triple cation doped perovskite exhibits improvements on both the stability and device performance [Cho *et al.* (b)][Kim *et al.* (d)]; extrinsic and intrinsic instabilities of perovskite itself introduces a poor stability under ambient conditions that remains to be a major impediment towards commercialization [Zhang *et al.* (d)][Arora *et al.* (a)][El-Mellouhi, Bentria, Rashkeev, Kais & Alharbi]. As a result, rapid decomposition from the perovskite materials into optically-inert constituents is observed under ambient environment processing, such as PbI_2 [Berhe *et al.*]. Tremendous efforts have been carried out in an attempt to overcome this problem. Triple-cation perovskite are discovered as a promising candidate due to their low sensitivity to processing conditions [Stolterfoht *et al.*][Wang *et al.* (a)][Wang *et al.* (f)]. In addition, the implementation of Cs^+ as a third cation into FA/MA based perovskite is found to have both improved purity and stability of the perovskite film [Saliba *et al.*][Azam *et al.*]. $FA/MA/Cs$ perovskite can crystallize into two different phases, including non-photoactive non-perovskite hexagonal δ-phase (yellow phase) and photoactive perovskite α-phase (black phase) [Stoumpos *et al.*][Eperon *et al.*][Lee *et al.* (c)]. The yellow phase impurities would limit the charge collection by affecting the morphology and crystal growth of the perovskite that need to be avoided [Saliba *et al.*]. The success mixture of MA/FA represents that small cation MA can act as a stabilizer for the black phase of the FA perovskite [Pellet *et al.*]. Comparing to the ionic radius of MA (2.70 Å) and FA(2.79 Å), Cs has the smallest of 1.81 Å[Amat *et al.*]. Moreover, the incorporation of Cs into FA perovskite had shown improved structural stability and stimulated black phase crystallization because of the entropic stabilization [Yi *et al.*].

In this chapter, we will demonstrate the fabrication and characterizations of the triple-cation perovskite-based LEDs in which the perovskite material synthesis and device fabrication/operation/characterization are all performed under ambient conditions. LEDs operating at 750 nm are first fabricated and tested with a maximum EQE of 3.1 %. The perovskite film is shown to be compact but with large crystal grains. Then we modified the crystallinity of the perovskite film by adding DMF additive into the perovskite precursor where the perovskite films show smaller grain size and less film thickness with the same degree of compactness. As a result, we can fabricate LEDs with another 90 % improvement in EQE reaching 5.9 % with the same peak emission wavelength.

3.2 Materials Synthesis and Device Fabrication/Characterization Methods

The perovskite synthesis and device fabrication are all performed under an ambient environment at 22 °C and 50 % relative humidity. Lead thiocyanate is added into the triple-cation perovskite to make it more stable under ambient environments [Asuo *et al.* (a)]. For the triple-cation perovskite solution synthesis, $0.8M$ of PbI_2, $0.5M$ of $PbBr_2$, $1M$ of FAI, $0.2M$ of $MABr$ and $0.6M$ of MAI are all dissolved in the solution made by $4:1$ DMF:$DMSO$ (volume ratio). Then 70 µl of cesium iodide solution is added to the perovskite solution followed by 60 minutes of slow stirring with no heating. To improve the performance of the LEDs, different perovskite solutions are developed by adding DMF into the original perovskite precursor in volume ratio forming 87.5% ($DMF : precursor = 7 : 1$), 80% ($DMF : precursor = 4 : 1$), and 66.6% ($DMF : precursor = 2 : 1$). Together with the 100% perovskite precursor, all these four perovskite solutions are used to fabricate four different LEDs.

For the LED device fabrication, the FTO-coated glass substrates (Ossila S304, 12 – 14 Ω/sq) are ultrasonically cleaned using acetone and isopropanol (IPA) for 10 minutes in sequence. Then the diluted $PEDOT : PSS$ (CleviosTM P VP AL 4083) with isopropanol in 1 : 3 volume ratio is spin-coated atop of the FTO substrates for 40 s at 3000 rpm followed by 200 °C annealing for 15 minutes in air. The thickness of the $PEDOT : PSS$ layer is approximately 150 nm measured using a profilometer. Before the deposition of perovskite film, UV treatments are performed using a UV lamp (405 nm, 6 W) for 15 minutes for better surface wettability. After the treatment, the perovskite film is deposited atop the $PEDOT : PSS$ layer in a two-step spin-coating mode. First perovskite solution is spin-coated at 2000 rpm for 20 s, then a none-stop solvent-anti-solvent treatment using ethanol and chlorobenzene mixture is performed at 5000 rpm for 20 s to achieve a well-crystallized and compact perovskite thin film. The samples are subsequently annealed on a hotplate at 120 °C for 15 minutes for the conversion of the perovskite. Once the samples have cooled down, $10mg/ml$ of $F8$ in chlorobenzene is spin-coated atop of the perovskite film at $4000rpm$ for $30s$ followed by a 15 minutes annealing at 80 °C. Finally, a 5 nm of MoO_3 layer and a 150 nm of the silver electrode through a $0.025cm^2$ shadow mask are thermally evaporated at a speed of 0.2 Å/s.

Hitachi SU 8230 ultra-high-resolution field emission SEM is used to acquire the SEM images. XRD patterns are recorded using BrukerAXS D8 Advance X-ray diffractometer with a CuK1 source (= 1.5406 Å). PerkinElmer Lamba 750 spectro-photometer is used to obtain the UV-vis optical absorption spectrum. Ambios XP200 is the profilometer used to determine the thin film thickness where the scanning speed is $0.03 mm/s$ and the stylus force is 0.03 mg. Jobin-Yvon iHR320 triple-grating spectrometer with Synapse silicon CCD array equipped is used to record the steady-state electroluminescence. The emitting power of the perovskite LED is measured through a photodetector (Thorlabs, S120VC, 50 mW, $200 - 1100$ nm) connected with an energy and power module (Thorlabs, PM100USB). The IV characteristics are obtained using LabVIEW controlled Keithley 2400 source-measure unit. The IV characteristics and emitting power measurements are performed at the same time, to calculate the EQE of the LEDs using the equation listed below:

$$EQE = \frac{n(\text{photon})}{n(\text{electron})} = \frac{P/E(\text{photon})}{I/q} \tag{3.1}$$

P is the output power measured using the photodetector in W, I is the corresponding current measured at the same time in A, q is the electron charge and E(photon) is $1.2398/\lambda$ (μm) where λ is the peak emitting wavelength.

3.3 Perovskite Crystallinity Improvement Analysis

The first step to analyzing the spin-coated perovskite film is to obtain its SEM images to check the formation of the perovskite grains. Figure 3.1 is a combined SEM image of the perovskite film fabricated with 100% perovskite solution. Figure 3.1a shows that the film is very compact; however, the perovskite grain size is considerably large. Figure 3.1b presents that the film has an average grain size of approximately 680 nm with 1230 nm as the largest grain. Unlike the solar cell application, small grains are necessary to spatially confine the charge carriers for efficient radiative recombination for the LEDs [Cho *et al.* (a)][Zhao *et al.* (b)][Xiao *et al.*]. Besides the grain size, the thickness of the active layer is crucial to the performance of the LEDs due to the considerably low carrier mobilities. The lack of active materials would limit the emission of the LEDs if the active layer is too thin; additionally, carriers would be lost due to the none-radiative recombination of electron and hole pairs if the active layer is too thick [Liu, Gangishetty & Kelly (b)].

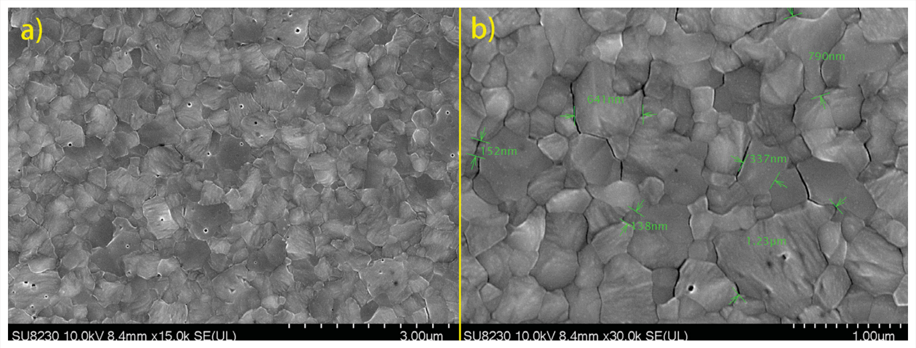

Figure 3.1 *SEM* images of the 100% perovskite solution. (a) *SEM* image with a scale bar of 3 µm. (b) *SEM* image of measured perovskite grain size with a scale bar of 1 µm.

We have developed a cost-effective approach to reducing both the perovskite grain size and active film thickness (under the same spin-coating speed) while maintaining its high compactness. Three additional perovskite solutions are prepared by adding *DMF* into the original (100%) perovskite precursor in volume ratio, forming 87.5%, 80% and 66.6% perovskite solution. Figure 3.2 and Figure 3.3 represent the comparison of these four perovskite films and their measured grain size respectively.

Figure 3.2 reveals that the coverage for all the perovskite films is homogeneous and complete. We can conclude that adding DMF into the perovskite precursor with different volume ratios does not have any influence on the compactness of the perovskite film as well as the appearance of the pin-holes. Figure 3.3 is a representation of the grain size measurements for all the perovskite film with a scale bar of 1 µm. ImageJ, a computer freeware, is used to measure the grain size which ranges from 90 nm to 1230 nm. The average grain size value is calculated by averaging 50 data points and the detailed values are listed in Table 3.1. The average crystallite grain diameter and (corresponding film thickness using the spin-coated speed of 4000 rpm for 100%,

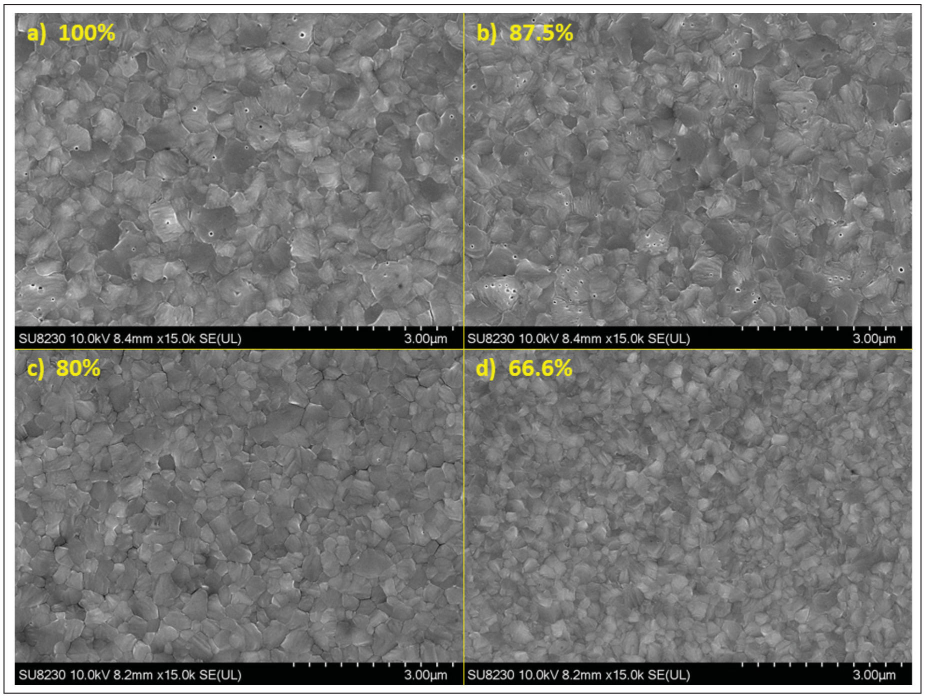

Figure 3.2 Comparison of SEM images for four different perovskite solution in volume with a scale bar of 3 µm. (a) 100%, (b) 87.5%, (c) 80%, (d) 66.6%.

87.5%, 80% and 66.6% are 674 nm (290 nm), 616 nm (190 nm), 537 nm (160 nm) and 402nm (100nm) respectively. These measured average values support the claims of the grain size and film thickness reduction by adding DMF into perovskite precursor.

Table 3.1 Average grain size values and thickness under 4000rpm spin-coating speed for 100%, 87.5%, 80% and 66.6% perovskite film.

	100%	**87.5%**	**80%**	**66.6%**
Average Grain Size (nm)	674	616	537	402
thickness (nm)	290	190	160	100

In addition to the grain size and thickness measurements, XRD and UV-vis have been also performed to analyze the quality and the bandgap for these four different perovskite films. Figure 3.4 is the XRD patterns using 100% sample as the reference. The y-axis shows the XRD intensities for different samples by count. Overall, the XRD patterns represent the perovskite

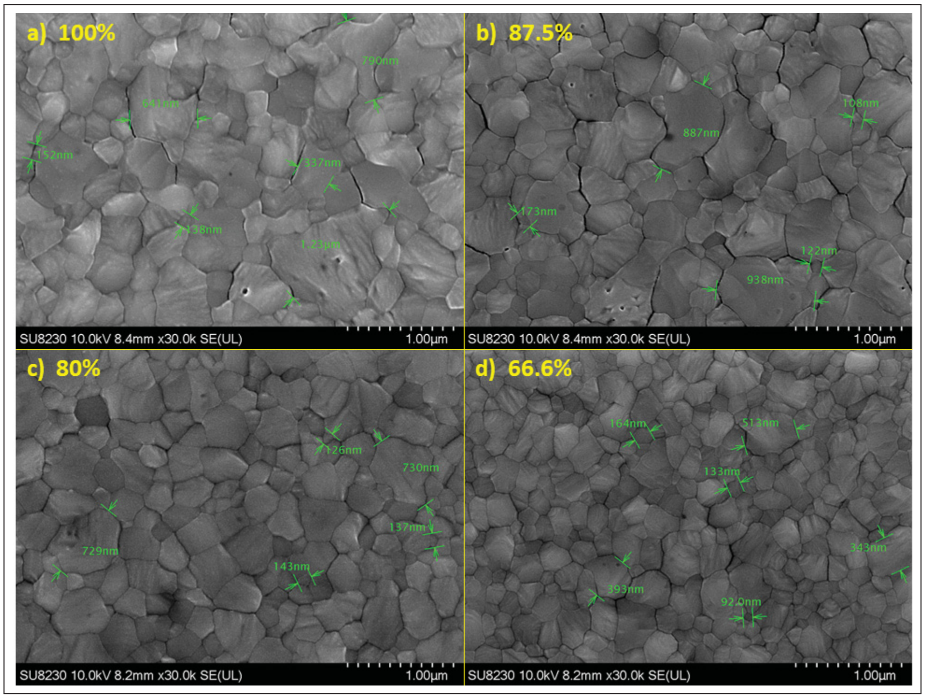

Figure 3.3 SEM images of the perovskite film with the scale bar of 1 µm with some measured grains. For average size data collection, the ImageJ is used to measure the grain size from these SEM images. (a) 100%, (b) 87.5%, (c) 80%, (d) 66.6%.

films are highly crystallized. The perovskite materials are crystallized in the tetragonal phase with a space group of I4cm(108) and lattice parameters of $a = b = 8.86$ Åand $c = 12.65$ Årespectively [Kim, Im & Park (c)][Asuo *et al.* (b)]. The consistencies of the XRD-specific peaks at 14.15°(110) plane and 28.55°(220) plane show no clear consequences on the peak-shifting by introducing the DMF additive. Table 3.2 represent the FWHM values and the crystallite size in nm for each batch of the perovskite samples at 110 and 220 respectively. Scherrer's equation is used to estimate the FWHM values of the 110 peak. The FWHM values of the 110 plane vary between 0.19°and 0.24°. Therefore, the crystallinity of the perovskite films is maintained even upon introducing the DMF additive. The peak at 26.5°(marked as in Figure 3.4) refers to the FTO substrate which is more pronounced for the 66.6% film because of its low film thickness. Figure 3.5 shows the $UV - vis$ optical absorption spectroscopy for the perovskite thin films. The bandgap of the 100% perovskite is 1.68 eV while the rests are approximately 0.01 eV larger which lies within the margin of error.

Table 3.2 FWHM and the calculated crystallite size for each perovskite batch.

Angle	FWHM	Crystallite Size (nm)
100%		
14.11 (110)	0.23515	33.65007
28.52 (220)	0.33579	24.13005
87.5%		
14.14 (110)	0.28118	28.1426
28.56 (220)	0.41317	19.61255
80%		
14.13 (110)	0.23947	33.04377
28.54 (220)	0.31926	25.38002
66.6%		
14.14 (110)	0.19069	41.4983
28.59 (220)	0.191	42.42834

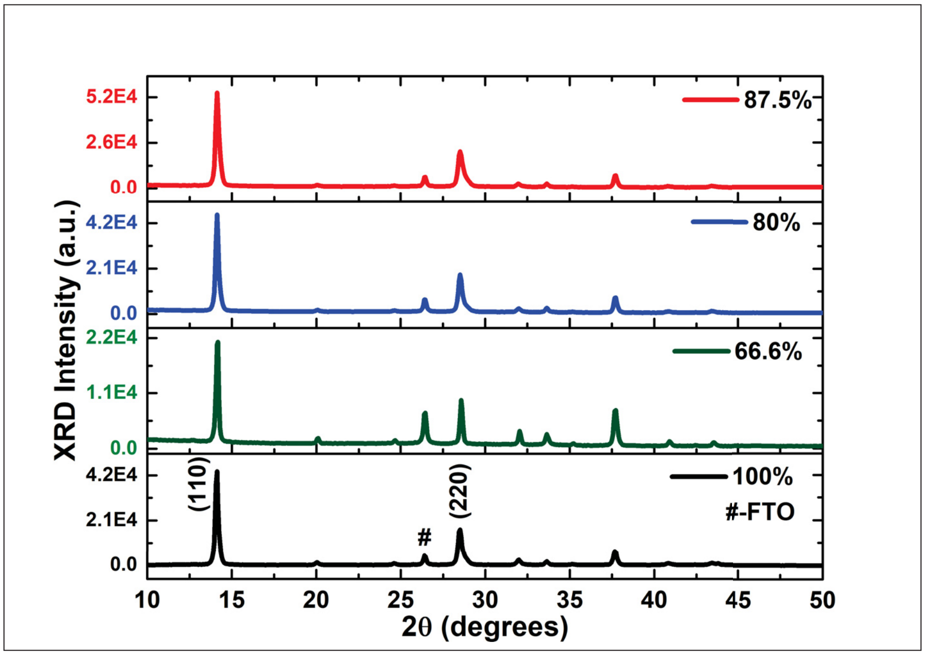

Figure 3.4 X-ray diffraction patterns for 100%, 87.5%, 80% and 66.6%.

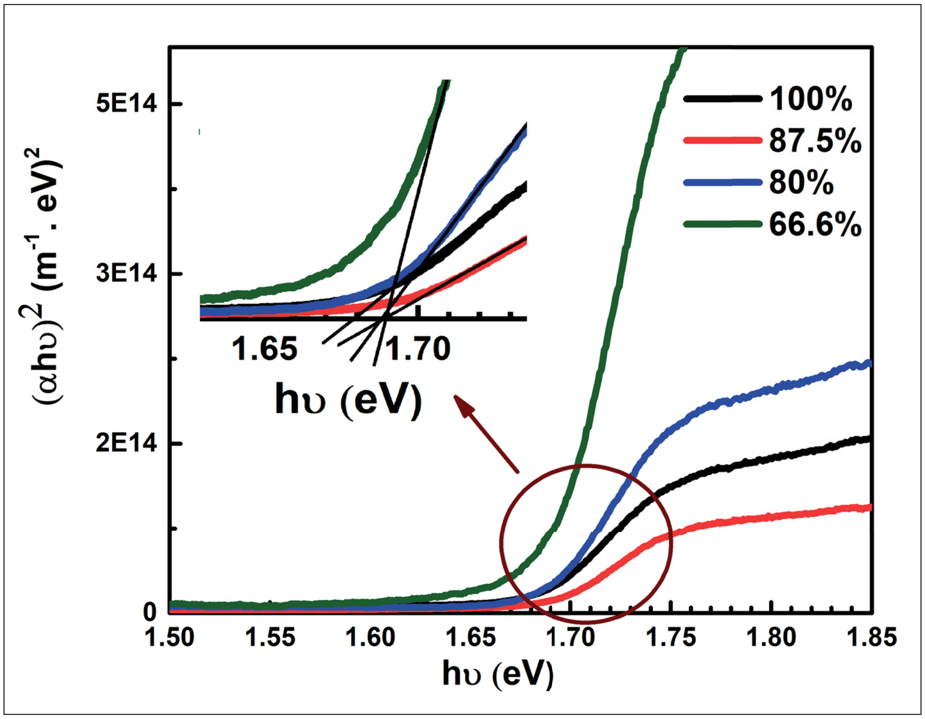

Figure 3.5 Tauc plot of the perovskite thin films. The inset is the bandgap assessments from the linear extrapolation.

To provide a better understanding, Figure 3.6 is plotted which contains the average grain size, film thickness, and XRD peak intensities as a function of the perovskite concentration. The average grain size (green plot) and film thickness (blue plot) are using the y-axis on the right. The red y-axis on the right corresponds to the XRD peak intensities. Based on the characterizations of the perovskite materials, we can conclude so far that 80% perovskite could bring the best performance of the fabricated LEDs.

3.4 Perovskite NIR LED

3.4.1 LED Device Architecture

A simple three-layer architecture ($PEDOT : PSS/Perovskite/F8$) sandwiched between electrodes is used to fabricate NIR perovskite-based LED devices as shown in Figure 3.7a. FTO and MoO_3/Ag are used as cathode and anode respectively where MoO_3/Ag system has a high-

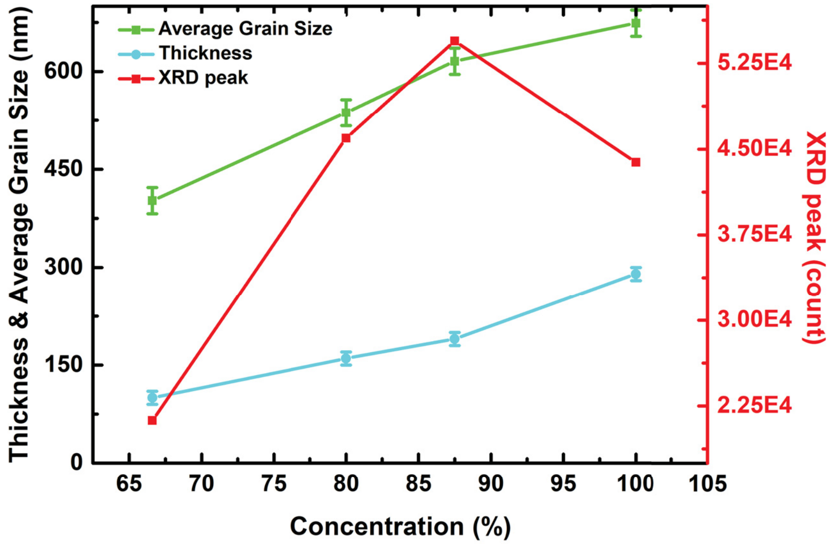

Figure 3.6 Perovskite film characterizations including average grain size, film thickness and XRD peak intensities at 14.15% as a function of the perovskite concentration.

workfunction providing ohmic hole injection into the LED device [Lu, Kabra, Johnson & Friend (b)]. *F*8 is a polyfluorene conjugated polymer that is chosen to form a heterojunction with perovskite film. This heterojunction acts as a carrier-blocking structure to prevent the quenching of the light emission at the contact interfaces and electrical shorts through the perovskite layer [Hoye *et al.*][Tan *et al.*]. Figure 3.7b shows the energy band diagram of the designed perovskite LED.

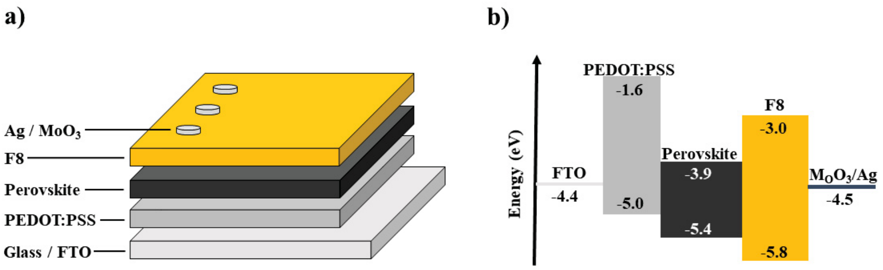

Figure 3.7 (a) Schematic of the perovskite LED device structure. (b) Its energy band-diagram.

3.4.2 LED Device Characterizations

For the consistency study, a comparative statistical analysis for over 50 LEDs in total by the measurements of the electroluminescence intensity is performed as shown in Figure 3.8. The box for each sample group indicates the LEDs lay within the $2^n d$ and $3^r d$ quartile (25% to 75%). The solid lines on the top and bottom of the box represent the maximum and minimum while the ones lay within the box represent the median for each sample group. This statistical analysis combined with the perovskite film characterizations in Figure 3.6 suggests that 80% perovskite yields the best trade-off between the thickness and the quality of the perovskite film. The performance of the LEDs decreases significantly when perovskite is diluted further with DMF. It is because of the reduced crystallinity of the perovskite film and insufficient perovskite materials for light emission. From the film thickness perspective, a lower perovskite film thickness compared to 100% and 87.5% reduces the carrier losses transportation and provides a better balance between electron and holes favoring exciton formation and radiative emission.

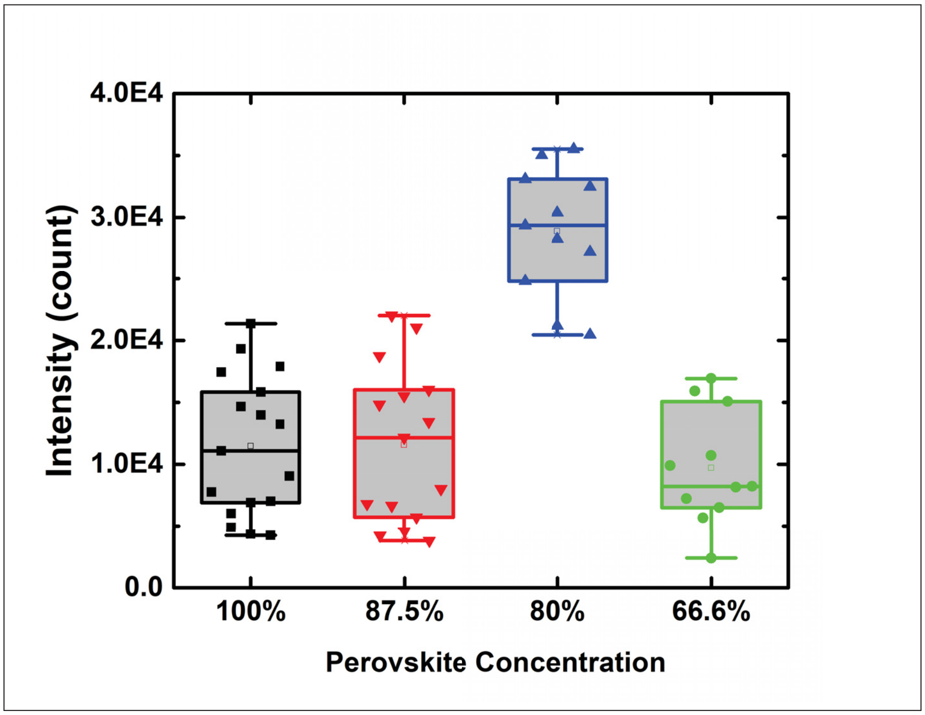

Figure 3.8 Statistical analysis for more than 50 perovskite LEDs in total by the electroluminescence intensity.

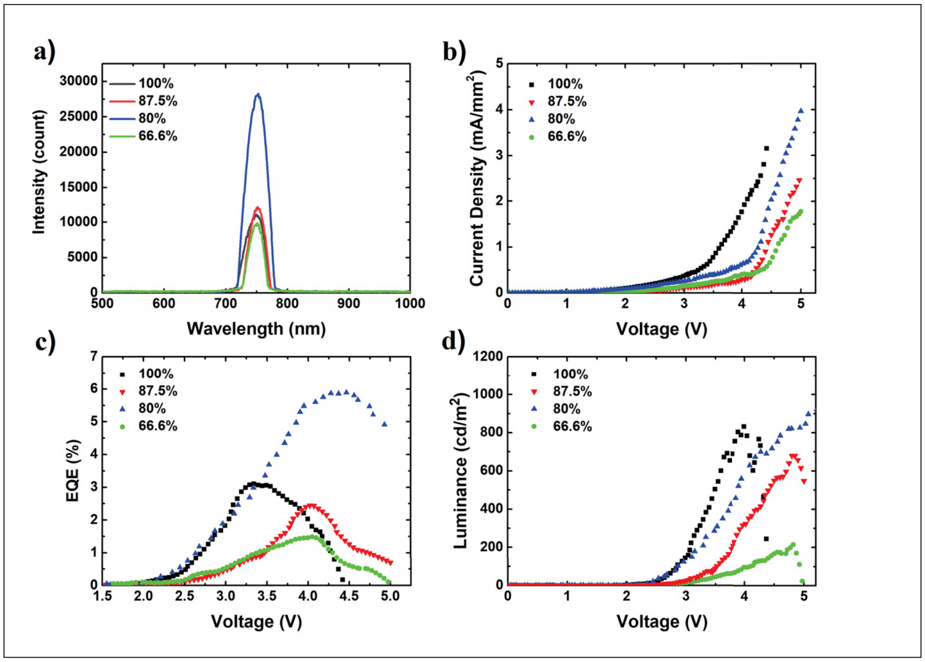

Figure 3.9 Electrical characterizations for the perovskite LEDs with different concentration, such as 100%, 87.5%, 80% and 66.6%. (a) Electroluminescence spectrum with a bias voltage of $4.5V$. (b) Current-density versus voltage ($J-V$) characteristics. (c) EQE versus voltage characteristics. (d) Luminance versus voltage characteristics.

Figure 3.9a is the electroluminescence spectra for fabricated LEDs with different perovskite concentrations. The emission peaks for 100%, 87.5%, 80% and 66.6% LEDs are 750, 751, 753 and 751 ± 2 nm respectively. Among them, 80% LEDs exhibit a significantly (about 3 times) stronger light emission. This could be explained by higher carrier delivery (thinner film) compared to 100% and 87.5% devices, and greater perovskite crystallinity than 66.6% devices. The $FWHM$ of the 80% LEDs' emission is 40 nm. The average $J-V$ characteristics for the three best devices from each concentration are indicated in Figure 3.9b. The turn-on voltage is slightly over 3 V for 100% LEDs and is approximately 4 V for 87.5%, 80% and 66.6% LEDs. When the applied voltage is increased beyond the turn-on voltage, the current density increase rapidly in a typical non-linear rectifying behavior for all devices. The peak current densities for 100%, 87.5%, 80% and 66.6% devices are 3.15, 2.46, 3.96 and 1.78 mA/mm^2. EQE versus voltage characteristics are summarized in Figure 3.9c. The maximum EQE are

3.1% (100% LED), 2.4% (87.5%LED), 5.9% (80%LED) and 1.5% (66.6% LED) plus a 10% error value. LEDs with 80% perovskite concentration exhibit a 90% increase in EQE compared to that of un-modified LED (100%). Luminance characteristics are represented in Figure 3.9d. The luminance drops dramatically for 100% LED after 4 V and 4.8 V for 87.5% and 66.6%. Perovskite LED with 80% concentration has the best performance of 986 cd/m^2 and continues working at $5V$. Table 3.3 summarizes the peak characterization values for all four sets of perovskite LEDs.

Table 3.3 Peak electrical characterization values for all four sets of perovskite LEDs.

Concentration	**Electroluminance** (N.A.)	**Current Density** (mA/mm^2)	**EQE** (%)	**Luminance** (cd/m^2)
100%	11093	3.15	3.1	831
87.5%	12158	2.46	2.4	679
80%	28251	3.96	5.9	986
66.6%	9894	1.78	1.5	214

3.5 Conclusion

In this chapter, we have described a triple cation perovskite synthesis method and its customization for efficient NIR LED fabrication. All the devices are fabricated in an ambient environment incorporating thiocyanate ions and solvent-anti-solvent treatment techniques. We demonstrate that we can significantly improve the EQE of fabricated LED devices from 3.1% to 5.9% by perovskite crystallinity modification techniques. By introducing DMF additive into the perovskite precursor, key characteristics of the perovskite film are optimized including the reduction of grain size and film thickness. At the same time, the modified films preserve their tetragonal halide perovskite morphology. To date, the best LEDs are fabricated with 80% perovskite solution with a maximum EQE of 5.9%. As a result, we believe the triple cation perovskite synthesis and perovskite modification technique represent an important step towards new low-cost perovskite LED fabrications and similar technologies for a wide range of energy-efficient applications, such as display, bio-sensing, and lighting.

CHAPTER 4

ELECTROSPRAYED MICOR-PARTICLE PLED

4.1 Introduction

PLEDs have generated a tremendous academic and industrial research interests for new generations of low-cost solid-state lighting devices and flat panel displays. PLEDs have many advantages, such as flexibility, solution-based fabrication and large-area scalability [Dai *et al.*][Wei, Ge & Voit (a)]. Liquid fabrication techniques are generally used for polymeric materials fabrication because of their high material yield, low cost and low-temperature processing [Ju, Yamagata & Higuchi (a)]. The first PLED that based on the poly-phenylenevinylene (PPV) material was reported approximately three decades ago [Burroughes *et al.*]. More recently, PLEDs using PFO [Yan *et al.*][Hasan, Sandberg, Nur & Willander], $F8BT$ [Ho *et al.*][Kabra *et al.*][Lu, Finlayson & Friend (a)] and $MEH-PPV$ [Gustafsson *et al.*] [Deng *et al.* (b)][Hewidy, Gadallah & Fattah] acting as blue-, green and red-emitting polymers are developed respectively [Song, Kim, Lee & Moon]. The full-color displays have been achieved by the mixture of blue-, green- and red-emitting polymers [Zheng *et al.* (a)][Yu][Zheng *et al.* (b)].

To fulfill the potential of PLEDs, such as high efficiency, long operation lifetime, and high thermal stability, a multi-layer structure is generally required [Zhou *et al.* (b)]. Such devices consist of an electron-injection layer, an electron-transporting layer, an emissive layer, a hole-transporting layer, and a hole-injection layer [Ràfols-Ribé *et al.*]. Most unfortunately, conjugated polymers have similar solubility in common organic solvents that create great difficulties in fabricating these multi-layered PLEDs. As a result, low performance for both polymer materials is introduced because the deposited underlying film will be partially dissolved and blended with the newly deposited material during the fabrication process [Ma]. A liquid buffer layer has been developed for multi-layer PLED architectures [Zheng *et al.* (a)][Tseng *et al.*][An *et al.*]; however, the number of layers is very limited since only very few solvents can be used to orthogonally dissolve common polymer materials [Zhou *et al.* (b)].

Electrospraying, a fabrication technique, is reported over a century ago [Zeleny]. It has been widely developed for the deposition of biological materials [Nguyen *et al.* (a)][Boda, Li & Xie], semi-conductive ceramics [Mokhtari, Latifi & Shamshirsaz], and polymers [Bodnár, Grifoll & Rosell-Llompart]. Electrospraying is a liquid atomization process using electrostatic forces to overcome the surface tension at the tip of a needle under high electrical potential [Lee, Koo & Cho (e)][Pitsalidis *et al.*]. Therefore, electrospraying is a promising fabrication technique that can lead to the formation of sub-micro- to nano-meter polymeric structures [Xie, Jiang, Davoodi, Srinivasan & Wang]. It also offers limitless possibilities for new technologies and materials targeting medical devices and micro-electronics [Zhu, Masood, O'Brien & Zhang (b)]. Recently, electrospraying has also been applied to the fabrication of organic LED devices [Lee *et al.* (e)][Hwang, Xin, Cho, Cho & Chae (b)][Sajid, Zubair, Doh, Na & Choi][Miyazaki & Koishikawa] and organic photovoltaic devices [Anjusree, Deepak, Nair & Nair][Hong *et al.*].

4.2 Materials and Fabrication Methods

4.2.1 Device Fabrication

The ITO coated glass substrates (Kintec Company, 15 Ω/sq) are cleaned ultrasonically using acetone, ethanol, and isopropanol in sequence for 10 minutes each. PEDOT:PSS solution (CleviosTM PVP AL 4083) is diluted $1:3$ volume ratio with isopropanol (IPA). Then the diluted $PEDOT:PSS$ solution is spin-coated atop the ITO coated glass at 3000 rpm for 60 s to achieve a uniform $PEDOT:PSS$ layer. A nitrogen-filled oven is used to anneal the samples for 20 minutes at 200°C. Next, TFB (American Dye Source, Inc.), as a hole-transporting material, is dissolved in the THF solvent at 4 mg/ml, weight concentration, and spin-coated atop the $PEDOT:PSS$ film at 3000 rpm.

For the red-light-emitting PLED, $MEH-PPV$ (American Dye Source, Inc.) is the only active material used. $MEH-PPV$ is dissolved in the THF solvent with a weight concentration of 4 mg/ml. Then the solution is electrosprayed atop the spin-coated TFB film forming an approximately 2 µm thick particle layer using the optimized parameters: 6 cm in distance, 10.5 kV of applied voltage, 2 ml/h of flow rate and 2 minutes of deposition time. After the electrospraying deposition, a 120 nm thick Al cathode is thermal evaporated through a shadow masking at 0.3 Å/s. The shadow mask has a dimension of $2mm$ by $2mm$.

For the other four different colors PLEDs, all the fabrication procedures, and electrospraying parameters are the same as the $MEH-PPV$ (G/R=0:1) PLED, except the material ratio and the deposition time of the active layer. The polymer material ratio is controlled only with the deposition time for the G/R=1:0, G/R=7:3, G/R=1:1, and G/R=3:7 devices. For example, G/R=7:3 device has a deposition sequence of $42s$ ($F8BT$-green), then-$18s$ ($MEH-PPV$-red), then $42s$ ($F8BT$-green) and finally $18s$ ($MEH-PPV$-red). In contrast, the alternating sequence $30s$(green) – $30s$(red) – $30s$(green) – $30s$(red) is applied for G:R=1:1 PLED. A $18s$(green) – $42s$(red) – $18s$(green) – $42s$(red) sequence is used for the G:R=3:7 PLED and $120s$(green) for the G:R=1:0 PLED.

4.2.2 Device Characterization

The electrosprayed particle layer is analyzed using an Olympus LEXT 3D microscope (OLS4100). Jobin-Yvon iHE320 triple-grating spectrometer with a Synapse silicon CCD array is used to record the steady-state electroluminescence spectra. The Keithley 236 is connected to a computer with a GPIB module, and the IV characteristics are recorded using a lab-made Labview program. The emitting power of the PLEDs is recorded using a photodetector (Thorlabs, S120VC, $200-1100$ nm, 50 mW) connecting through an energy and power meter module (Thorlabs, PM100USB). To calibrate, a commercial LED with known output power is used to obtain the attenuation factor before the characterization of the fabricated PLEDs.

4.2.3 Design of Experiments for Electrosprayed Particle Layer

Conjugated polymers have relatively low carrier mobilities, and the thickness of the electrosprayed particle layer is critical for the efficiency of the PLED devices [Kabra *et al.*]. There are many can affect the size of the electrosprayed particles as it is shown in Figure 4.1.

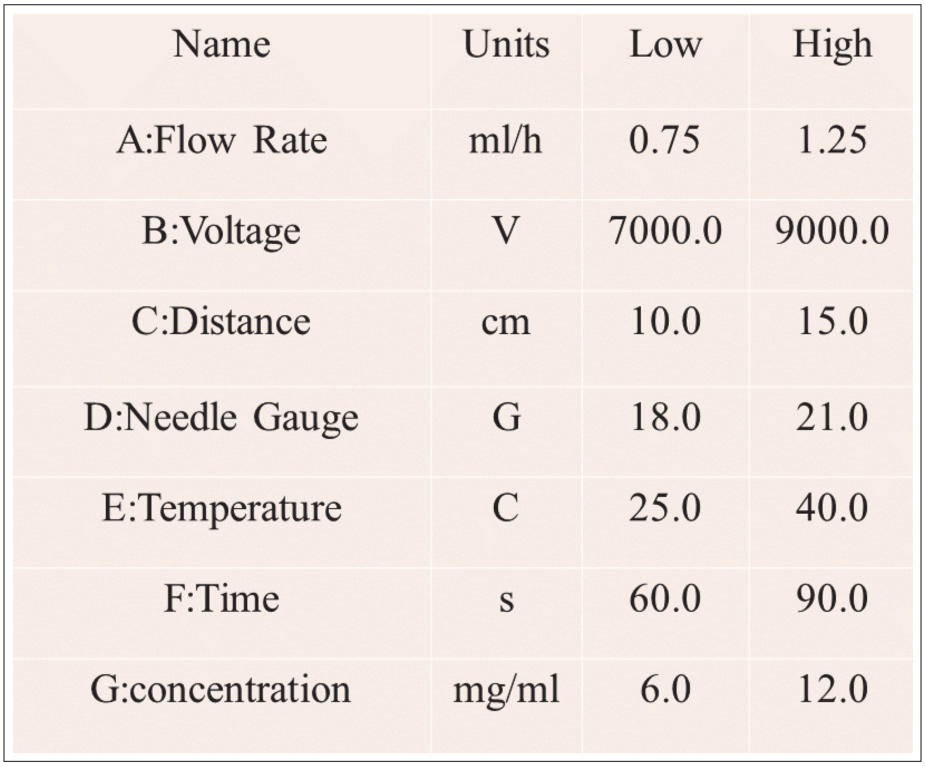

Name	Units	Low	High
A:Flow Rate	ml/h	0.75	1.25
B:Voltage	V	7000.0	9000.0
C:Distance	cm	10.0	15.0
D:Needle Gauge	G	18.0	21.0
E:Temperature	C	25.0	40.0
F:Time	s	60.0	90.0
G:concentration	mg/ml	6.0	12.0

Figure 4.1 Low and high values for the seven-parameter design of experiment

The flow rate represents how fast the solution flows through the needle. Voltage is controlled through the power supply. The distance is measured by the separation between the tip of the needle and the grounded metal collector. The gauge of the needle describes the size of the hole in the needle. The smaller the gauge, the larger the hole. Temperature expresses the temperature of the solution. Time represents the duration of the particle collection. The concentration of solution controls the viscosity. The higher the concentration, the larger the solution viscosity.

Seven parameters could impact the size of the electrosprayed particles. To eliminate the less-impacting parameters and discover the degree of influence of each parameter, we have implemented a design of experiments technique to solve these problems. Totally 32 runs are performed, recorded, and analyzed. The $3D$ image for each run is measured using a LEXT 3D microscope and the average height is determined over 100 particles through a computer freeware Digimizer. A standardized Pareto Chart for the height of the particle layer is represented in Figure 4.2. It shows the degree of impact on the particle layer height for each electrospraying parameter and their combinations. We can conclude from the chart that distance, concentration, and needle gauge are more important than the rest parameters.

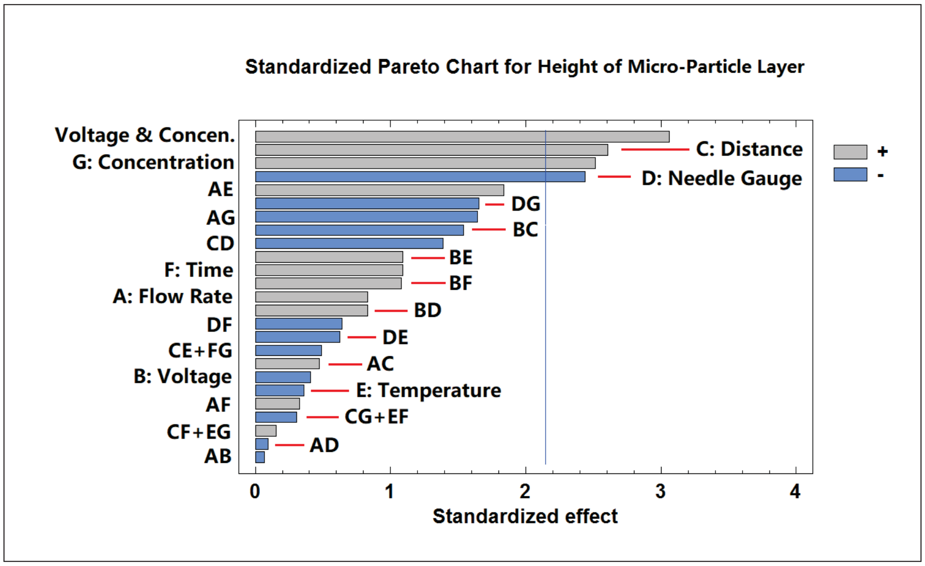

Figure 4.2 Standardized Pareto Chart for height of micro-particle layer with all the parameters and their different combinations.

Figure 4.3 shows the characterization result for the sample which has the minimum height among them all during this design of the experiment. Figure 4.3a is the 3D image and Figure 4.3b is the estimated response surface mesh analysis for the corresponding sample. In Figure 4.3a, the sample is 259 vt 259 µm and the height ranges from 0 to 13.7 µm. Figure 4.3b shows the height of the particles using a cuboid representation with distance, needle gauge, and concentration as its x-, y-, and z-axis respectively. The circled corner has the maximum particle height of 9.1 µm

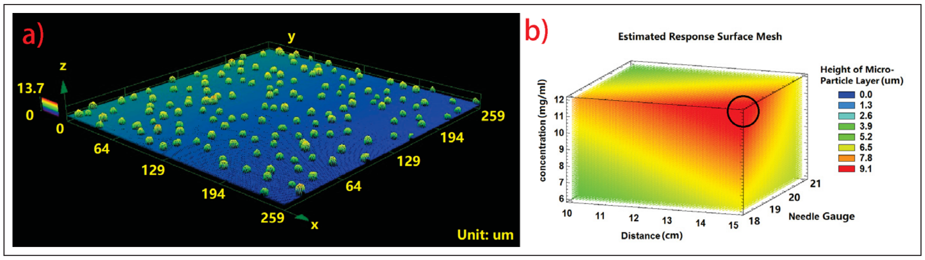

Figure 4.3 Characterization results for the minimum height of the 7-parameters design of experiment. (a) 3D images of the electrosprayed particle film. (b) The estimated response surface mesh analysis for the corresponding sample.

with a distance of 15 cm, needle gauge of 18, and concentration of 12 mg/ml. To achieve the minimum particle height, we need to target the complete opposite of the circled corner which indicates a smaller distance, a larger needle gauge and a lower concentration.

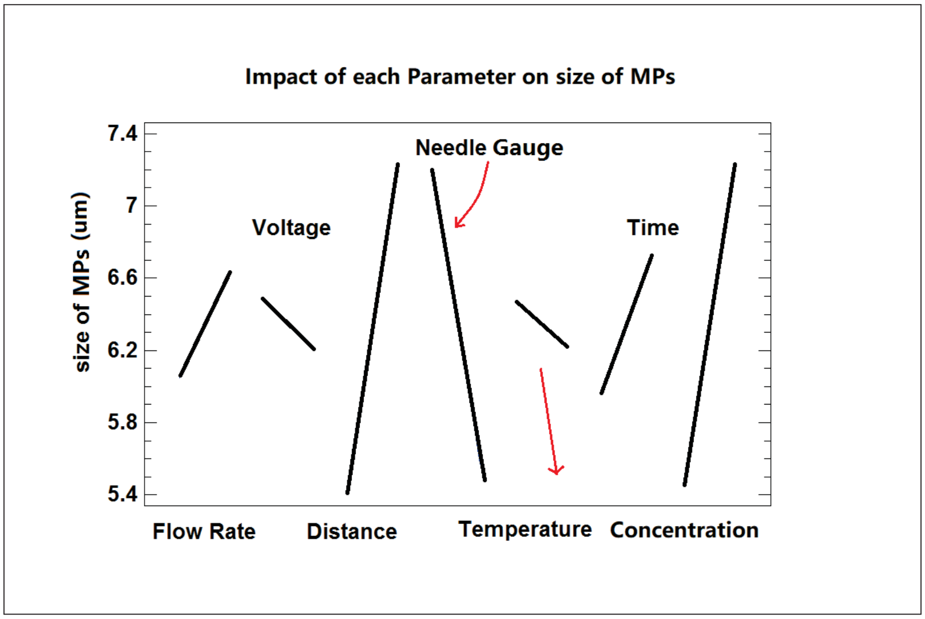

Figure 4.4 Effect of each experimental parameter on the size of the polymer particles. The length of each line relates to its degree of impact on the particle size, while the sign of the slope indicates whether the relationship is directly proportional (positive slope) or inversely proportional (negative slope)

Figure 4.4 presents the interrelation between each key parameter and the size of the particles. The length of the line describes the degree of impact on the particle size; for example, the longer line indicates the greater impact. Additionally, the sign of the slope for each line represents if the particle size is inversely or directly proportional to the given key parameters. The needle gauge controls the jetting cone. A small collection of particles would prefer needle with a smaller hole which means a larger needle gauge number. The concentration of the solution controls the quantity of the polymer materials at a given volume, and it also affects the solution viscosity and electrical conductivity. The concentration selected has little influence on the conductivity of the solution because the polymers are semi-conductive. We have also measured through a viscosity meter to conclude that there is no significant change in the viscosity for different designed concentrations. Therefore, a small concentration is preferred for the small-particle collections. The magnitude of the electrical field between the needle and metal collector is a crucial parameter in electrospraying. The applied voltage and distance have a tight inter-wined relationship to the electrical field. For a given voltage, a smaller distance would result in a higher electrical field and smaller particle collections; however, insufficient time for solvent evaporation could cause aggregation of wet particles. In addition, the electrosprayed materials could be lost to the surroundings if the distance is too large.

A new set of designs of the experiments is created targeting applied voltage, distance, a needle gauge, and concentration. Their designed low and high values are shown in Figure 4.5. After the characterizations of all the samples, the sample with the minimum particle size is selected. Its 3D scan and surface response mesh is represented in Figure 4.6. Figure 4.6a shows a 3D scan image by LEXT 3D microscope that is used to determine the average particle size. The sample has a dimension of 259 by 259µm. The color bar on the right is the scale of the height of the particles where the red color indicates a maximum height of 6.9 µm. The estimated response surface mesh for this set of designs of the experiments is presented in Figure 4.6b. Compared to Figure 4.3b, the area is circled in red indicates the minimum size of electrosprayed particles achieved. As a result, the desired values for these three main parameters are: 4 mg/ml

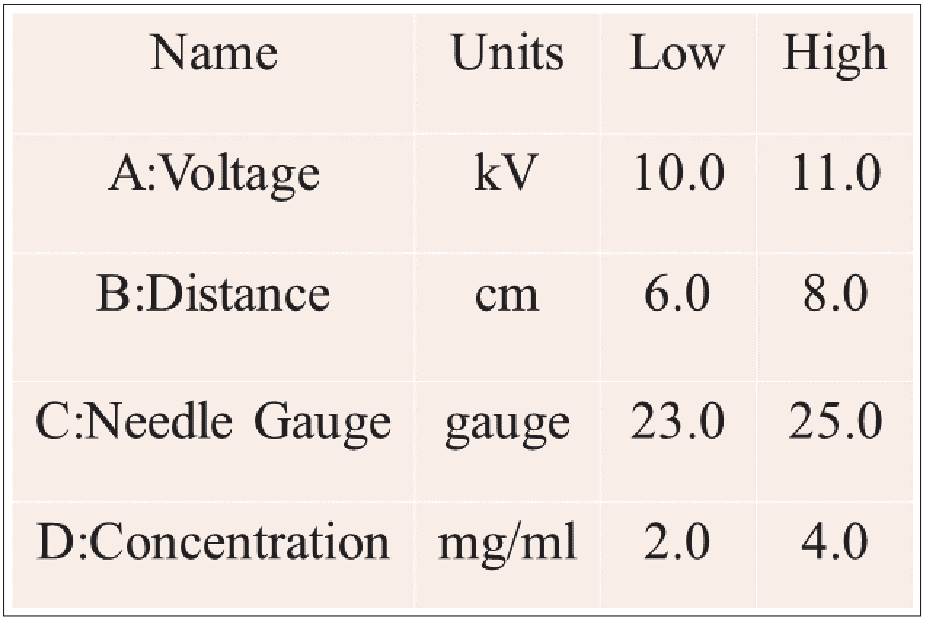

Name	Units	Low	High
A:Voltage	kV	10.0	11.0
B:Distance	cm	6.0	8.0
C:Needle Gauge	gauge	23.0	25.0
D:Concentration	mg/ml	2.0	4.0

Figure 4.5 Low and high values for the 4-parameter design of experiment

of concentration, 6cm of distance, and needle gauge of 25 with the applied voltage is fixed at 10.5 kV.

4.3 Single Color Light Emitting LED

Based on the ideal electrospraying parameters obtained, red-emitting PLEDs using $MEH-PPV$ particle layer are fabricated and tested. Figure 4.7a is the schematic representation of the red-emitting PLED architecture and Figure 4.7b is its corresponding energy band diagram. ITO and Al are acting as anode and cathode respectively. $PEDOT : PSS$ layer is used to smooth the surface roughness of the ITO electrode. TFB is the hole-transporting layer and $MEH-PPV$ is the electron-transporting layer. The injected electron and holes are radiatively recombined at the interfaces between the TFB and $MEH-PPV$ resulting in light emission.

Figure 4.8 is the electrical characterizations of $MEH-PPV$ based PLED. The normalized electroluminescence with its peak emission of 601 nm is shown in Figure 4.8a. The inset of Figure 4.8a represents the macroscopical picture of an operating red-emitting PLED. Figure

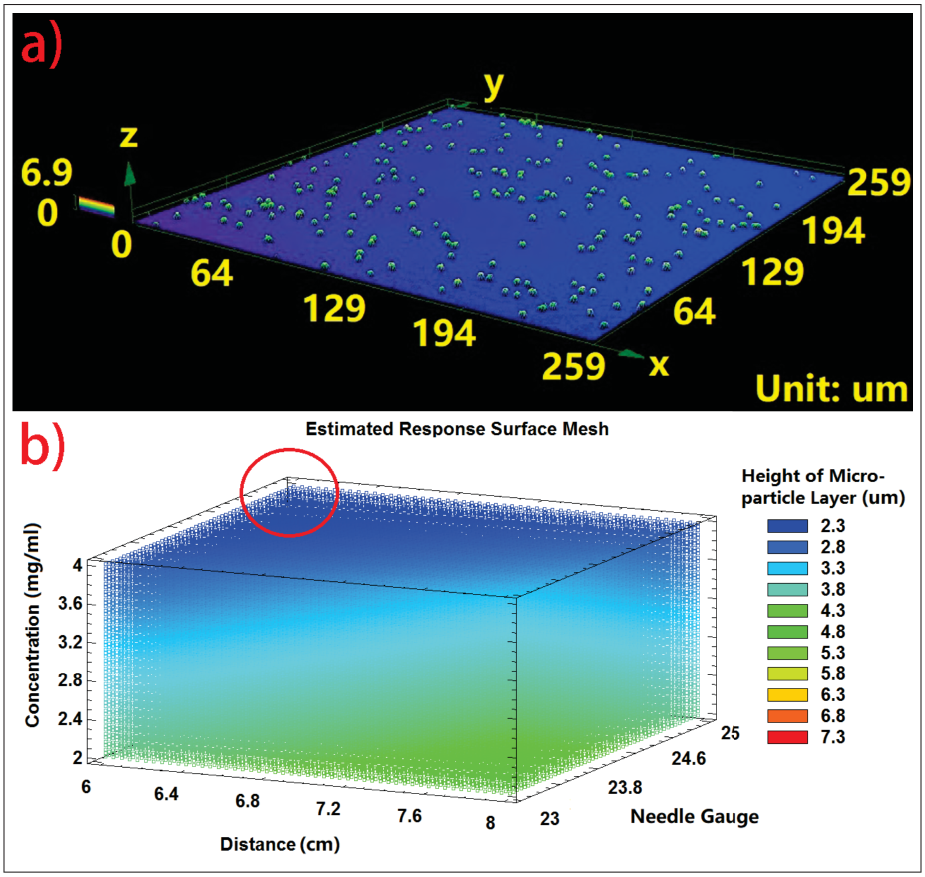

Figure 4.6 Characterization results for the minimum height of the four-parameters design of experiment. (a) 3D images of the electrosprayed particle film. (b) The estimated response surface mesh analysis for the corresponding sample.

4.8b shows the current density versus voltage characteristics where the device has a peak current density at 16.1 mA/mm^2 under a bias voltage of 13.5 V. Under a bias voltage of 13.5 V, the PLED reaches its maximum luminance of 475 cd/m^2 in Figure 4.8c. Finally, Figure 4.8d indicates fabricated PLED has a maximal EQE of 3.2%.

4.4 Color-Tunable LED

The specialties of the electrospraying fabrication technique, could be used to combine different conjugated polymer materials without acquiring any orthogonal solvents. Therefore, we have chosen to explore the combined deposition of both $MEH-PPV$ (red-emitting) and $F8BT$

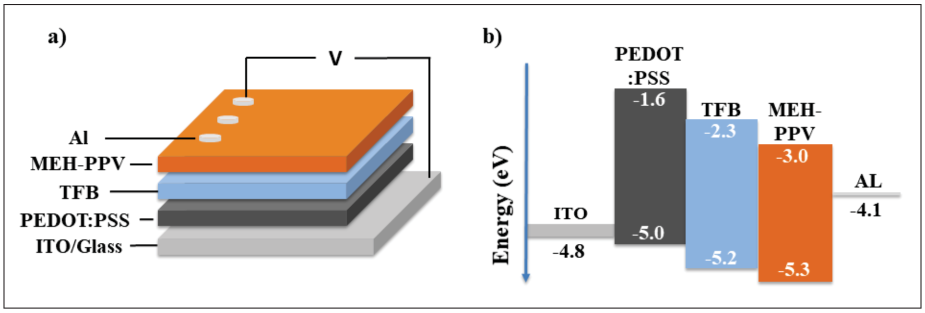

Figure 4.7 Structure of PLED using $MEH-PPV$ at the active material. (a) Schematic of the device architecture. (b) Its energy band diagram.

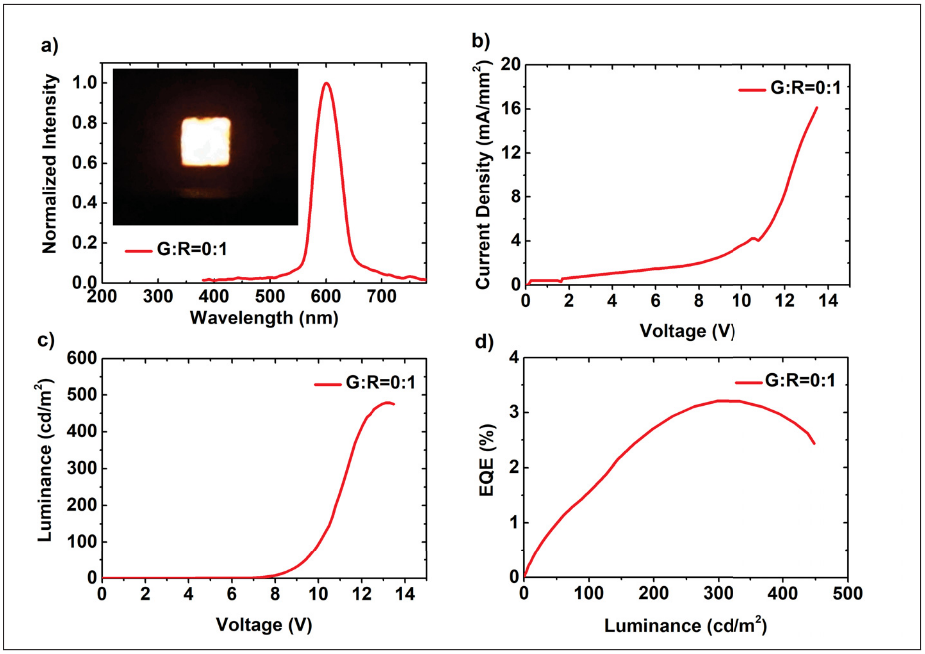

Figure 4.8 Electrical characterization of the red-emitting PLED (G:R=0:1). (a) Normalized electroluminescence spectrum. The inset image shows the PLED under operation. (b) Current density versus voltage characteristics. (c) Luminance versus voltage characteristics. (d) The evolution of the device EQE as a function of the luminance.

(green-emitting) particles on a single sample after the successful fabrication of red-emitting PLED via electrospraying.

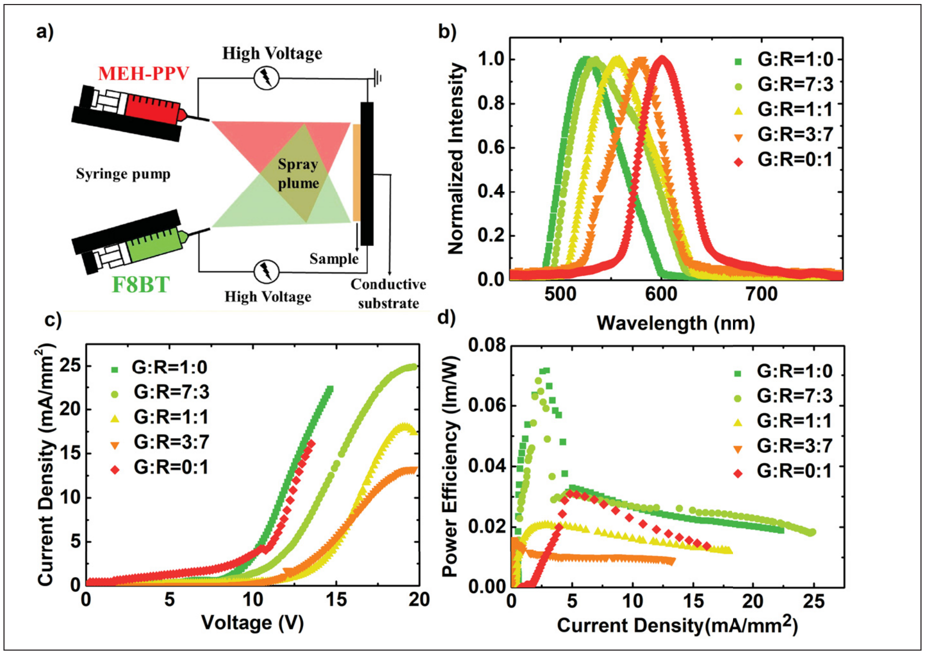

Figure 4.9 Electrical characterizations for all five color-emitting PLEDs. (a) A schematic representation of the electrospraying setup for the production of mixed polymer particles. (b) Normalized electroluminescence spectrum for 5 PLEDs. The set is an image focused on the sample surface for G:R=3:7 PLED in operating. (c) Current density versus voltage characterizations. (d) Power efficiency versus current density characterizations.

Figure 4.9 shows the electrical characterizations for all five different PLEDs. Figure 4.9a is the schematic representation of the electrospraying setup used to color-mixed PLEDs. Each color is controlled independently and all the electrospraying parameters for both color deposition are the same except for their own deposition time. The deposition time controls the relative ratio of the red-emitting and green-emitting polymer particles.

To show the level of control this approach can provide, another four different sets of devices are designed and fabricated. Their active materials compositions are 100% $F8BT$ (G:R=1:0), 70% $F8BT$ with 30% $MEH-PPV$ (G:R=7:3), 50% $F8BT$ with 50% $MEH-PPV$ (G:R=1:1), and 30% $F8BT$ with 70% $MEH-PPV$ (G:R=3:7). Their normalized electroluminescence spectra together with the red-emitting PLED are compared in Figure 4.9a. Their emission peaks are changing from green to red gradually where the peak values are $525nm$, $535nm$, $558nm$, $580nm$, and $601nm$ respectively. The right shoulder of G:R=7:3 at around $565nm$ and the left shoulder of G:R=3:7 at around 540nm indicate a less balanced mixture of $MEH-PPV$ and $F8BT$ particles. The inset of Figure 4.9a is an image of the orange PLED (G:R=3:7) in operating. The camera is set to focus on the light-emitting particles instead of its macroscopic sample surface when taking the picture. This inset image is a clear representation of the lighting spectrum shifting of the electrosprayed particle blends. For example, a yellow-light emission is achieved when the green and red light-emitting particles contribute equally (G:R=1:1) to the PLED emission. As for the unbalanced particle ratio, green and red light-emitting polymer particles dominate the PLED emission for the sample G:R=7:3 and G:R=3:7 respectively. Figure 4.9c presents the current density versus voltage characteristics for all five PLEDs. From the plotted data, PLEDs with mixed particles require higher bias voltage to reach comparable currents compared to pure color PLEDs. It is likely caused by the electrical field interaction between two needles causing lower uniformity of the samples. Figure 4.9d illustrates that green PLED has the highest power efficiency and the power efficiency tends to decrease when $MEH-PPV$ particles are introduced.

The standardized CIE diagram containing all five PLEDs color points is presented in Figure 4.10a. The CIE coordinates are generated using an online freeware [noa (g)]. The detailed CIE coordinates for five PLEDs ordering from green to red are (0.26,0.66), (0.35, 0.60), (0.41, 0.57), (0.46, 0.50) and (0.58, 0.40) respectively. A black dot line is drawn to connect the green and red coordinates. As we can see, the rest three PLED coordinates fall gradually onto the dotted line indicating the balanced color mixture. Figure 4.10b shows a combined picture of five PLEDs under operation. The gradual change of colors, ranging from green to red, can be easily distinguished. The different shape of the red PLED compared to the rest is due to the different shapes of shadow masks that are used at these two different stages of research.

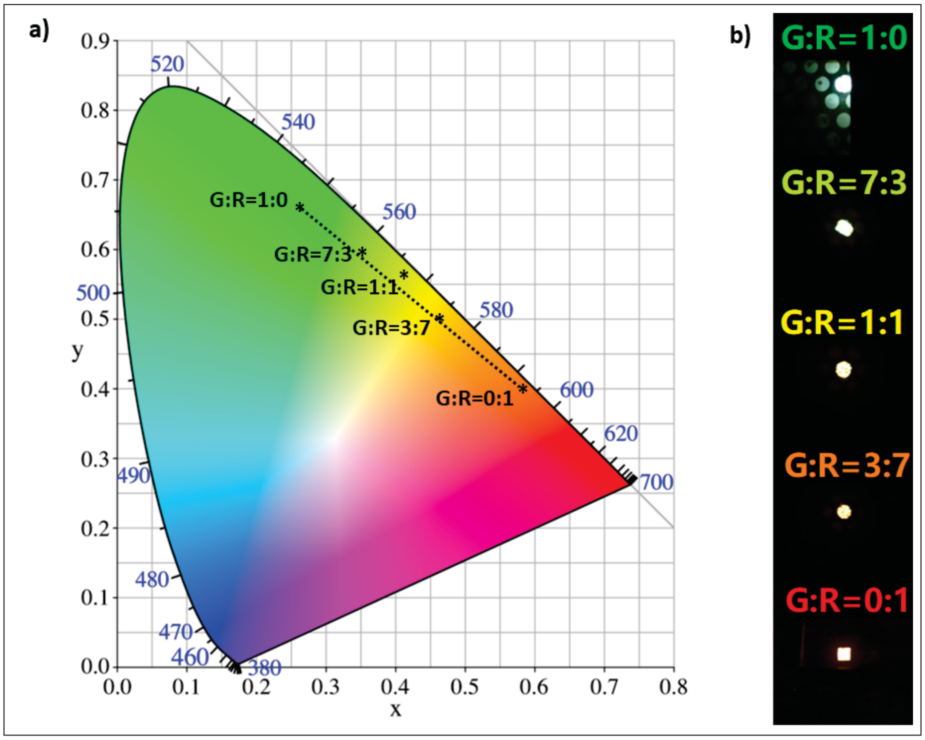

Figure 4.10 Emission color characterizations for all five PLEDs. (a) CIE diagram containing all five coordinates. (b) Pictures of the PLEDs under operation.

4.5 Conclusion

In summary, we successfully represent that facile PLED fabrications can be achieved with carefully optimized electrospraying. Two sets of designs of experiments followed by statistical analysis are performed to identify the main electrospraying parameter in the beginning. Then red-emitting PLEDs using $MEH-PPV$ particles are fabricated and characterized based on the obtained ideal set of electrospraying parameters as a proof of concept. Finally, we demonstrate the ability to mix $F8BT$ (green-emitting) and $MEH-PPV$ (red-emitting) particles to tune the device emission. Even though the overall performance of these PLEDs is still modest and the uniformity of the mixed particle layer is relatively difficult to control; we still believe that this approach proposes a new paradigm for simple hybrid multi-polymer-based optoelectronic devices fabrication with controllable properties. Hence, we believe that it could lead to a brighter future for low-cost, multi-layered PLED devices.

CHAPTER 5

INKJET PRINTED SI-BASED PHOTODETECTORS

5.1 Introduction

A photodetector is a device that converts an optical signal into an electrical signal. It has been used for a wide of applications in various fields including chemical/biological detection [Kelley *et al.*][Kumar, Bhatt, Abhyankar, Yun & Jeong], optical communication [Yang *et al.* (c)], image sensing [Wang *et al.* (c)] and environmental monitoring [Ju *et al.* (b)]. Nowadays, inorganic material based photodetectors prepared with germanium (Ge), silicon (Si) or their compounds are dominating the commercial photo-detection market due to their fast response speed [Yang *et al.* (a)], high gain-bandwidth [Surendran *et al.*] and high stability [Liu *et al.* (a)]. Compared to the inorganic materials, the technological advantages and numerous desirable properties provided by organic semiconductor materials, such as large area scalability, low cost, compatible with flexible substrate and solution process, could greatly promote the development of high-performance optoelectronic devices [Miao & Zhang]. However, the poor carrier mobility of most organic semiconductor materials (10^{-3} $cm^{-2}V^{-1}S^{-1}$) comparing to those of inorganic materials (10^{4} $cm^{-2}V^{-1}S^{-1}$) would cause rather long RC-time, longer response time and poor frequency response [Meskers, Duren, Janssen, Louwet & Groenendaal][Vuuren, Armin, Pandey, Burn & Meredith]. In addition, inorganic materials exhibit a much higher stability especially in the moist environment [Liang *et al.*]. silicon is the most abundant inorganic semiconducting material on earth. Porous silicon nano-structures have gained interest due to their high surface-to-volume ratio, easy fabrication process, a single-crystal structure similar to the bulk silicon, and cost-effectiveness [Banerjee, Asuo, Pignolet, Nechache & Cloutier (a)]. These excellent properties make it a suitable material candidate for photodetector device fabrication. A hybrid photodetector combining advantageous characteristics of both organic and inorganic materials could be a solution in developing a highly efficient photodetector to realize the optimal photoelectric conversion. Poly(3,4-ethylene-dioxy thiophene) ($PEDOT$) is one of the most suitable materials among numerous conducting polymers based on its excellent properties including high conductivity, high stability, moderate band gap and broad adsorption [Liang *et al.*][Friedel *et al.*]. Porous silicon nano-structures have gain interests due to its easy fabrication process, high surface to volume ratio, single-crystal structure similar to the bulk silicon and cost-effectiveness [Banerjee *et al.* (a)]. Surface plasmon has been widely used to improve the characteristics of photodetectors [Miao *et al.*][Jia *et al.*][Kaur, Yadav & Mitra]. Embedding of localized surface plasmon (LSP) effect of noble metal nanoparticles is an efficient technique to enhance the light absorption through coupling, between metal nano-particles and the incident light, due to its unique features including light trapping, strong absorption, improved sensitivity, and high efficiency [Li *et al.* (a)][Chandrakalavathi, Peta & Jeyalakshmi]. Metallic nano-particles that support LSPs, such as Pt [Guo *et al.* (b)], Al [Bao *et al.*], Ag [El-Mahalawy & Wassel] and Au [Goswami *et al.*], exhibit many beneficial characterizations including scattering cross section, enhanced local electrical field and increased optical absorption [Qu *et al.*][Sellappan *et al.*]. Among all the above mentioned metallic nano-particles, Ag nano-particles were extensively utilized and considered to be a better plasmonic material owning to their exceptional features,including high density of plasmonic electric field, flexibly in maintaining resonant frequency and low loss [Li *et al.* (a)][Besteiro, Kong, Wang, Hartland & Govorov][Sundararaman, Narang, Jermyn, Goddard Iii & Atwater][Lin *et al.*]. Previous reports establish that the incorporation of Ag nano-particles into the devices could bring a 20-fold responsivity enhancement [Li *et al.* (a)]. Also, a self-powered photodetector (UV-photodetector) employing Ag/SiO_2 core-shell nano-particles and achieved a high on/off ratio of 8212 [Huang *et al.*].

Compare with conventional fabrication methods, such as dip-coating [Shen, Yuan, Zhong & Tian], spin-coating [Dou *et al.*], and blade coating [Deng *et al.* (a)], the implementation of printing techniques into optoelectronic device fabrications have become a surging field in both academic and industrial research. The most utilized electronic printing techniques are inkjet [Liu *et al.* (e)], aerosol [Gupta, Arunachalam, Cloutier & Izquierdo], flexo [Krebs, Fyenbo & Jørgensen], gravure [Secor *et al.*] and screen printing [Shaheen, Radspinner, Peyghambarian & Jabbour]. Among them, inkjet printing is a flexible, digital, and additive printing technique with many advantages including low temperature, no material waste, precise fabrication, able to deposit various materials that can be dispersed in the solution, and compatible with a wide range of substrate, over a large area [Azzellino *et al.*][Alamri, Leung, Vaseem, Shamim & He]. A wide range of materials have been adapted to compatible with inkjet printing, such as organic molecules, sol-gel metal oxides, polymers, metallic ceramic nano-particles and carbon / post carbon nano-materials [Arias, MacKenzie, McCulloch, Rivnay & Salleo][Aleeva & Pignataro][Kamyshny & Magdassi][Secor & Hersam]. Previous reports have demonstrated the optimization of inkjet-printed PEDOT:PSS thin film [Xiong & Liu]. Later, a Ag grid/ITO hybrid transparent electrode using inkjet printing proves the concept of inkjet printed Ag electrode which can be used as an electrode for optoelectronic devices fabrication.

Reliability, performance, and economics are all important for the further advancements in photodetector research and industry; in this work, we demonstrate fully inkjet printed self-powered photodetectors based on (1) pristine silicon substrate, (2) porous silicon substrate and (3) Ag nano-particles embedded on porous silicon substrate. The Ag nano-particles are fabricated by controlling the cleaning procedure after the galvanic displacement method (GDM) [Liu, Qu, Zhang, Tan & Wang (c)][Banerjee, Trudeau, Gerlein & Cloutier (b)][Kawasaki *et al.*]. Their surface morphology and light absorptance are characterizaed. A $PEDOT : PSS$ layer is first printed atop of different silicon substrates, followed by the Ag contacts printed on top. Photodetectors with different types of silicon substrates are characterized and compared. The photodetector with Ag nanoparticles embedded porous silicon exhibits the best performance, which has more than two orders of magnitude in photocurrent enhancement. This effective printing fabrication technique and the simple device structure are promising for the future of low cost, efficient and stable photodetector devices.

5.2 Fabrication and Characterization Methods

5.2.1 Synthesis of porous silicon and silicon with Ag nanoparticles.

Silicon with porous nano-structure is synthesized using a metal-assisted wet electroless chemical etching technique on a commercial low-doped $n-type$ silicon wafer (UniversityWafers, $1-10$ Ω-cm). The silicon wafer is cut into around 4 cm^2 and cleaned by ultra-sonication with acetone, IPA, and ethanol in sequence for 15 mins each. Afterward, the samples are rinsed with DI water and blow-dried using a nitrogen gun. The etchant solution is prepared by the mixture of $0.01M$ of $AgNO_3$ solution and $4.8M$ aqueous hydrogen fluoride (HF) solution in a $1:1$ volume ratio. The cleaned silicon samples are immersed in the prepared etchant solution for 15 mins in the ambient environment. Then the etched samples are cleaned with a 70% nitric acid (HNO_3) for 1 h in ambient condition followed by the DI water wash and N_2 blow dry for porous silicon only samples preparation. As for the porous silicon samples with Ag nanoparticles attached, the last cleaning protocol should be neglected. Finally, all the samples are treated using a 20% HBr solution for 2 mins to remove any native oxide layers atop the nano-structured silicon.

5.2.2 Formation of Hybrid Heterojunction

The samples are cleaned with DI water and blown to dry. The $PEDOT:PSS$ (Clevious 4083) is inkjet printed atop the various types of silicon substrate using Ceradrop (X-serie). The $PEDOT:PSS$ layer is printed with centered square lattice formation, splat diameter of 34 µm, and 125 µm raster overlapping. The high raster overlapping ensures good coverage and uniformity for only one $PEDOT:PSS$ layer printing. During the printing, the printing bed is heated at 50°C. The detection resolution is 15 µm and the tolerance is 5 µm. The $PEDOT:PSS$ is then annealed at 200°C for 15 mins on a hotplate after the printing is finished.

5.2.3 Ag Finger Gird Structure

Ag pads and fingers are printed via Ceradrop (X-serie) to serve as the contacts of the photodetectors. The dimension of the pad size is 1.5 mm on x-axis and 8 mm y-axis. The distance between pads is 4 mm. The width of the fingers is 0.04 mm and the spacing between them is 0.8 mm. Because of the formation difference between Ag pads and fingers, different inkjet printing parameters are applied to ensure the optimal structure and connection. There is only one printed layer for both Ag pads and fingers. For the Ag pad printing, square lattice formation and splat diameter of 51 µm are used. The printing direction is along the positive y-axis. The Ag fingers are printed with a square lattice and splat diameter of 40 µm. Since the set splat diameter is the same as the width of the fingers; therefore, to ensure a smooth finger line formation, a diamond filling strategy is applied. The diamond filling is meaning that every other Ag droplet is deposited onto the substrate. Therefore, each Ag printed finger would require two passes to finish. The detection resolution and tolerance are 15 µm and 3 µm respectively for both pad and fingers. Throughout the entire Ag printing process, the printing bed is heated to 50°C. To cure the printed Ag ink and finalized the device fabrication, the devices are annealed at 140°C for 30 mins.

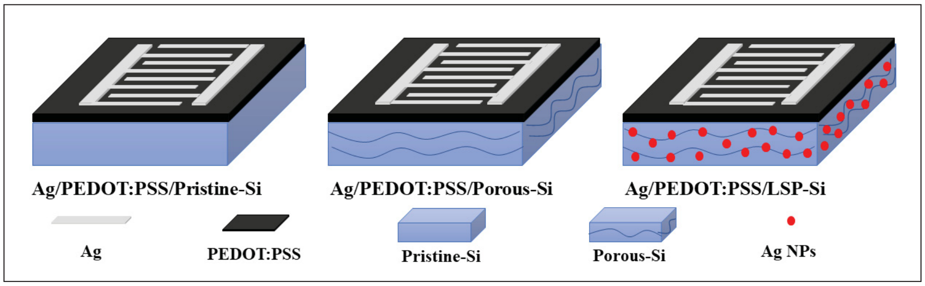

Figure 5.1 Schematic structure of the photodetectors with different types of Si substrate, such as pristine-Si, porous-Si and porous-Si with Ag nano-particles embedded.

The architecture of the photodetectors is represented in Figure 5.1. In general, $PEDOT:PSS$ is printed atop the silicon substrate, and then Ag finger electrodes are printed atop of the

$PEDOT : PSS$ layer. Three batches of photodetectors are fabricated based on different types of silicon substrate, such as pristine-Si, porous-Si and porous-Si with Ag nano-particles embedded.

5.2.4 Materials and Device Characterization

The SEM characterizations of the various types of silicon substrates are performed by using a Hitachi SU-8230 field emission scanning electron microscope (SEM). PerkinElmer Lamba 750 spectro-photometer is used to obtain the UV-vis optical absorption spectrum. The current-voltage (IV) characteristics of the photodetector are performed by using a Keithley 2400 source measuring unit (SMU) under A.M. $1.5G$ illumination with a Newport solar simulator. The transient photo-response is measured by manually periodically turning on and off the solar simulator while recording the responses electrically. The photocurrent spectral measurement of the device is characterized using a TRIAX320 monochromator, a chopper, and a lock-in amplifier.

5.3 Results and Discussions

Three batches of hybrid photodetectors are fabricated; they are $pristine - Si$, nanostructured-Si ($porous - Si$), and Ag nano-particles induced LSP effects enhanced nanostructured Si ($plasmonic - Si$). The $pristine - Si$ batch is used as the reference for comparison. To investigate their surface morphology, SEM images for the sample surfaces are taken for each batch as shown in Figure 5.2. Figure 5.2a, 2b and 2c shows the surface SEM images for $pristine - Si$, $porous - Si$ and $plasmonic - Si$ respectively. The uniformly distributed white small dots in Figure 5.2c are the Ag nanoparticles.

Figure 5.3 is the $UV - VIS$ characterizations of the different silicon substrate surfaces to discover their light reflections. The x-axis is the wavelength in nm. The y-axis is the light reflection in percentage. As shown in Figure 5.3, the $pristine - Si$ batch has the highest reflection of 65% at around 370 nm with its average light reflection is above 40%. Compared to the $pristine - Si$ substrate, $porous - Si$ and $plasmonic - Si$ have a much lower light reflection. $Plasmonic - Si$

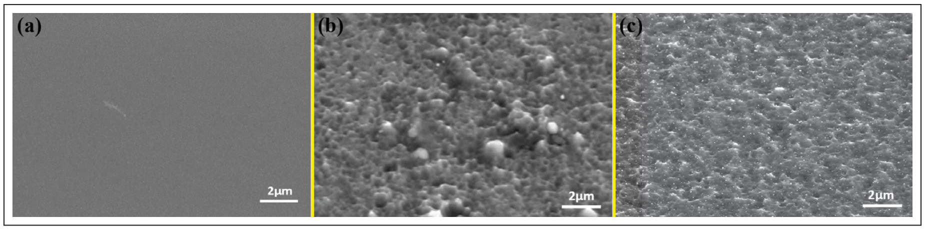

Figure 5.2 SEM images for different types of Si substrates with a scale bar of 2 μm. (a) $PristineSi$ substrate. (b) $Porous - Si$ substrate. (c)$Plasmonic - Si$ substrate

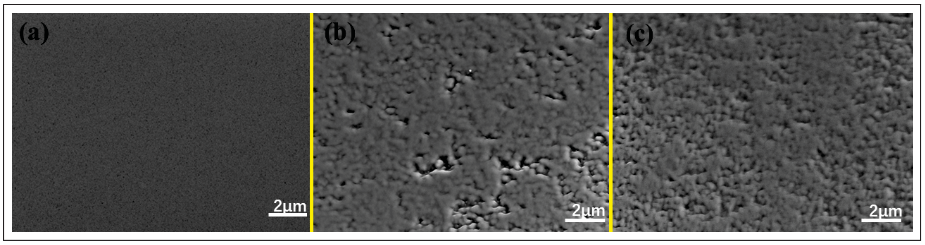

Figure 5.3 SEM images for $PEDOT : PSS$ coated silicon substrates. (a) $PEDOT : PSS$ coated $pristine - Si$. (b) $PEDOT : PSS$ coated $porous - Si$. (c) $PEDOT : PSS$ coated $plasmonic - Si$

substrate has the lowest light reflection with its average value of 5.5%. Therefore, photodetectors with $plasmonic - Si$ may have the best performance among them all because of its highest light absorption. Figure 5.4 shows the SEM images for the $PEDOT : PSS$ coated $pristine - Si$, $porous - Si$, and $plasmonic - Si$ substrate respectively. These SEM images indicate that $PEDOT : PSS$ coating does not have any significant impacts on the morphology of the silicon substrates.

Figure 5.5 is a cartoon image showing the energy band diagram of the $plasmonic - Si$ based photodetector. Compared to the $pristine - Si$, $porous - Si$ based devices, it has the advantage of high surface-to-volume ratio which can provide additional enhancement of the light trapping inside the heterojunction. Furthermore, for $plasmonic - Si$ based photodetector device, the generated plasmonic hot electrons when Ag nanoparticles are illuminated can be injected into the conduction band of $n - Si$ by overcoming or tunneling through the Schottky barrier

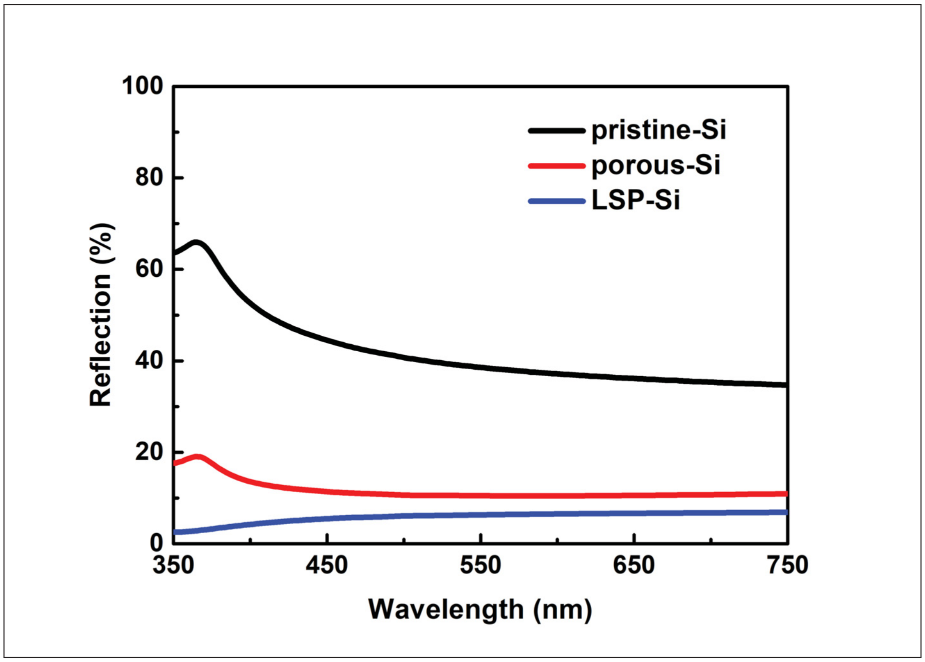

Figure 5.4 Light reflection for three different silicon substrates.

between $n-Si$ and Ag [Knight, Sobhani, Nordlander & Halas][Govorov, Zhang & Gun'ko]. The plasmonic holes in Ag nanoparticles would be incorporated in the hole-transport flow towards the contact. The current-voltage ($I-V$) characteristics in the dark and under 1.5G A.M. illumination are plotted in Figure 5.6(a-c), for $pristine-Si$-, $porous-Si$-, and $plasmonic-Si$-based photodetectors respectively. It can be noticed that the photocurrent enhancement from dark to light for $plasmonic-Si$ photodetector is a lot higher than comparing to the rest two where $pristine-Si$-based photodetector has the lowest enhancement. To be exact, the photocurrent enhancement from dark to light for $pristine-Si$, $porous-Si$ and $plasmonic-Si$ photodetectors are 14.2, 55.2 and 802 times respectively. The photocurrent enhancement data suggests that the characterization of the high surface-to-volume ratio of the $porous-Si$ provides a slightly improvement on the photocurrent generation. The most photocurrent enhancement is contributed by the Ag nanoparticles induced LSP effects.

The time-dependent photo-response for these photodetectors is investigated using a Newport solar simulator with a manually turned-on and -off for every 10 s as one period. Figure 5.7(a-f)

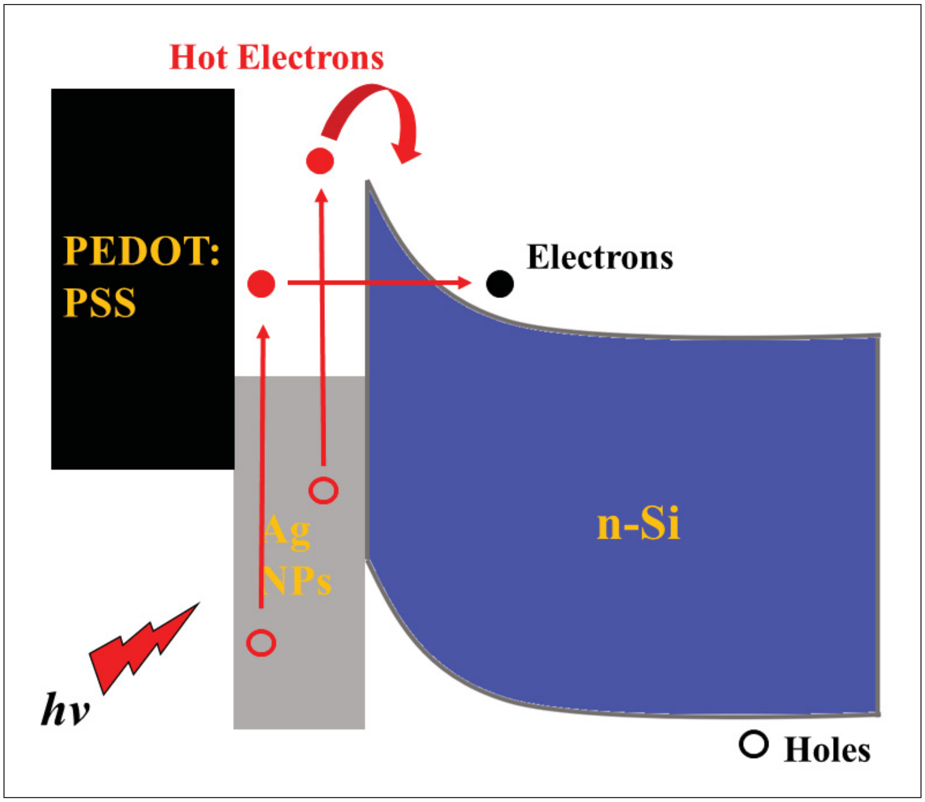

Figure 5.5 The energy band diagram of the photodetector with $plasmonic - Si$ substrate.

demonstrates the time response characteristics of the photodetector devices in the reversible ON/OFF states under an up to 4 V applied bias. All the observed ON/OFF switching behaviors for these $n - silicon$ based photodetector devices are performed over several cycles without losing photocurrent and photo-response speed suggesting the devices are reliable and robust. Zoomed in photo-response plots are shown in Figure 5.7(d-f) for clearer illustrations. The rise τ_r and decay τ_d for the $pristine - Si$, $porous - Si$ and $plasmonic - Si$ photodetectors are $\tau_r = 1000ms$ & $\tau_d = 749ms$, $\tau_r = 185ms$ & $\tau_d = 139ms$, and $\tau_r = 176ms$ & $\tau_d = 98ms$ respectively. In contrast, similar devices without any nanostructures on the $n - silicon$ substrate exhibits significantly larger time constants of $\tau_r = 1000ms \;\; \tau_d = 749ms$.

Figure 5.8 represents the spectral responsivity and the calculated detectivity for the photodetectors under 4 V. The spectral responsivity is the ratio between the incident light power and the

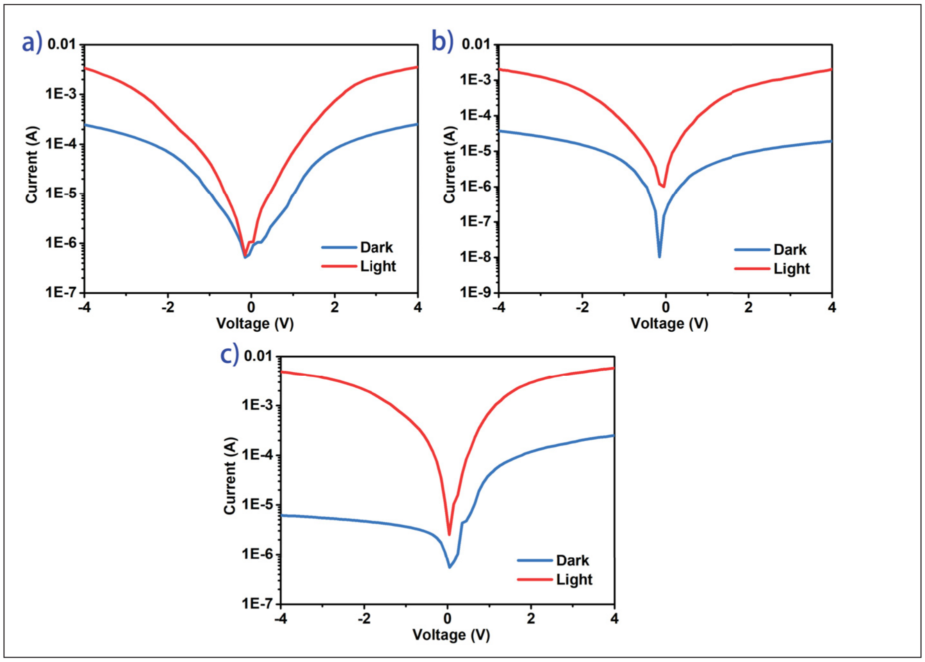

Figure 5.6 Current versus voltage characteristics at dark and under illumination (A.M. 1.5G illumination) for photodetectors with three types of $n - Si$ substrates. (a) $Pristine - Si$ based photodetector. (b) $Porous - Si$ based photodetector. (c) $Plasmonic - Si$ based photodetector.

photocurrent density as a function of the wavelength (380 – 700 nm). The responsivity for $pristine - Si$-, $porous - Si$-, and $plasmonic - Si$-based photodetectors are 11.1, 21.2, and 24.8 mAW^{-1} with their calculated detectivitis of $2.1E + 9$, $1.14E + 10$ and $1.6E + 10$ $cmHz^{1/2}W^{-1}$ respectively. We can notice that the detectivity of the $plasmonic - Si$-based device has an enhancement of one order of magnitude comparing to the pristine device. This enhancement is mainly introduced by higher surface-to-volume ratio, higher light absorptance, as well as higher electron-hole pairs because of the Ag nanoparticles. To provide a clear comparison, Table 5.1 summarized the characteristics of all three types of the photodetectors.

Figure 5.9 contains the statistic analysis of the $plasmonic - Si$-based photodetectors. Figure 5.9a shows the device stability for up to 60 days with the normalization of the photocurrent enhancement values on the y-axis. The $plasmonic - Si$-based photodetector still has more than 95% of its initial performance after 60 days when stored under an ambient environment. Totally

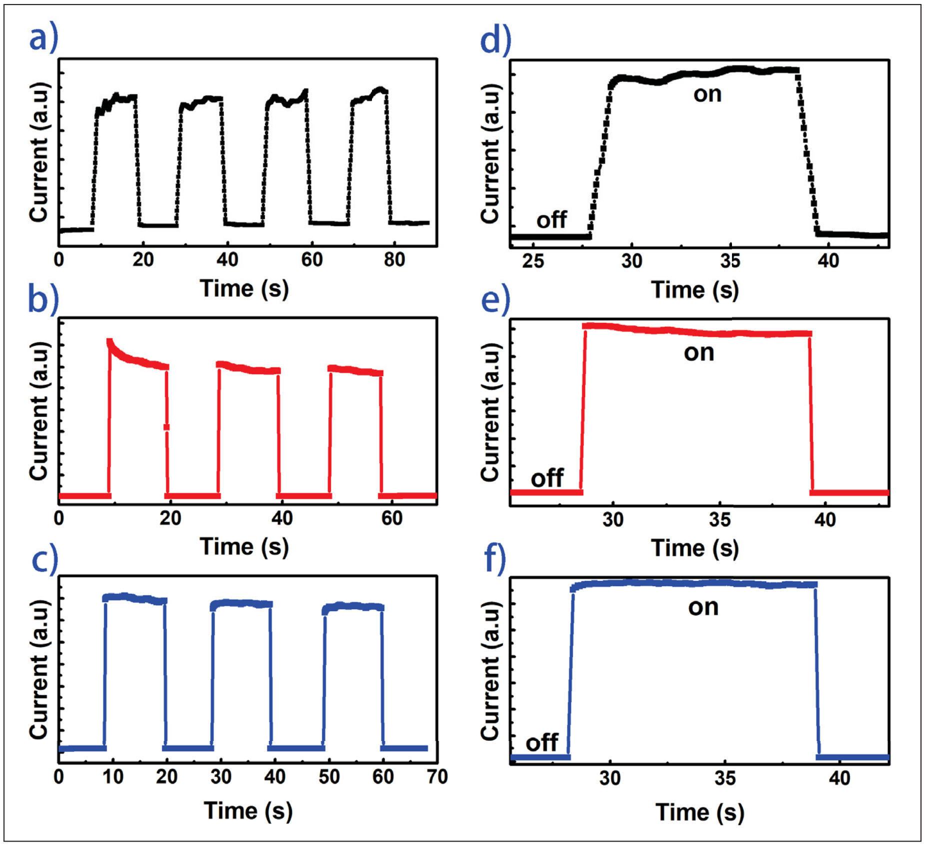

Figure 5.7 Transient photoresponse measurements for photodetectors with three different types of Si substrates (a) $Pristine-Si$. (b) $Porous-Si$, (c) $Plasmonic-Si$. (d), (e) and (f) are their zoomed-in plots for (a), (b) and (c) respectively

Table 5.1 A summary of the photodetectors with different types of silicon substrates

	$Pristine-Si$	$Porous-Si$	$Plasmonic-Si$
Photocurrent enhancement	14.2	55.2	**802**
Rise Time (ms)	1000	185	**176**
Decay Time (ms)	749	139	**98**
Responisity (mAW^{-1})	11.1	21.2	**24.8**
Detectivity ($cmHz^{1/2}W^{-1}$)	2.1E+9	1.14E+10	**1.6E+10**

ten(10) devices are characterized to generate the reproducibility data (Figure 5.9b). It shows that 90% of the devices have more than 800 times of photocurrent enhancement indicating they are highly reproducible.

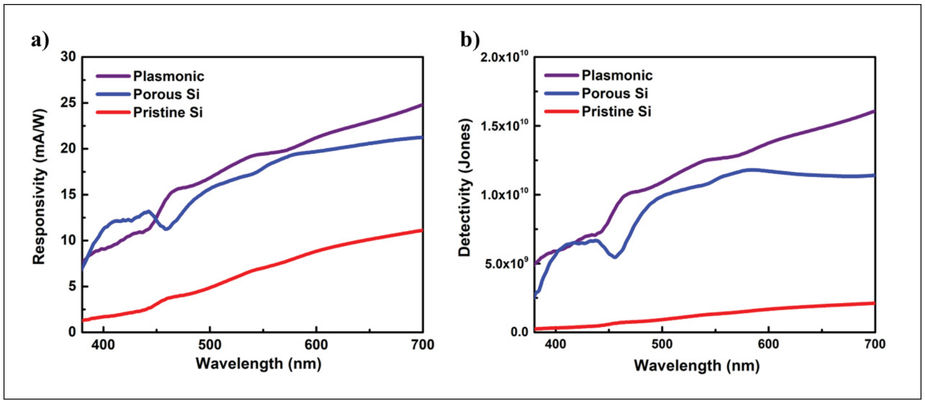

Figure 5.8 Spectral responsivity and detectivity for the $pristine-Si$-, $porous-Si$-, and $plasmonic-Si$-based photodetectors. (a) Responsivity in mA/W. (b) Detectivity in Jones.

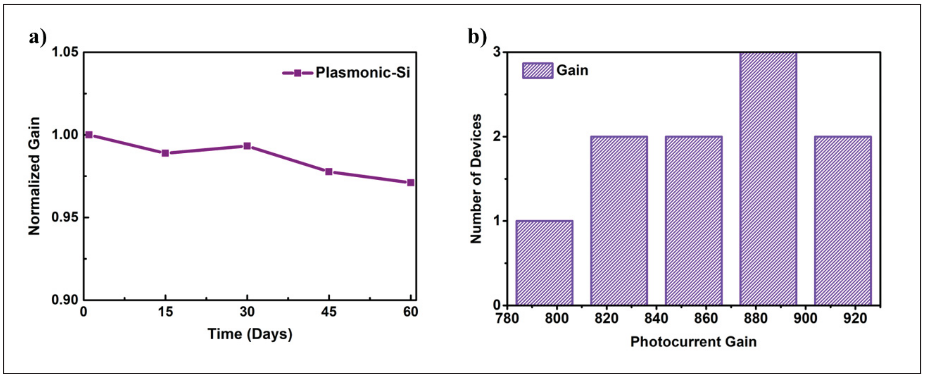

Figure 5.9 Statistic of the $Plasmonic-Si$-based photodetectors. (a) Normalized stability of the device by days. (b) Reproducibility based on 10 devices.

At last, a current-voltage characteristic for the plasmon-enhanced photodetector using a 2.5W flashlight at an indoor environment is shown in Figure 5.10 to demonstrate its practicability. The photocurrent enhancement is up to 85000x, which is superior compared to the AM 1.5G illumination, since the input power required for the flashlight is very low. Therefore, the photodetector has ability to detect low intensity light.

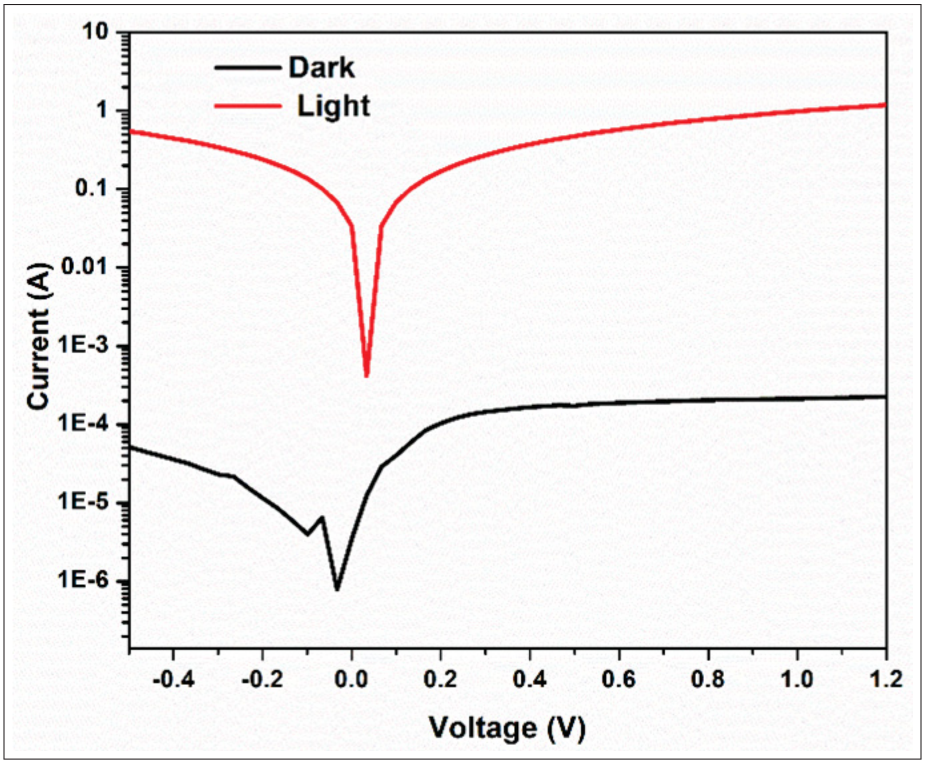

Figure 5.10 Current-voltage characteristic using a 2.5W flashlight for plasmon-enhanced photodetector.

5.4 Conclusion

In this chapter, we have demonstrated a fully inkjet printed high photocurrent enhancement photodetector (802 times on average) based on Ag nanoparticles induced surface plasmonic enhanced nanostructured $n - silicon$. This photodetector has the characteristics of a 176/98 ms rise/decay time under 1.5 sun, 24.8 mAW responsivity and $1.6E + 10$ $cmHz^{1/2}W^{-1}$ detectivity. Throughout the chapter, we have compared three types of $n - silicon$ substrates, such as $pristine - Si$, $porous - Si$, and $plasmonic - Si$ on both material and device performance perspectives. Firstly, with the silicon material analysis and device performance characterization, we have demonstrated Ag nanoparticles induced surface plasma together with the nanostructured silicon structure could dramatically improve the performance of the photodetectors. Secondly, we have also presented the possibility of incorporating inkjet printing into the silicon-based photodetector fabrication with good a device performance. Therefore, we believe our research could make a significant contribution to the further development of photodetector from both device structure and fabrication technique perspectives.

CHAPTER 6

CONCLUSION AND FUTURE RESEARCH PROSPECTS

6.1 Conclusion

In this thesis, various fabrication and characterization of the optoelectronic devices are demonstrated, including triple-cation perovskite-based LED, color-tunable polymer-based LED, and fully ink-jet printed photodetectors.

Compared to conventional inorganic material fabrication techniques, solution processes such as spin-coating could significantly reduce the fabrication cost. However, due to the similar solubility of the organic materials in the common organic solvent, spin-coating is not optimal in fabricating multi-layered architecture. To overcome this difficulty, electrospraying is implemented instead. It has the advantages of being material cost effective, narrow size distribution, and easy setup. Throughout the entire project of the color-tunable polymer-based PLEDs, we have found out the throughput consistency is hard to maintain for the electrospraying. Finally, we discover the ink-jet printing technique could be a solution containing both of their advantages, such as material cost-effective, precise control, and the possibility for multi-layered architecture fabrication.

Even with these advantages, the performance is still limited of novel solution-processable material-based devices, such as conjugate polymers and perovskite materials, compared to their inorganic counterparts. The limiting performance includes low stability, low brightness, and low efficiency for manufacturing products. In the solution-based fabrication process, the solvent used to mix the active material is critical. The properties such as dielectric constant, boiling point, and molecular weight affect the polymer molecular morphology during spin-coating, Taylor Cone formation during electrospraying, and droplets formation and deposition during ink-jet printing.

From the material and device perspectives, triple-cation perovskite, conjugate polymers, and n-type Si are used to fabricate NIR LEDs, color-tunable LEDs, and photodetectors respectively.

Organo-inorganic halide perovskite materials have many promising properties including high quantum yield, high charge carrier mobility, and tunable bandgap. However, the stability of the perovskite materials-based device remains as a great challenge. Among different types of perovskite materials, triple-cation perovskite is discovered to be the best candidate for overcoming stability difficulties due to its low sensitivity to processing conditions. After the successful demonstration of the triple-cation perovskite-based LED, we have implemented the perovskite grain tailoring technique which brings a 90% increment on the devices' EQE performance. Conjugate polymers are another promising material for LED fabrication because of their flexibility, solution possibility, and large-area scalability [Dai *et al.*][Wei *et al.* (a)]. We have implemented the electrospraying technique into the PLED fabrication process and successfully tuned the emission wavelength by controlling the deposition time of the electrosprayed polymer materials. Finally, we have fabricated photodetectors based on n-type Si using ink-jet printing. The photodetectors are divided into three patches, such as pristine Si, $porousSi$, and silver nano-particles embedded Si.

6.2 Future Research Prospects

As described in this thesis, a lot of work has been done in LED and photodetector fabrication using perovskite, conjugate polymers, and n-type Si with different fabrication techniques such as spin-coating, electrospraying, and ink-jet printing. However, many improvements can be implemented based on the results shown in this thesis. Some of the future research prospects are listed as follows (by type of the project):

6.2.1 Triple-cation based perovskite LED

- Develop a new recipe of the triple-cation perovskite for different emission wavelengths by varying the halide material composition, such as Cl, Br, and I.

- Modify the device architecture by using different ETL, HTL, and electrode materials achieving more efficient charge transportation and radiative recombination.
- Apply different perovskite post-treatment techniques, such as annealing, laser sintering, and UV exposure, and study their influences on the perovskite crystallinity and grain size distribution which could affect the device performance

6.2.2 Polymer-based LED via electrospraying

- Build an electrospraying setup that can precise monitoring some of the parameters and discover their connection to the electrospraying outcomes. The parameters can be humidity, ambient temperature, and chamber pressure.
- Develop a computer simulation tied closely to the electrospraying which could lead to better control of the consistency of the device performance.
- Implement another blue light-emitting polymer, forming a RGB color mixture system, to achieve while light emission.

6.2.3 Fully ink-jet printed optoelectronic devices

- Use ink-jet printing technique to fabricate polymer blend LED. When fabricating PLED using a polymer blend, phase separation is critical to the LED's performance. Because large phase is preferred for LED, we could achieve controlled large phase separation by printing one polymer right next to another. The LEDs containing controlled large-phase domains could have a great increase in their performance.
- Print polymer-based optoelectronic devices on a flexible substrate, such as polyimide (PI), polyethylene naphthalate (PEN), and polyethylene terephthalate (PET) using Au or Ag as electrode materials.

6.2.4 Academic Achievements

During this doctoral thesis, published journal articles with peer reviews are shown as follows:

1. X. Guo, J. Benavides-Guerrero, D. Banerjee, F. Roy-Moisan, and S. G. Cloutier, "Hybrid Color-Tunable Polymer Light-Emitting Diodes Using Electrospraying," ACS Omega 4(21), 19287–19292 (2019).

2. X. Guo, I. M. Asuo, I. M. Asuo, A. Pignolet, R. Nechache, and S. G. Cloutier, "Ambient fabrication of efficient triple cation perovskite-based near-infrared light-emitting diodes," Opt. Mater. Express 12(1), 153–165 (2022).

3. Guo, X. et al. Plasmon-enhanced photodetectors fabricated using digital inkjet-printing on chemically nanopatterned silicon wafers. AIP Adv. 13, 055309 (2023)

4. D. Banerjee, X. Guo, and S. G. Cloutier, "Plasmon-Enhanced Silicon Nanowire Array-Based Hybrid Heterojunction Solar Cells," Sol. RRL 2(7), 1800007 (2018).

5. D. Banerjee, J. A. Benavides, X. Guo, and S. G. Cloutier, "Tailored Interfaces of the Bulk Silicon Nanowire/TiO2 Heterojunction Promoting Enhanced Photovoltaic Performances," ACS Omega 3(5), 5064–5070 (2018).

6. D. Banerjee, X. Guo, J. Benavides, B. Rameau, and S. G. Cloutier, "Designing green self-healing anticorrosion conductive smart coating for metal protection," Smart Mater. Struct. 29(10), 105027 (2020).

7. J. A. Benavides-Guerrero, L. F. Gerlein, C. Trudeau, D. Banerjee, X. Guo, and S. G. Cloutier, "Synthesis of vacancy-rich titania particles suitable for the additive manufacturing of ceramics," Sci. Rep. 12(1), 15441 (2022).

APPENDIX I

SUPPORTING INFORMATION

Ambient Fabrication of Efficient Triple Cation Perovskite-Based Near-Infrared Light-Emitting Diodes

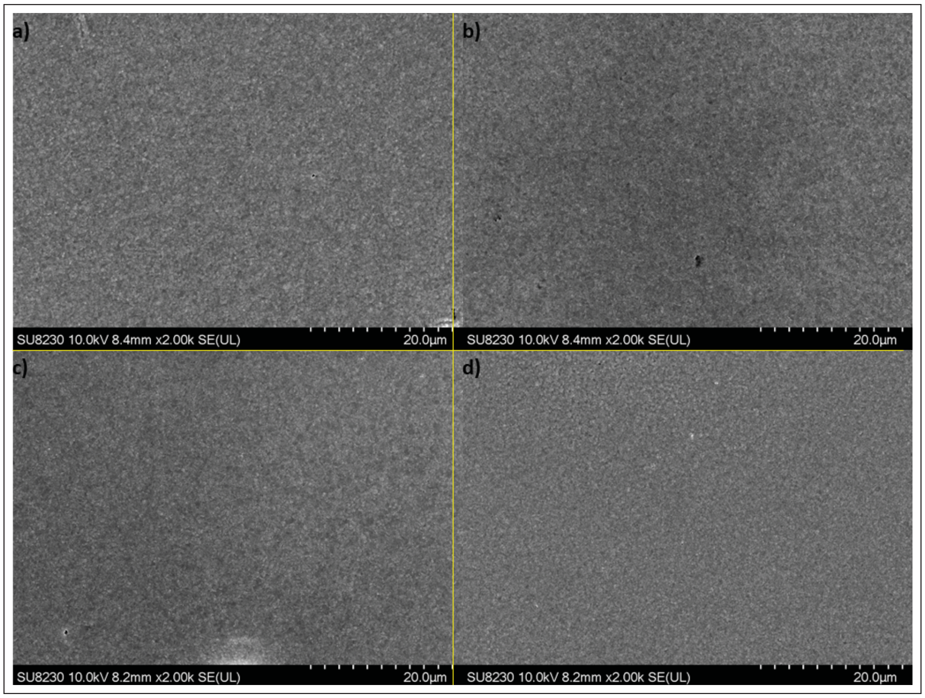

Figure-A -1 SEM images of the perovskite film with the scale bar of 20 µm.

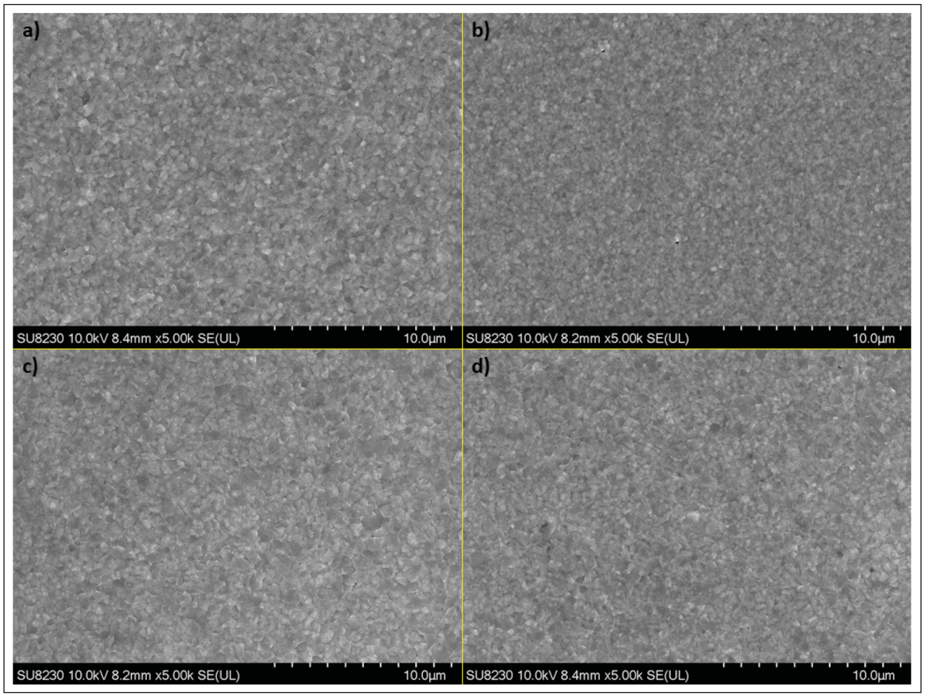

Figure-A -2 SEM images of the perovskite film with the scale bar of 10 µm.

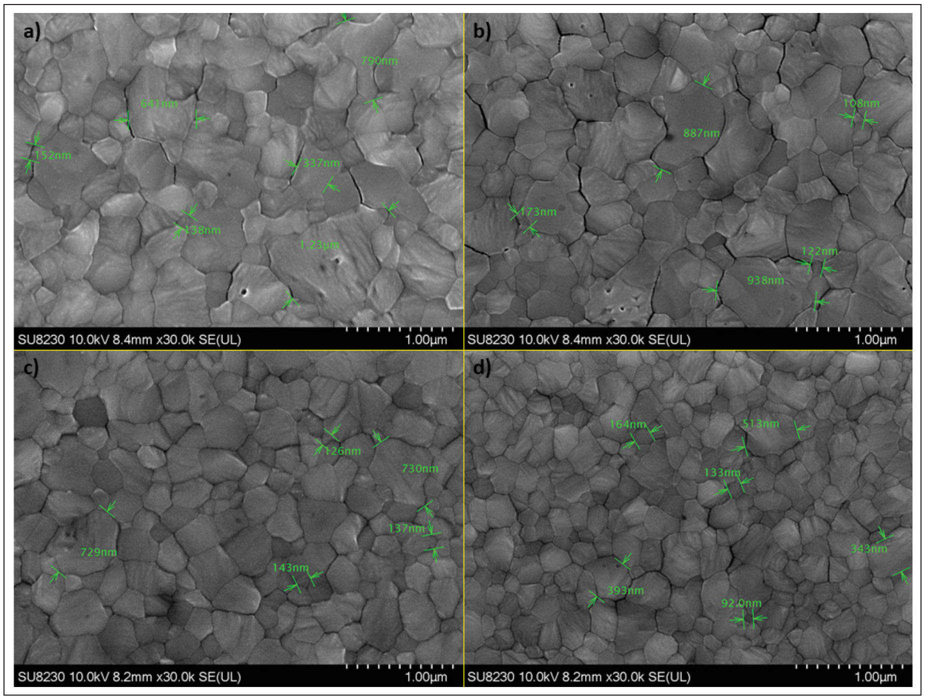

Figure-A -3 SEM images of the perovskite film with the scale bar of 1 µm with some measured size grains. For average size data collection, the ImageJ is used to measure the grain size based on the SEM images with a scale bar of 1 µm.

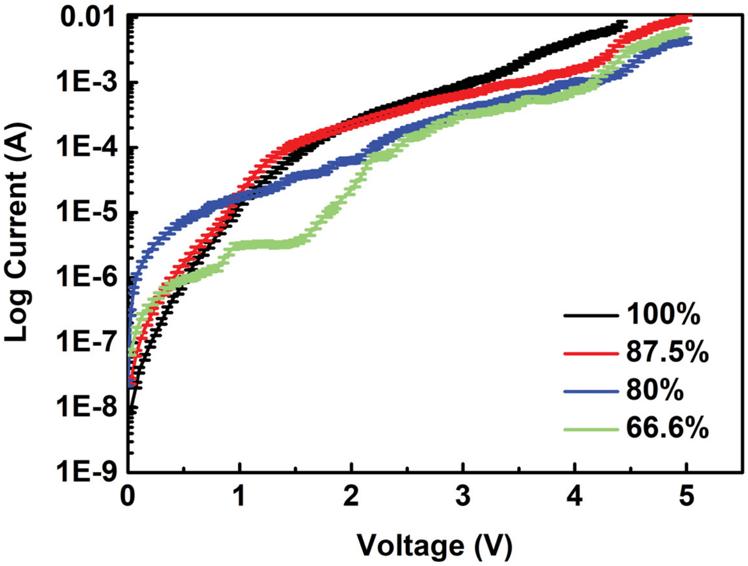

Figure-A -4 Semi-log of the IV curve for the perovskite LEDs. Sample 100% and 87.5% show very similar behavior in semi-log plot. However, sample 80% exhibits larger leakage current (about 1 order of magnitude) than previous mentioned two samples at low voltage.

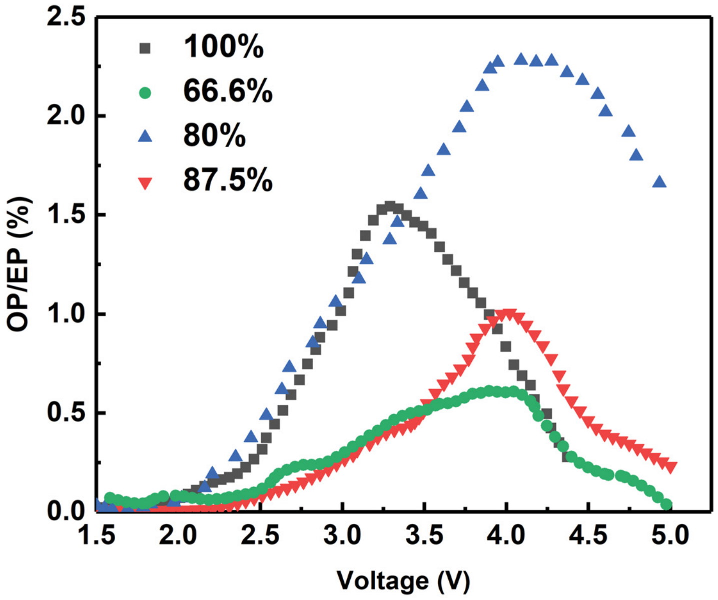

Figure-A -5 Power conversion efficiency as a function of applied voltage.

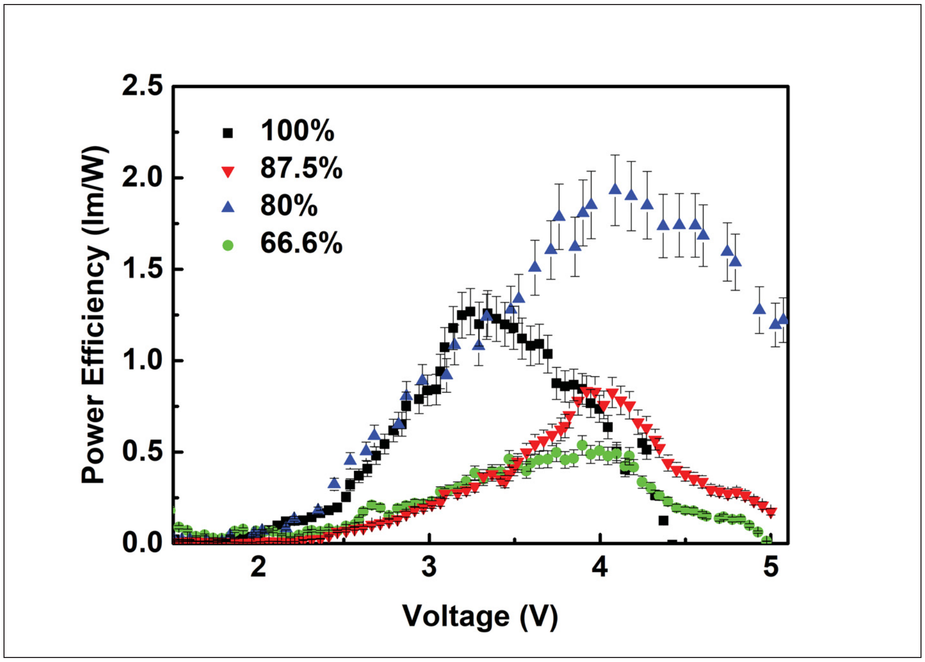

Figure-A -6 Power efficiency v.s. voltage characteristics of the perovskite LEDs. LED with 80% precursor concentration has the highest power efficiency of 1.93 lm/W with 10% error bar.

BIBLIOGRAPHY

2.2. Hybrid orbitals | Organic Chemistry 1: An open textbook. Retrieved on 2021-05-17 from: https://courses.lumenlearning.com/suny-potsdam-organicchemistry/chapter/2-2-hybrid-orbitals/.

2.4: 2.4 Conjugated Pi Bond Systems. Retrieved on 2022-10-23 from: https://chem.libretexts.org/Courses/Sacramento_City_College/SCC%3A_Chem_420_-_Organic_Chemistry_I/Text/02%3A_Structure_and_Properties_of_Organic_Molecules/2.04%3A_2.4_Conjugated_Pi_Bond_Systems.

BraggsLaw. Retrieved on 2020-10-10 from: https://serc.carleton.edu/research_education/geochemsheets/BraggsLaw.html.

Ceradrop - Inkjet Technology, Aerosol Jet, Digital Printing, Printed Electronics, Smart 3D, 3D, Piezoelectric inkjet printer. Retrieved on 2020-10-09 from: http://www.ceradrop.com/en/products/x-serie/.

[Page Version ID: 9921513]. *Exciton*. Wikipedia, den frie encyklopædi. Retrieved on 2022-10-23 from: https://da.wikipedia.org/w/index.php?title=Exciton&oldid=9921513.

F8BT | 210347-52-7. Retrieved on 2020-10-03 from: https://www.ossila.com/products/f8bt.

Google Code Archive - Long-term storage for Google Code Project Hosting. Retrieved on 2018-05-15 from: https://code.google.com/archive/p/jtchem/downloads.

Lighting Market Size, Share & Trends | Industry Report [2020-2027]. Retrieved on 2020-11-05 from: https://www.fortunebusinessinsights.com/industry-reports/lighting-market-101542.

Luminosity functions. Retrieved on 2020-10-03 from: http://www.cvrl.org/lumindex.htm.

MEH-PPV Polymer for Device Fabrication | 138184-36-8. Retrieved on 2020-10-06 from: https://www.ossila.com/products/meh-ppv.

Metal-Semiconductor Ohmic and Schottky Contacts. Retrieved on 2022-10-23 from: https://cleanroom.byu.edu/ohmic-schottky.

The Nobel Prize in Chemistry 2000. Retrieved on 2022-10-23 from: https://www.nobelprize.org/prizes/chemistry/2000/popular-information/.

Perovskite Mineral Data. Retrieved on 2021-05-18 from: http://webmineral.com/data/Perovskite.shtml#.YKNi92gzY2w.

PFO Polymer F8 for Organic Electronics | 19456-48-5 | Ossila. Retrieved on 2020-10-03 from: https://www.ossila.com/products/pfo-f8-19456-48-5?variant=19689534881888.

[Page Version ID: 977985794]. *Polyfluorene*. Wikipedia. Retrieved on 2020-10-03 from: https://en.wikipedia.org/w/index.php?title=Polyfluorene&oldid=977985794.

[Page Version ID: 949473935]. *Responsivity*. Wikipedia. Retrieved on 2020-10-13 from: https://en.wikipedia.org/w/index.php?title=Responsivity&oldid=949473935.

[Page Version ID: 980433171]. *Scanning electron microscope*. Wikipedia. Retrieved on 2020-10-10 from: https://en.wikipedia.org/w/index.php?title=Scanning_electron_microscope&oldid=980433171.

[Page Version ID: 1046030182]. *Strouhal number*. Wikipedia. Retrieved on 2021-10-03 from: https://en.wikipedia.org/w/index.php?title=Strouhal_number&oldid=1046030182.

Tetrahydrofuran Solvent Properties. Retrieved on 2022-10-25 from: https://macro.lsu.edu/howto/solvents/THF.htm.

TFB Polymer for OLEDs & Devices | 220797-16-0. Retrieved on 2020-10-03 from: https://www.ossila.com/products/tfb.

What is Benzene? Retrieved on 2022-10-23 from: https://regenesis.com/en/glossary/benzene/.

Wiley-VCH - Inkjet Printing in Industry. Retrieved on 2022-10-24 from: https://www.wiley-vch.de/de?option=com_eshop&view=product&isbn=9783527347803&title=Inkjet%20Printing%20in%20Industry.

X-ray Powder Diffraction (XRD). Retrieved on 2020-10-10 from: https://serc.carleton.edu/research_education/geochemsheets/techniques/XRD.html.

Rockett, A. (Ed.). Organic Semiconductors. *The Materials Science of Semiconductors* (pp. 395–453). Springer US. doi: 10.1007/978-0-387-68650-9_9.

Adjokatse, S., Fang, H.-H. & Loi, M. A. Broadly tunable metal halide perovskites for solid-state light-emission applications. 20(8), 413–424. doi: 10.1016/j.mattod.2017.03.021.

Ahn, N., Kwak, K., Jang, M. S., Yoon, H., Lee, B. Y., Lee, J.-K., Pikhitsa, P. V., Byun, J. & Choi, M. Trapped charge-driven degradation of perovskite solar cells. 7(1), 13422. doi: 10.1038/ncomms13422. Number: 1 Publisher: Nature Publishing Group.

Al-Milaji, K. N. & Zhao, H. New Perspective of Mitigating the Coffee-Ring Effect: Interfacial Assembly. 123(19), 12029–12041. doi: 10.1021/acs.jpcc.9b00797. Publisher: American

Chemical Society.

Alamri, A. M., Leung, S., Vaseem, M., Shamim, A. & He, J.-H. Fully Inkjet-Printed Photodetector Using a Graphene/Perovskite/Graphene Heterostructure. 66(6), 2657–2661. doi: 10.1109/TED.2019.2911715. Conference Name: IEEE Transactions on Electron Devices.

Alamán, J., Alicante, R., Peña, J. I. & Sánchez-Somolinos, C. Inkjet Printing of Functional Materials for Optical and Photonic Applications. 9(11). doi: 10.3390/ma9110910.

Aleeva, Y. & Pignataro, B. Recent advances in upscalable wet methods and ink formulations for printed electronics. 2(32), 6436–6453. doi: 10.1039/C4TC00618F. Publisher: The Royal Society of Chemistry.

Amat, A., Mosconi, E., Ronca, E., Quarti, C., Umari, P., Nazeeruddin, M. K., Grätzel, M. & De Angelis, F. Cation-Induced Band-Gap Tuning in Organohalide Perovskites: Interplay of Spin–Orbit Coupling and Octahedra Tilting. 14(6), 3608–3616. doi: 10.1021/nl5012992. Publisher: American Chemical Society.

An, D., Zou, J., Wu, H., Peng, J., Yang, W. & Cao, Y. White emission polymer light-emitting devices with efficient electron injection from alcohol/water-soluble polymer/Al bilayer cathode. 10(2), 299–304. doi: 10.1016/j.orgel.2008.11.016.

and & and, a. Analysis of the ohmic contacts of Ti/Al/Ni/Au to AlGaN/GaN HEMTs by the multi-step annealing process. 33(6), 064005. doi: 10.1088/1674-4926/33/6/064005.

Anjusree, G. S., Deepak, T. G., Nair, S. V. & Nair, A. S. Facile fabrication of TiO2 nanoparticle–TiO2 nanofiber composites by co-electrospinning–electrospraying for dye-sensitized solar cells. 24(6), 762–769. doi: 10.1016/j.jechem.2015.11.001.

Arias, A. C., MacKenzie, J. D., McCulloch, I., Rivnay, J. & Salleo, A. Materials and Applications for Large Area Electronics: Solution-Based Approaches. 110(1), 3–24. doi: 10.1021/cr900150b. Publisher: American Chemical Society.

Aristidou, N., Sanchez-Molina, I., Chotchuangchutchaval, T., Brown, M., Martinez, L., Rath, T. & Haque, S. A. The Role of Oxygen in the Degradation of Methylammonium Lead Trihalide Perovskite Photoactive Layers. 54(28), 8208–8212. doi: https://doi.org/10.1002/anie.201503153. _eprint: https://onlinelibrary.wiley.com/doi/pdf/10.1002/anie.201503153.

Arora, N., Dar, M. I., Abdi-Jalebi, M., Giordano, F., Pellet, N., Jacopin, G., Friend, R. H., Zakeeruddin, S. M. & Grätzel, M. Intrinsic and Extrinsic Stability of Formamidinium Lead Bromide Perovskite Solar Cells Yielding High Photovoltage. 16(11), 7155–7162. doi: 10.1021/acs.nanolett.6b03455. Publisher: American Chemical Society.

Arora, N., Dar, M. I., Hinderhofer, A., Pellet, N., Schreiber, F., Zakeeruddin, S. M. & Grätzel, M. Perovskite solar cells with CuSCN hole extraction layers yield stabilized efficiencies greater than 20%. doi: 10.1126/science.aam5655. Publisher: American Association for the Advancement of Science Section: Report.

Ashraf, S., Mattsson, C. G., Fondell, M., Lindblad, A. & Thungström, G. Surface modification of SU-8 for metal/SU-8 adhesion using RF plasma treatment for application in thermopile detectors. 2(8), 086501. doi: 10.1088/2053-1591/2/8/086501. Publisher: IOP Publishing.

Asuo, I. M., Gedamu, D., Doumon, N. Y., Ka, I., Pignolet, A., Cloutier, S. G. & Nechache, R. Ambient condition-processing strategy for improved air-stability and efficiency in mixed-cation perovskite solar cells. 1(6), 1866–1876. doi: 10.1039/D0MA00528B. Publisher: RSC.

Asuo, I. M., Gedamu, D., Ka, I., Gerlein, L. F., Fortier, F.-X., Pignolet, A., Cloutier, S. G. & Nechache, R. High-performance pseudo-halide perovskite nanowire networks for stable and fast-response photodetector. 51, 324–332. doi: 10.1016/j.nanoen.2018.06.057.

Azam, M., Yue, S., Xu, R., Liu, K., Ren, K., Sun, Y., Liu, J., Wang, Z., Qu, S., Lei, Y. & Wang, Z. Highly efficient solar cells based on Cl incorporated tri-cation perovskite materials. 6(28), 13725–13734. doi: 10.1039/C8TA03953D. Publisher: The Royal Society of Chemistry.

Azzellino, G., Grimoldi, A., Binda, M., Caironi, M., Natali, D. & Sampietro, M. Fully Inkjet-Printed Organic Photodetectors with High Quantum Yield. 25(47), 6829–6833. doi: 10.1002/adma.201303473. _eprint: https://onlinelibrary.wiley.com/doi/pdf/10.1002/adma.201303473.

B. Mitzi, D. Templating and structural engineering in organic–inorganic perovskites. 0(1), 1–12. doi: 10.1039/B007070J. Publisher: Royal Society of Chemistry.

Baleja, R., Šumpich, J., Bos, P., Helštýnová, B., Sokanský, K. & Novšk, T. Comparison of LED properties, compact fluorescent bulbs and bulbs in residential areas. *2015 16th International Scientific Conference on Electric Power Engineering (EPE)*, pp. 566–571. doi: 10.1109/EPE.2015.7161181.

Banerjee, D., Asuo, I. M., Pignolet, A., Nechache, R. & Cloutier, S. G. High performance photodetectors using porous silicon-TiO2 heterostructure. 2(3), 035021. doi: 10.1088/2631-8695/abb06d. Publisher: IOP Publishing.

Banerjee, D., Trudeau, C., Gerlein, L. F. & Cloutier, S. G. Phonon processes in vertically aligned silicon nanowire arrays produced by low-cost all-solution galvanic displacement method. 108(11), 113109. doi: 10.1063/1.4944334. Publisher: American Institute of Physics.

Bao, G., Li, D., Sun, X., Jiang, M., Li, Z., Song, H., Jiang, H., Chen, Y., Miao, G. & Zhang, Z. Enhanced spectral response of an AlGaN-based solar-blind ultraviolet photodetector with Al nanoparticles. 22(20), 24286–24293. doi: 10.1364/OE.22.024286. Publisher: Optical Society of America.

Bella, F., Renzi, P., Cavallo, C. & Gerbaldi, C. Caesium for Perovskite Solar Cells: An Overview. 24(47), 12183–12205. doi: 10.1002/chem.201801096.

Berhe, T. A., Su, W.-N., Chen, C.-H., Pan, C.-J., Cheng, J.-H., Chen, H.-M., Tsai, M.-C., Chen, L.-Y., Dubale, A. A. & Hwang, B.-J. Organometal halide perovskite solar cells: degradation and stability. 9(2), 323–356. doi: 10.1039/C5EE02733K. Publisher: The Royal Society of Chemistry.

Bernanose, A. Electroluminescence of organic compounds. 6, S54–S55. doi: 10.1088/0508-3443/6/S4/319. Publisher: IOP Publishing.

Bernanose, A., Comte, M. & Vouaux, P. Sur un nouveau mode d'émission lumineuse chez certains composés organiques. 50, 64–68. doi: 10.1051/jcp/1953500064. Publisher: EDP Sciences.

Besteiro, L. V., Kong, X.-T., Wang, Z., Hartland, G. & Govorov, A. O. Understanding Hot-Electron Generation and Plasmon Relaxation in Metal Nanocrystals: Quantum and Classical Mechanisms. 4(11), 2759–2781. doi: 10.1021/acsphotonics.7b00751. Publisher: American Chemical Society.

Bethe, H. A. *Theory of the Boundary Layer of Crystal Rectifiers*. Radiation Laboratory, Massachusetts Institute of Technology.

Blom, P. W. M., de Jong, M. J. M. & Vleggaar, J. J. M. Electron and hole transport in poly(p-phenylene vinylene) devices. 68(23), 3308–3310. doi: 10.1063/1.116583. Publisher: American Institute of Physics.

Blom, P. W. M., Mihailetchi, V. D., Koster, L. J. A. & Markov, D. E. Device Physics of Polymer:Fullerene Bulk Heterojunction Solar Cells. 19(12), 1551–1566. doi: https://doi.org/10.1002/adma.200601093. _eprint: https://onlinelibrary.wiley.com/doi/pdf/10.1002/adma.200601093.

Boda, S. K., Li, X. & Xie, J. Electrospraying an enabling technology for pharmaceutical and biomedical applications: A review. 125, 164–181. doi: 10.1016/j.jaerosci.2018.04.002.

Bodas, D. & Khan-Malek, C. Formation of more stable hydrophilic surfaces of PDMS by plasma and chemical treatments. 83(4), 1277–1279. doi: 10.1016/j.mee.2006.01.195.

Bodnár, E., Grifoll, J. & Rosell-Llompart, J. Polymer solution electrospraying: A tool for engineering particles and films with controlled morphology. 125, 93–118. doi: 10.1016/j.jaerosci.2018.04.012.

Boyd, C. C., Cheacharoen, R., Leijtens, T. & McGehee, M. D. Understanding Degradation Mechanisms and Improving Stability of Perovskite Photovoltaics. 119(5), 3418–3451. doi: 10.1021/acs.chemrev.8b00336. Publisher: American Chemical Society.

Bradley, D. Electroluminescent polymers: materials, physics and device engineering. 1(6), 789–797. doi: 10.1016/S1359-0286(96)80103-3.

Braun, D. Semiconducting polymer LEDs. 5(6), 32–39. doi: 10.1016/S1369-7021(02)00637-5.

Breternitz, J., Tovar, M. & Schorr, S. Twinning in MAPbI 3 at room temperature uncovered through Laue neutron diffraction. 10(1), 16613. doi: 10.1038/s41598-020-73487-1. Number: 1 Publisher: Nature Publishing Group.

Brédas, J. L., Heeger, A. J. & Wudl, F. Towards organic polymers with very small intrinsic band gaps. I. Electronic structure of polyisothianaphthene and derivatives. 85(8), 4673–4678. doi: 10.1063/1.451741. Publisher: American Institute of Physics.

Burroughes, J. H., Bradley, D. D. C., Brown, A. R., Marks, R. N., Mackay, K., Friend, R. H., Burns, P. L. & Holmes, A. B. Light-emitting diodes based on conjugated polymers. 347(6293), 539–541. doi: 10.1038/347539a0.

Cacialli, F., Friend, R. H., Bouché, C.-M., Le Barny, P., Facoetti, H., Soyer, F. & Robin, P. Naphthalimide side-chain polymers for organic light-emitting diodes: Band-offset engineering and role of polymer thickness. 83(4), 2343–2356. doi: 10.1063/1.366977. Publisher: American Institute of Physics.

Campbell, A. J., Bradley, D. D. C. & Antoniadis, H. Quantifying the efficiency of electrodes for positive carrier injection into poly(9,9-dioctylfluorene) and representative copolymers. 89(6), 3343–3351. doi: 10.1063/1.1334925. Publisher: American Institute of Physics.

Cao, W., Li, J., Chen, H. & Xue, J. Transparent electrodes for organic optoelectronic devices: a review. 4(1), 040990. doi: 10.1117/1.JPE.4.040990. Publisher: SPIE.

Chandrakalavathi, T., Peta, K. R. & Jeyalakshmi, R. Enhanced UV photoresponse with Au nanoparticles incorporated rGO/Si heterostructure. 5(2), 025011. doi: 10.1088/2053-1591/aaa9ac. Publisher: IOP Publishing.

Charles, T. Printed electronics prototyping of flexible optoelectronic methylammonium trihalide perovskite based devices [phdthesis]. Ecole de Technologie Superieure.

Chen, J., Zhou, S., Jin, S., Li, H. & Zhai, T. Crystal organometal halide perovskites with promising optoelectronic applications. 4(1), 11–27. doi: 10.1039/C5TC03417E. Publisher: The Royal Society of Chemistry.

Chen, J., Zhou, S., Jin, S., Li, H. & Zhai, T. Crystal organometal halide perovskites with promising optoelectronic applications. 4(1), 11–27. doi: 10.1039/C5TC03417E. Publisher: Royal Society of Chemistry.

Chen, W., Wu, Y., Yue, Y., Liu, J., Zhang, W., Yang, X., Chen, H., Bi, E., Ashraful, I., Grätzel, M. & Han, L. Efficient and stable large-area perovskite solar cells with inorganic charge extraction layers. 350(6263), 944–948. doi: 10.1126/science.aad1015. Publisher: American Association for the Advancement of Science.

Chen, Y., Zhang, L., Zhang, Y., Gao, H. & Yan, H. Large-area perovskite solar cells – a review of recent progress and issues. 8(19), 10489–10508. doi: 10.1039/C8RA00384J. Publisher: The Royal Society of Chemistry.

Chen, Z., Turedi, B., Alsalloum, A. Y., Yang, C., Zheng, X., Gereige, I., AlSaggaf, A., Mohammed, O. F. & Bakr, O. M. Single-Crystal MAPbI3 Perovskite Solar Cells Exceeding 21% Power Conversion Efficiency. 4(6), 1258–1259. doi: 10.1021/acsenergylett.9b00847. Publisher: American Chemical Society.

Chiu, F.-C. (2014). A Review on Conduction Mechanisms in Dielectric Films. *Advances in Materials Science and Engineering*, 2014, 1-18.

Cho, H., Jeong, S.-H., Park, M.-H., Kim, Y.-H., Wolf, C., Lee, C.-L., Heo, J. H., Sadhanala, A., Myoung, N., Yoo, S., Im, S. H., Friend, R. H. & Lee, T.-W. Overcoming the electroluminescence efficiency limitations of perovskite light-emitting diodes. 350(6265), 1222. doi: 10.1126/science.aad1818.

Cho, H., Kim, J. S., Wolf, C., Kim, Y.-H., Yun, H. J., Jeong, S.-H., Sadhanala, A., Venugopalan, V., Choi, J. W., Lee, C.-L., Friend, R. H. & Lee, T.-W. High-Efficiency Polycrystalline Perovskite Light-Emitting Diodes Based on Mixed Cations. 12(3), 2883–2892. doi: 10.1021/acsnano.8b00409. Publisher: American Chemical Society.

Choi, W.-J., Kwak, D.-J., Park, C.-S. & Sung, Y.-M. Characterization of Transparent Conductive ITO, ITiO, and FTO Films for Application in Photoelectrochemical Cells. 12(4), 3394–3397. doi: 10.1166/jnn.2012.5571.

Christians, J. A., Miranda Herrera, P. A. & Kamat, P. V. Transformation of the Excited State and Photovoltaic Efficiency of CH3NH3PbI3 Perovskite upon Controlled Exposure to Humidified Air. 137(4), 1530–1538. doi: 10.1021/ja511132a. Publisher: American Chemical Society.

Conings, B., Drijkoningen, J., Gauquelin, N., Babayigit, A., D'Haen, J., D'Olieslaeger, L., Ethirajan, A., Verbeeck, J., Manca, J., Mosconi, E., Angelis, F. D. & Boyen, H.-G. Intrinsic Thermal Instability of Methylammonium Lead Trihalide Perovskite. 5(15), 1500477. doi: https://doi.org/10.1002/aenm.201500477. _eprint: https://onlinelibrary.wiley.com/doi/pdf/10.1002/aenm.201500477.

Cook, J. H., Al-Attar, H. A. & Monkman, A. P. Effect of PEDOT–PSS resistivity and work function on PLED performance. 15(1), 245–250. doi: 10.1016/j.orgel.2013.11.029.

Cui, X. & Boland, T. Human microvasculature fabrication using thermal inkjet printing technology. 30(31), 6221–6227. doi: 10.1016/j.biomaterials.2009.07.056.

Cummins, G. & Desmulliez, M. P. Inkjet printing of conductive materials: a review. 38(4), 193–213. doi: 10.1108/03056121211280413. Publisher: Emerald Group Publishing Limited.

Dai, X., Zhang, Z., Jin, Y., Niu, Y., Cao, H., Liang, X., Chen, L., Wang, J. & Peng, X. Solution-processed, high-performance light-emitting diodes based on quantum dots. 515(7525), 96–99. doi: 10.1038/nature13829.

Daly, R., Harrington, T. S., Martin, G. D. & Hutchings, I. M. Inkjet printing for pharmaceutics – A review of research and manufacturing. 494(2), 554–567. doi: 10.1016/j.ijpharm.2015.03.017.

de Gans, B.-J., Duineveld, P. C. & Schubert, U. S. Inkjet Printing of Polymers: State of the Art and Future Developments. 16(3), 203–213. doi: 10.1002/adma.200300385. _eprint: https://onlinelibrary.wiley.com/doi/pdf/10.1002/adma.200300385.

Deng, W., Zhang, X., Huang, L., Xu, X., Wang, L., Wang, J., Shang, Q., Lee, S.-T. & Jie, J. Aligned Single-Crystalline Perovskite Microwire Arrays for High-Performance Flexible Image Sensors with Long-Term Stability. 28(11), 2201–2208. doi: 10.1002/adma.201505126. _eprint: https://onlinelibrary.wiley.com/doi/pdf/10.1002/adma.201505126.

Deng, X. Y., Lau, W. M., Wong, K. Y., Low, K. H., Chow, H. F. & Cao, Y. High efficiency low operating voltage polymer light-emitting diodes with aluminum cathode. 84(18), 3522–3524. doi: 10.1063/1.1739510.

Derby, B. Inkjet Printing of Functional and Structural Materials: Fluid Property Requirements, Feature Stability, and Resolution. 40(1), 395–414. doi: 10.1146/annurev-matsci-070909-104502. _eprint: https://doi.org/10.1146/annurev-matsci-070909-104502.

Doe, J. (1999a). ACRONYM: Class name. Institution.

Doe, J. (1999b). ACRONYM: Class name [Class notes]. Retrieved from: http://www.google.ca.

Doe, J. (1999c). *The title of the thesis*. (Master's thesis, School, Address).

Doe, J. (1999d). *The title of the thesis*. (Master's thesis, School, Address). Retrieved from: Name of the database. (ID number).

Doe, J. (1999e). *The title of the thesis*. (Master's thesis, School, Address). Retrieved from: http://www.google.ca.

Doe, J. (1999f). Web page title [Format]. Retrieved from: http://www.google.ca.

Doe, J. (1999g). Dataset title [Online dataset]. Retrieved from: http://www.google.ca.

Doe, J. (1999h). Dataset title [Online dataset]. Retrieved from: http://www.google.ca.

Doe, J. [Nickname]. (1999i, October, 2). Web page title [Format]. Retrieved from: http://www.google.ca.

Doe, J. [Nickname]. (1999j, October, 2). Web page title [Format]. Retrieved from: http://www.google.ca.

Doe, J. [Nickname]. (1999k, October, 2). Video title [Youtube Video]. Retrieved from: http://www.google.ca.

Doe, J. [Nickname]. (1999l, October, 2). Video title [Youtube Video]. Retrieved from: http://www.google.ca.

Doe, J. (1999m). Web page title [Format]. Retrieved from: http://www.google.ca.

Doe, J. (1999n). *Patent type n°42*. Location: organization.

Doe, J. (1999o). *Patent type n°42*. Location: organization.

Doe, J. (1999p). *The title of the thesis*. (Ph.D. thesis, School, Address).

Doe, J. [Unpublished raw data]. (1999q) [Short description of the contents].

Doe, J. (1999r). Software name (Version 1.0) [Software]. Location: Publisher.

Doe, J. (1999s). *The title of the report* (Report n°42). Location: Publisher.

Doe, J. (1999t). *Document title*. Unpublished document, Institution, Location.

Doe, J. (1999u). *Document title*. Manuscript submitted for publication.

Doe, J. (1999v). *Document title*. Retrieved from: http://www.google.ca.

Doe, J., Doe, J. & Doe, J. (1999a). Title of the article. *Name of the journal*, 4(2), 220-242.

Doe, J., Doe, J. & Doe, J. (1999b). Title of the article. *Name of the journal*. In press.

Doe, J., Doe, J. & Doe, J. (1999c). *Title of the book* (ed. 3). Location: Publisher.

Doe, J., Doe, J. & Doe, J. (1999d). *Title of the book* [Version]. doi: 123-456-789.

Doe, J., Doe, J. & Doe, J. (Eds.). (1999e). *Title of the book* (ed. 3). Location: Publisher.

Doe, J., Doe, J. & Doe, J. (1999f). *Title of the book* [Version]. Retrieved from: http: //www.google.com.

Doe, J., Doe, J. & Doe, J. (1999g). Title of the entry. In *Title of the encyclopedia* (ed. 3, vol. 4, pp. 220-242). Location: Publisher.

Doe, J., Doe, J. & Doe, J. (1999h). In Doe, J., Doe, J. & Doe, J. (Eds.), *Title of the book* (ed. 3, vol. 4, ch. 7, pp. 220-242). Location: Publisher.

Doe, J., Doe, J. & Doe, J. (1999i). Title of the chapter. In Doe, J., Doe, J. & Doe, J. (Eds.), *Title of the book* (ed. 3, vol. 4, pp. 220-242). Location: Publisher.

Doe, J., Doe, J. & Doe, J. (1999j). Title of the article. In Doe, J., Doe, J. & Doe, J. (Eds.), *Title of the conference proceedings* (ed. 3, vol. 4, pp. 220-242). Location: Publisher.

Doe, J., Doe, J. & Doe, J. (1999k, October). *Title of the article*. Communication presented in Title of the conference proceedings, Location (pp. 220-242).

Doe, J., Doe, J. & Doe, J. (1999l). Title of the article. *Title of the conference proceedings*, 4(2), 220-242.

Doe, J., Doe, J. & Doe, J. (1999m, October). Title of the article. *Title of the magasine*, 4(2), 220-242.

Doe, J., Doe, J. & Doe, J. (1999n, October). Title of the article. *Title of the magasine*, pp. 220.

Dong, C., Wang, Z.-K. & Liao, L.-S. Progress of Triple Cation Organometal Halide Perovskite Solar Cells. 8(4), 1900804. doi: https://doi.org/10.1002/ente.201900804. _eprint: https://onlinelibrary.wiley.com/doi/pdf/10.1002/ente.201900804.

Dong, H., Zhang, C., Liu, X., Yao, J. & Zhao, Y. S. Materials chemistry and engineering in metal halide perovskite lasers. 49(3), 951–982. doi: 10.1039/C9CS00598F. Publisher: The Royal Society of Chemistry.

Dong, H., Carr, W. W. & Morris, J. F. Visualization of drop-on-demand inkjet: Drop formation and deposition. 77(8), 085101. doi: 10.1063/1.2234853. Publisher: American Institute of Physics.

Dou, L., Yang, Y. M., You, J., Hong, Z., Chang, W.-H., Li, G. & Yang, Y. Solution-processed hybrid perovskite photodetectors with high detectivity. 5(1), 5404. doi: 10.1038/ncomms6404. Number: 1 Publisher: Nature Publishing Group.

Downs, C. & Vandervelde, T. E. Progress in Infrared Photodetectors Since 2000. 13(4), 5054–5098. doi: 10.3390/s130405054. Number: 4 Publisher: Multidisciplinary Digital Publishing Institute.

Efimenko, K., Wallace, W. E. & Genzer, J. Surface Modification of Sylgard-184 Poly(dimethyl siloxane) Networks by Ultraviolet and Ultraviolet/Ozone Treatment. 254(2), 306–315. doi: 10.1006/jcis.2002.8594.

El-Mahalawy, A. M. & Wassel, A. R. Enhancement of organic/inorganic hybrid photodetector based on pentacene/n-Si by surface plasmonic effect of gold and silver nanoparticles: A comparative study. 131, 106395. doi: 10.1016/j.optlastec.2020.106395.

El-Mellouhi, F., Bentria, E. T., Rashkeev, S. N., Kais, S. & Alharbi, F. H. Enhancing Intrinsic Stability of Hybrid Perovskite Solar Cell by Strong, yet Balanced, Electronic Coupling. 6(1), 30305. doi: 10.1038/srep30305. Number: 1 Publisher: Nature Publishing Group.

Eperon, G. E., Stranks, S. D., Menelaou, C., Johnston, M. B., Herz, L. M. & Snaith, H. J. Formamidinium lead trihalide: a broadly tunable perovskite for efficient planar heterojunction solar cells. 7(3), 982–988. doi: 10.1039/C3EE43822H. Publisher: The Royal Society of Chemistry.

Ercan, E., Tsai, P.-C., Chen, J.-Y., Lam, J.-Y., Hsu, L.-C., Chueh, C.-C. & Chen, W.-C. Stretchable and Ambient Stable Perovskite/Polymer Luminous Hybrid Nanofibers of Multicolor Fiber Mats and Their White LED Applications. 11(26), 23605–23615. doi: 10.1021/acsami.9b05527. Publisher: American Chemical Society.

Fang, T., Zhang, F., Yuan, S., Zeng, H. & Song, J. Recent advances and prospects toward blue perovskite materials and light-emitting diodes. 1(2), 211–233. doi: https://doi.org/10.1002/inf2.12019. _eprint: https://onlinelibrary.wiley.com/doi/pdf/10.1002/inf2.12019.

Fashandi, H. & Karimi, M. Pore formation in polystyrene fiber by superimposing temperature and relative humidity of electrospinning atmosphere. 53(25), 5832–5849. doi: 10.1016/j.polymer.2012.10.003.

Friedel, B., Keivanidis, P. E., Brenner, T. J. K., Abrusci, A., McNeill, C. R., Friend, R. H. & Greenham, N. C. Effects of Layer Thickness and Annealing of PEDOT:PSS Layers in Organic Photodetectors. 42(17), 6741–6747. doi: 10.1021/ma901182u. Publisher: American Chemical Society.

Frolova, L. A., Davlethanov, A. I., Dremova, N. N., Zhidkov, I., Akbulatov, A. F., Kurmaev, E. Z., Aldoshin, S. M., Stevenson, K. J. & Troshin, P. A. Efficient and Stable MAPbI3-Based Perovskite Solar Cells Using Polyvinylcarbazole Passivation. 11(16), 6772–6778. doi: 10.1021/acs.jpclett.0c01776. Publisher: American Chemical Society.

Fromm, J. E. Numerical Calculation of the Fluid Dynamics of Drop-on-Demand Jets. 28(3), 322–333. doi: 10.1147/rd.283.0322. Conference Name: IBM Journal of Research and Development.

Frost, J. M., Butler, K. T., Brivio, F., Hendon, C. H., van Schilfgaarde, M. & Walsh, A. Atomistic Origins of High-Performance in Hybrid Halide Perovskite Solar Cells. 14(5), 2584–2590. doi: 10.1021/nl500390f. Publisher: American Chemical Society.

Gardos, M. N. Tribo-oxidative degradation of polished polycrystalline diamond films in 0.2Torr partial pressure of oxygen. In Dowson, D., Priest, M., Taylor, C. M., Ehret, P., Childs, T. H. C., Dalmaz, G., Lubrecht, A. A., Berthier, Y., Flamand, L. & Georges, J. M. (Eds.), *Tribology Series* (vol. 38, pp. 549–558). Elsevier. doi: 10.1016/S0167-8922(00)80159-5.

Geffroy, B., le Roy, P. & Prat, C. Organic light-emitting diode (OLED) technology: materials, devices and display technologies. 55(6), 572–582. doi: 10.1002/pi.1974. _eprint: https://onlinelibrary.wiley.com/doi/pdf/10.1002/pi.1974.

Ghayempour, S. & Mortazavi, S. M. Fabrication of micro–nanocapsules by a new electrospraying method using coaxial jets and examination of effective parameters on their production. 4(71), 717–727. doi: 10.1016/j.elstat.2013.04.001.

Giebeler, C., Antoniadis, H., Bradley, D. D. C. & Shirota, Y. Influence of the hole transport layer on the performance of organic light-emitting diodes. 85(1), 608–615. doi: 10.1063/1.369413. Publisher: American Institute of Physics.

Girtan, M. & Negulescu, B. A review on oxide/metal/oxide thin films on flexible substrates as electrodes for organic and perovskite solar cells. 13, 100122. doi: 10.1016/j.omx.2021.100122.

Gohain, N. Studies on the structure and function of phenazine modifying enzymes PhzM and PhzS involved in the biosynthesis of pyocyanin. doi: 10.17877/DE290R-8364. Accepted: 2009-06-29T09:48:19Z.

Goldschmidt, V. M. Die Gesetze der Krystallochemie. 14, 477–485. doi: 10.1007/BF01507527.

Goldstein, J., Newbury, D. E., Joy, D. C., Lyman, C. E., Echlin, P., Lifshin, E., Sawyer, L. & Michael, J. R. *Scanning Electron Microscopy and X-Ray Microanalysis: Third Edition* (ed. 3). Springer US. doi: 10.1007/978-1-4615-0215-9.

Goswami, L., Aggarwal, N., Krishna, S., Singh, M., Vashishtha, P., Singh, S. P., Husale, S., Pandey, R. & Gupta, G. Au-Nanoplasmonics-Mediated Surface Plasmon-Enhanced GaN Nanostructured UV Photodetectors. 5(24), 14535–14542. doi: 10.1021/acsomega.0c01239. Publisher: American Chemical Society.

Govorov, A. O., Zhang, H. & Gun'ko, Y. K. Theory of Photoinjection of Hot Plasmonic Carriers from Metal Nanostructures into Semiconductors and Surface Molecules. 117(32), 16616–16631. doi: 10.1021/jp405430m. Publisher: American Chemical Society.

Granqvist, C. G. Transparent conductive electrodes for electrochromic devices: A review. 57(1), 19–24. doi: 10.1007/BF00331211.

Green, M. A., Dunlop, E. D., Hohl-Ebinger, J., Yoshita, M., Kopidakis, N. & Ho-Baillie, A. W. Y. Solar cell efficiency tables (Version 55). 28(1), 3–15. doi: 10.1002/pip.3228. _eprint: https://onlinelibrary.wiley.com/doi/pdf/10.1002/pip.3228.

Grüner, J., Remmers, M. & Neher, D. Direct determination of the emission zone in a polymer light-emitting diode. 9(12), 964–968. doi: 10.1002/adma.19970091207. _eprint: https://onlinelibrary.wiley.com/doi/pdf/10.1002/adma.19970091207.

Guo, X. e. a. Hybrid Color-Tunable Polymer Light-Emitting Diodes Using Electrospraying. 4(21), 19287–19292. doi: 10.1021/acsomega.9b02666. Publisher: American Chemical Society.

Guo, X., Asuo, I. M., Asuo, I. M., Pignolet, A., Nechache, R. & Cloutier, S. G. Ambient fabrication of efficient triple cation perovskite-based near-infrared light-emitting diodes. 12(1), 153–165. doi: 10.1364/OME.445150. Publisher: Optica Publishing Group.

Guo, Z., Jiang, D., Zhao, M., Guo, F., Pei, J., Liu, R., Sun, L., Hu, N. & Zhang, G. Surface plasmon enhanced the responsivity of the ZnO/Pt nanoparticles/ZnO sandwich structured photodetector via optimizing the thickness of the top ZnO layer. 124, 24–27. doi: 10.1016/j.sse.2016.07.026.

Gupta, A. A., Arunachalam, S., Cloutier, S. G. & Izquierdo, R. Fully Aerosol-Jet Printed, High-Performance Nanoporous ZnO Ultraviolet Photodetectors. 5(10), 3923–3929. doi: 10.1021/acsphotonics.8b00829. Publisher: American Chemical Society.

Gustafsson, G., Cao, Y., Treacy, G. M., Klavetter, F., Colaneri, N. & Heeger, A. J. Flexible light-emitting diodes made from soluble conducting polymers. 357(6378), 477–479. doi: 10.1038/357477a0.

Hameed, B. S., Bhatt, C. S., Nagaraj, B. & Suresh, A. K. Chapter 19 - Chromatography as an Efficient Technique for the Separation of Diversified Nanoparticles. In Hussain, C. M. (Ed.), *Nanomaterials in Chromatography* (pp. 503–518). Elsevier. doi: 10.1016/B978-0-12-812792-6.00019-4.

Han, Y., Meyer, S., Dkhissi, Y., Weber, K., Pringle, J. M., Bach, U., Spiccia, L. & Cheng, Y.-B. Degradation observations of encapsulated planar CH3NH3PbI3 perovskite solar cells at high temperatures and humidity. 3(15), 8139–8147. doi: 10.1039/C5TA00358J. Publisher: The Royal Society of Chemistry.

Hasan, K. u., Sandberg, M. O., Nur, O. & Willander, M. ZnO/Polyfluorene Hybrid LED on an Efficient Hole-Transport Layer of Graphene Oxide and Transparent Graphene Electrode. 2(4), 326–330. doi: 10.1002/adom.201300412.

Hewidy, D., Gadallah, A. S. & Fattah, G. A. Electroluminescence enhancement of glass/ITO/PEDOT:PSS/MEH-PPV/PEDOT:PSS/Al OLED by thermal annealing. 1130, 327–332. doi: 10.1016/j.molstruc.2016.10.040.

Ho, P. K. H., Kim, J.-S., Burroughes, J. H., Becker, H., Li, S. F. Y., Brown, T. M., Cacialli, F. & Friend, R. H. Molecular-scale interface engineering for polymer light-emitting diodes. 404(6777), 481–484. doi: 10.1038/35006610.

Hofmann, A. I., Cloutet, E. & Hadziioannou, G. Materials for Transparent Electrodes: From Metal Oxides to Organic Alternatives. 4(10), 1700412. doi: 10.1002/aelm.201700412.

Hogan, C. J., Yun, K. M., Chen, D.-R., Lenggoro, I. W., Biswas, P. & Okuyama, K. Controlled size polymer particle production via electrohydrodynamic atomization. 311(1), 67–76. doi: 10.1016/j.colsurfa.2007.05.072.

Hon, K. K. B., Li, L. & Hutchings, I. M. Direct writing technology-Advances and developments. *CIRP Annals - Manufacturing Technology|CIRP Ann Manuf Technol*, pp. 601–620. doi: 10.1016/j.cirp.2008.09.006.

Hong, S. C., Lee, G., Ha, K., Yoon, J., Ahn, N., Cho, W., Park, M. & Choi, M. Precise Morphology Control and Continuous Fabrication of Perovskite Solar Cells Using Droplet-

Controllable Electrospray Coating System. 9(9), 7879–7884. doi: 10.1021/acsami.6b15095.

Hoye, R. L. Z., Chua, M. R., Musselman, K. P., Li, G., Lai, M.-L., Tan, Z.-K., Greenham, N. C., MacManus-Driscoll, J. L., Friend, R. H. & Credgington, D. Enhanced Performance in Fluorene-Free Organometal Halide Perovskite Light-Emitting Diodes using Tunable, Low Electron Affinity Oxide Electron Injectors. 27(8), 1414–1419. doi: 10.1002/adma.201405044.

Hu, L., Li, J., Liu, J., Grüner, G. & Marks, T. Flexible organic light-emitting diodes with transparent carbon nanotube electrodes: problems and solutions. 21(15), 155202. doi: 10.1088/0957-4484/21/15/155202. Publisher: IOP Publishing.

Huang, Y., Yu, Q., Wang, J., Wang, J., Yu, C., Abdalla, J. T., Zeng, Z., Jiao, S., Wang, D. & Gao, S. Plasmon-Enhanced Self-Powered UV Photodetectors Assembled by Incorporating Ag@SiO2 Core–Shell Nanoparticles into TiO2 Nanocube Photoanodes. 6(1), 438–446. doi: 10.1021/acssuschemeng.7b02697. Publisher: American Chemical Society.

Hung, L. S. & Chen, C. H. Recent progress of molecular organic electroluminescent materials and devices. 39(5), 143–222. doi: 10.1016/S0927-796X(02)00093-1.

Hwang, J., Amy, F. & Kahn, A. Spectroscopic study on sputtered PEDOT·PSS: Role of surface PSS layer. 7(5), 387–396. doi: 10.1016/j.orgel.2006.04.005.

Hwang, W., Xin, G., Cho, M., Cho, S. M. & Chae, H. Electrospray deposition of polymer thin films for organic light-emitting diodes. 7(1), 52. doi: 10.1186/1556-276X-7-52.

Jafari-Nodoushan, M., Barzin, J. & Mobedi, H. Size and morphology controlling of PLGA microparticles produced by electro hydrodynamic atomization. 26(5), 502–513. doi: 10.1002/pat.3480. _eprint: https://onlinelibrary.wiley.com/doi/pdf/10.1002/pat.3480.

Jaworek, A. & Sobczyk, A. Electrospraying route to nanotechnology: An overview. 66(3), 197–219. doi: 10.1016/j.elstat.2007.10.001.

Jaworek, A., Krupa, A., Lackowski, M., Sobczyk, A. T., Czech, T., Ramakrishna, S., Sundarrajan, S. & Pliszka, D. Nanocomposite fabric formation by electrospinning and electrospraying technologies. 67(2), 435–438. doi: 10.1016/j.elstat.2008.12.019.

Jeon, N. J., Noh, J. H., Kim, Y. C., Yang, W. S., Ryu, S. & Seok, S. I. Solvent engineering for high-performance inorganic–organic hybrid perovskite solar cells. 13(9), 897–903. doi: 10.1038/nmat4014. Number: 9 Publisher: Nature Publishing Group.

Jeong, J., Kim, J. & Kim, H. Ag grid/ITO hybrid transparent electrodes prepared by inkjet printing. doi: 10.1016/J.SOLMAT.2011.02.016.

Jia, R., Lin, G., Zhao, D., Zhang, Q., Lin, X., Gao, N. & Liu, D. Sandwich-structured Cu2O photodetectors enhanced by localized surface plasmon resonances. 332, 340–345. doi: 10.1016/j.apsusc.2015.01.194.

Jiang, H. & Tan, H. One Dimensional Model for Droplet Ejection Process in Inkjet Devices. 3(2), 28. doi: 10.3390/fluids3020028. Number: 2 Publisher: Multidisciplinary Digital Publishing Institute.

Jiazhen, S., Minxuan, K. & Yanlin, S. Control and Application of "Coffee Ring" Effect in Inkjet Printing. 27(8), 979. doi: 10.7536/PC150230.

Jing, H., Peng, R., Ma, R.-M., He, J., Zhou, Y., Yang, Z., Li, C.-Y., Liu, Y., Guo, X., Zhu, Y., Wang, D., Su, J., Sun, C., Bao, W. & Wang, M. Flexible Ultrathin Single-Crystalline Perovskite Photodetector. doi: 10.1021/acs.nanolett.0c02468. Publisher: American Chemical Society.

Johnsson, M. & Lemmens, P. Crystallography and Chemistry of Perovskites. In *Handbook of Magnetism and Advanced Magnetic Materials*. American Cancer Society. doi: 10.1002/9780470022184.hmm411.

Ju, J., Yamagata, Y. & Higuchi, T. Thin-film fabrication method for organic light-emitting diodes using electrospray deposition. 21(43), 4343–4347. doi: 10.1002/adma.200900444.

Ju, Y., Song, J., Geng, Z., Zhang, H., Wang, W., Xie, L., Yao, W. & Li, Z. A microfluidics cytometer for mice anemia detection. 12(21), 4355–4362. doi: 10.1039/C2LC40332C. Publisher: The Royal Society of Chemistry.

Jung, M., Shin, T. J., Seo, J., Kim, G. & Seok, S. I. Structural features and their functions in surfactant-armoured methylammonium lead iodide perovskites for highly efficient and stable solar cells. 11(8), 2188–2197. doi: 10.1039/C8EE00995C. Publisher: The Royal Society of Chemistry.

Ka, I., Gerlein, L. F., Nechache, R. & Cloutier, S. G. High-performance nanotube-enhanced perovskite photodetectors. 7(1), 45543. doi: 10.1038/srep45543. Number: 1 Publisher: Nature Publishing Group.

Kabra, D., Lu, L. P., Song, M. H., Snaith, H. J. & Friend, R. H. Efficient Single-Layer Polymer Light-Emitting Diodes. 22(29), 3194–3198. doi: 10.1002/adma.201000317.

Kaddoum, G., Tran, H., Kong, L. & Atallah, M. (2017). Design of Simultaneous Wireless Information and Power Transfer Scheme for Short Reference DCSK Communication Systems. *IEEE Transactions on Communications*, 65(1), 431-443. doi: 10.1109/TCOMM.2016.2619707.

Kamyshny, A. & Magdassi, S. Conductive Nanomaterials for Printed Electronics. 10(17), 3515–3535. doi: 10.1002/smll.201303000. _eprint: https://onlinelibrary.wiley.com/doi/pdf/10.1002/smll.201303000.

Kasparek, C. & Blom, P. W. M. Solution-processed multilayer polymer light-emitting diode without intermixing. 110(2), 023302. doi: 10.1063/1.4973989. Publisher: American Institute of Physics.

Kaur, G., Yadav, K. L. & Mitra, A. Localized surface plasmon induced enhancement of electron-hole generation with silver metal island at n-Al:ZnO/p-Cu2O heterojunction. 107(5), 053901. doi: 10.1063/1.4928373. Publisher: American Institute of Physics.

Kawasaki, H., Yao, T., Suganuma, T., Okumura, K., Iwaki, Y., Yonezawa, T., Kikuchi, T. & Arakawa, R. Platinum Nanoflowers on Scratched Silicon by Galvanic Displacement for an Effective SALDI Substrate. 16(35), 10832–10843. doi: 10.1002/chem.201001038. _eprint: https://chemistry-europe.onlinelibrary.wiley.com/doi/pdf/10.1002/chem.201001038.

Ke, L., Chellappan, V., Liu, B., Soh, Z. X., Soh, R. H. T. & Chua, S. J. Electrical and optical properties of an alcohol soluble aminoalkyl-substituted cationic conjugated polymer. 43(8), 2818–2824. doi: 10.1007/s10853-008-2511-7.

Kebarle, P. & Verkerk, U. H. On the Mechanism of Electrospray Ionization Mass Spectrometry (ESIMS). In *Electrospray and MALDI Mass Spectrometry* (pp. 1–48). John Wiley & Sons, Ltd. doi: 10.1002/9780470588901.ch1.

Keivanidis, P. E., Ho, P. K. H., Friend, R. H. & Greenham, N. C. The Dependence of Device Dark Current on the Active-Layer Morphology of Solution-Processed Organic Photodetectors. 20(22), 3895–3903. doi: 10.1002/adfm.201000967. _eprint: https://onlinelibrary.wiley.com/doi/pdf/10.1002/adfm.201000967.

Kelley, S. O., Mirkin, C. A., Walt, D. R., Ismagilov, R. F., Toner, M. & Sargent, E. H. Advancing the speed, sensitivity and accuracy of biomolecular detection using multi-length-scale engineering. 9(12), 969–980. doi: 10.1038/nnano.2014.261. Number: 12 Publisher: Nature Publishing Group.

Khalate, A. A., Bombois, X., Scorletti, G., Babuska, R., Koekebakker, S. & de Zeeuw, W. A Waveform Design Method for a Piezo Inkjet Printhead Based on Robust Feedforward Control. 21(6), 1365–1374. doi: 10.1109/JMEMS.2012.2205899. Conference Name: Journal of Microelectromechanical Systems.

Khan, H., Yerramilli, A. S., D'Oliveira, A., Alford, T. L., Boffito, D. C. & Patience, G. S. Experimental methods in chemical engineering: X-ray diffraction spectroscopy—XRD. 98(6), 1255–1266. doi: 10.1002/cjce.23747. _eprint:

https://onlinelibrary.wiley.com/doi/pdf/10.1002/cjce.23747.

Kim, H.-S., Dhage, S. R., Shim, D.-E. & Hahn, H. T. Intense pulsed light sintering of copper nanoink for printed electronics. 97(4). doi: 10.1007/s00339-009-5360-6.

Kim, H., Zhao, L., Price, J. S., Grede, A. J., Roh, K., Brigeman, A. N., Lopez, M., Rand, B. P. & Giebink, N. C. Hybrid perovskite light emitting diodes under intense electrical excitation. 9(1), 4893. doi: 10.1038/s41467-018-07383-8. Number: 1 Publisher: Nature Publishing Group.

Kim, H.-S., Im, S. H. & Park, N.-G. Organolead Halide Perovskite: New Horizons in Solar Cell Research. 118(11), 5615–5625. doi: 10.1021/jp409025w. Publisher: American Chemical Society.

Kim, H. P., Kim, J., Kim, B. S., Kim, H.-M., Kim, J., Yusoff, A. R. b. M., Jang, J. & Nazeeruddin, M. K. High-Efficiency, Blue, Green, and Near-Infrared Light-Emitting Diodes Based on Triple Cation Perovskite. 5(7), 1600920. doi: 10.1002/adom.201600920.

Kimukin, [Accepted: 2016-07-01T11:02:14Z]. High speed and high efficiency infrared photodetectors [Thesis]. Bilkent University. Retrieved on 2021-05-21 from: http://repository.bilkent.edu.tr/handle/11693/29617.

Knight, M. W., Sobhani, H., Nordlander, P. & Halas, N. J. Photodetection with Active Optical Antennas. 332(6030), 702–704. doi: 10.1126/science.1203056. Publisher: American Association for the Advancement of Science Section: Report.

Kojima, A., Teshima, K., Shirai, Y. & Miyasaka, T. Organometal Halide Perovskites as Visible-Light Sensitizers for Photovoltaic Cells. 131(17), 6050–6051. doi: 10.1021/ja809598r.

Konstantakou, M. & Stergiopoulos, T. A critical review on tin halide perovskite solar cells. 5(23), 11518–11549. doi: 10.1039/C7TA00929A. Publisher: The Royal Society of Chemistry.

Krebs, F. C., Fyenbo, J. & Jørgensen, M. Product integration of compact roll-to-roll processed polymer solar cell modules: methods and manufacture using flexographic printing, slot-die coating and rotary screen printing. 20(41), 8994–9001. doi: 10.1039/C0JM01178A. Publisher: The Royal Society of Chemistry.

Kremer, M. H. [Publisher: Oregon State University]. Electrospray Deposition of Discrete Nanoparticles: Studies on Pulsed-Field Electrospray and Analytical Applications.

Kumar, D. & Sharma, R. C. Advances in conductive polymers. 34(8), 1053–1060. doi: 10.1016/S0014-3057(97)00204-8.

Kumar, M., Bhatt, V., Abhyankar, A. C., Yun, J.-H. & Jeong, H.-J. Multifunctional dumbbell-shaped ZnO based temperature-dependent UV photodetection and selective H2 gas detection. 45(29), 15011–15025. doi: 10.1016/j.ijhydene.2020.03.215.

Kumawat, N. K., Gupta, D. & Kabra, D. Recent Advances in Metal Halide-Based Perovskite Light-Emitting Diodes. 5(10), 1734–1749. doi: https://doi.org/10.1002/ente.201700356. _eprint: https://onlinelibrary.wiley.com/doi/pdf/10.1002/ente.201700356.

Kwon, K.-S., Rahman, M. K., Phung, T. H., Hoath, S. D., Jeong, S. & Kim, J. S. Review of digital printing technologies for electronic materials. 5(4), 043003. doi: 10.1088/2058-8585/abc8ca. Publisher: IOP Publishing.

Köhler, A., dos Santos, D. A., Beljonne, D., Shuai, Z., Brédas, J.-L., Holmes, A. B., Kraus, A., Müllen, K. & Friend, R. H. Charge separation in localized and delocalized electronic states in polymeric semiconductors. 392(6679), 903–906. doi: 10.1038/31901. Number: 6679 Publisher: Nature Publishing Group.

Larson, R. G. Re-Shaping the Coffee Ring. 51(11), 2546–2548. doi: 10.1002/anie.201108008. _eprint: https://onlinelibrary.wiley.com/doi/pdf/10.1002/anie.201108008.

Le, Q. V., Jang, H. W. & Kim, S. Y. Recent Advances toward High-Efficiency Halide Perovskite Light-Emitting Diodes: Review and Perspective. 2(10), 1700419. doi: 10.1002/smtd.201700419. _eprint: https://onlinelibrary.wiley.com/doi/pdf/10.1002/smtd.201700419.

Le, Q. V., Shin, J. W., Jung, J.-H., Park, J., Ozturk, A. & Kim, S. Y. Control of the Crystal Growth Shape in CH3NH3PbBr3 Perovskite Materials. 17(11), 8169–8174. doi: 10.1166/jnn.2017.15113.

Lee, C., Li, Y., Lee, W., Lee, Y., Choi, J., Kim, T., Wang, C., Gomez, E. D., Woo, H. Y. & Kim, B. J. Correlation between Phase-Separated Domain Sizes of Active Layer and Photovoltaic Performances in All-Polymer Solar Cells. 49(14), 5051–5058. doi: 10.1021/acs.macromol.6b01069. Publisher: American Chemical Society.

Lee, J. Y., Choi, M. H., Moon, D. K. & Haw, J. R. Synthesis of fluorene- and anthracene-based -conjugated polymers and dependence of emission range and luminous efficiency on molecular weight. 16(3), 395–400. doi: 10.1016/j.jiec.2009.08.003.

Lee, J.-W., Seol, D.-J., Cho, A.-N. & Park, N.-G. High-efficiency perovskite solar cells based on the black polymorph of HC(NH2)2 PbI3. 26(29), 4991–4998. doi: 10.1002/adma.201401137.

Lee, J.-Y., Connor, S. T., Cui, Y. & Peumans, P. Solution-Processed Metal Nanowire Mesh Transparent Electrodes. 8(2), 689–692. doi: 10.1021/nl073296g. Publisher: American

Chemical Society.

Lee, S., Koo, H. & Cho, S. Mask-less patterning of organic light emitting diodes using electrospray and selective biasing on pixel electrodes. 106(17), 173303. doi: 10.1063/1.4919382.

Lenggoro,I. Wuled, O. K., Fernández de la Mora, J. & Tohge, N. PREPARATION OF ZnS NANOPARTICLES BY ELECTROSPRAY PYROLYSIS. 31(1), 121–136. doi: 10.1016/S0021-8502(99)00534-0.

Li, W., Wang, D., Zhang, Z., Chu, X., Fang, X., Wang, X., Fang, D., Lin, F., Wang, X. & Wei, Z. Enhancement of a Cu_2O/ZnO photodetector via surface plasmon resonance induced by Ag nanoparticles. 8(11), 3561–3567. doi: 10.1364/OME.8.003561. Publisher: Optical Society of America.

Li, Y. Self-doped n-type water/alcohol-soluble conjugated polymers ETL for high-performance polymer and perovskite solar cells. 59(11), 1430–1431. doi: 10.1007/s11426-016-0152-y.

Li, Z., Yang, M., Park, J.-S., Wei, S.-H., Berry, J. J. & Zhu, K. Stabilizing Perovskite Structures by Tuning Tolerance Factor: Formation of Formamidinium and Cesium Lead Iodide Solid-State Alloys. 28(1), 284–292. doi: 10.1021/acs.chemmater.5b04107. Publisher: American Chemical Society.

Li, Z.-J., Hofman, E., Li, J., Davis, A. H., Tung, C.-H., Wu, L.-Z. & Zheng, W. Photoelectrochemically Active and Environmentally Stable CsPbBr3/TiO2 Core/Shell Nanocrystals. 28(1), 1704288. doi: 10.1002/adfm.201704288. _eprint: https://onlinelibrary.wiley.com/doi/pdf/10.1002/adfm.201704288.

Liang, Z., Zeng, P., Liu, P., Zhao, C., Xie, W. & Mai, W. Interface Engineering To Boost Photoresponse Performance of Self-Powered, Broad-Bandwidth PEDOT:PSS/Si Heterojunction Photodetector. 8(29), 19158–19167. doi: 10.1021/acsami.6b06301. Publisher: American Chemical Society.

Lin, G., Zhang, Q., Lin, X., Zhao, D., Jia, R., Gao, N., Zuo, Z., Xu, X. & Liu, D. Enhanced photoluminescence of gallium phosphide by surface plasmon resonances of metallic nanoparticles. 5(60), 48275–48280. doi: 10.1039/C5RA07368E. Publisher: The Royal Society of Chemistry.

Liu, D., Yu, B.-B., Liao, M., Jin, Z., Zhou, L., Zhang, X., Wang, F., He, H., Gatti, T. & He, Z. Self-Powered and Broadband Lead-Free Inorganic Perovskite Photodetector with High Stability. 12(27), 30530–30537. doi: 10.1021/acsami.0c05636. Publisher: American Chemical Society.

Liu, D., Gangishetty, M. K. & Kelly, T. L. Effect of CH3NH3PbI3 thickness on device efficiency in planar heterojunction perovskite solar cells. 2(46), 19873–19881. doi: 10.1039/C4TA02637C.

Liu, K., Qu, S., Zhang, X., Tan, F. & Wang, Z. Improved photovoltaic performance of silicon nanowire/organic hybrid solar cells by incorporating silver nanoparticles. 8(1), 88. doi: 10.1186/1556-276X-8-88.

Liu, X.-K., Xu, W., Bai, S., Jin, Y., Wang, J., Friend, R. H. & Gao, F. Metal halide perovskites for light-emitting diodes. 1–12. doi: 10.1038/s41563-020-0784-7. Publisher: Nature Publishing Group.

Liu, Y., Li, F., Perumal Veeramalai, C., Chen, W., Guo, T., Wu, C. & Kim, T. W. Inkjet-Printed Photodetector Arrays Based on Hybrid Perovskite CH3NH3PbI3 Microwires. 9(13), 11662–11668. doi: 10.1021/acsami.7b01379. Publisher: American Chemical Society.

Loscertales, I. G., Barrero, A., Guerrero, I., Cortijo, R., Marquez, M. & Gañán-Calvo, A. M. Micro/Nano Encapsulation via Electrified Coaxial Liquid Jets. 295(5560), 1695–1698. doi: 10.1126/science.1067595. Publisher: American Association for the Advancement of Science.

Lossev, O. CII. Luminous carborundum detector and detection effect and oscillations with crystals. 6(39), 1024–1044. doi: 10.1080/14786441108564683.

Lu, L. P., Finlayson, C. E. & Friend, R. H. Thick polymer light-emitting diodes with very high power efficiency using Ohmic charge-injection layers. 29(2), 025005. doi: 10.1088/0268-1242/29/2/025005.

Lu, L.-P., Kabra, D., Johnson, K. & Friend, R. H. Charge-Carrier Balance and Color Purity in Polyfluorene Polymer Blends for Blue Light-Emitting Diodes. 22(1), 144–150. doi: https://doi.org/10.1002/adfm.201101892. _eprint: https://onlinelibrary.wiley.com/doi/pdf/10.1002/adfm.201101892.

Lv, Q.-J., Zhang, Y.-H., Zheng, C.-D., Gao, J.-D., Zhang, J.-L. & Liu, J.-L. Analysis of stress-induced inhomogeneous electroluminescence in GaN-based green LEDs grown on mesh-patterned Si (111) substrates with n-type AlGaN layer*. 29(8), 087801. doi: 10.1088/1674-1056/ab96a2. Publisher: Chinese Physical Society and IOP Publishing Ltd.

Ma, X. [Accepted: 2014-11-25T12:56:49Z]. Hybrid light emitting diodes based on solution processed polymers, colloidal quantum dots, and colloidal metal nanoparticles [Thesis]. University of Delaware. Retrieved on 2020-10-03 from: https://udspace.udel.edu/handle/19716/13404.

Ma, X., Benavides, J., Haughn, C. R., Xu, F., Doty, M. F. & Cloutier, S. G. High polymer-LEDs enhancement by exciton–plasmon coupling using encapsulated metallic nanoparticles. 7(14), 1916–1923. doi: 10.1016/j.orgel.2013.04.033.

Magdassi, S. *The Chemistry of Inkjet Inks*. WORLD SCIENTIFIC. doi: 10.1142/6869.

Mahbubul, I. M., Saidur, R. & Amalina, M. A. Latest developments on the viscosity of nanofluids. 55(4), 874–885. doi: 10.1016/j.ijheatmasstransfer.2011.10.021.

Majumder, M., Rendall, C. S., Eukel, J. A., Wang, J. Y. L., Behabtu, N., Pint, C. L., Liu, T.-Y., Orbaek, A. W., Mirri, F., Nam, J., Barron, A. R., Hauge, R. H., Schmidt, H. K. & Pasquali, M. Overcoming the "Coffee-Stain" Effect by Compositional Marangoni-Flow-Assisted Drop-Drying. 116(22), 6536–6542. doi: 10.1021/jp3009628. Publisher: American Chemical Society.

Maleki, H. & Bertola, V. Recent advances and prospects of inkjet printing in heterogeneous catalysis. 10(10), 3140–3159. doi: 10.1039/D0CY00040J. Publisher: Royal Society of Chemistry.

Malinkiewicz, O., Yella, A., Lee, Y. H., Espallargas, G. M., Graetzel, M., Nazeeruddin, M. K. & Bolink, H. J. Perovskite solar cells employing organic charge-transport layers. 8(2), 128–132. doi: 10.1038/nphoton.2013.341. Number: 2 Publisher: Nature Publishing Group.

Malliaras, G. G. & Scott, J. C. Numerical simulations of the electrical characteristics and the efficiencies of single-layer organic light emitting diodes. 85(10), 7426–7432. doi: 10.1063/1.369373. Publisher: American Institute of Physics.

Mampallil, D. & Eral, H. B. A review on suppression and utilization of the coffee-ring effect. 252, 38–54. doi: 10.1016/j.cis.2017.12.008.

Martin, G. D., Hoath, S. D. & Hutchings, I. M. Inkjet printing - the physics of manipulating liquid jets and drops. 105(1), 012001. doi: 10.1088/1742-6596/105/1/012001.

Martin, G. D. & Hutchings, I. M. Fundamentals of Inkjet Technology. In *Inkjet Technology for Digital Fabrication* (pp. 21–44). John Wiley & Sons, Ltd. doi: 10.1002/9781118452943.ch2.

Masood, M. T. Solution-Processable Compact and Mesoporous Titanium Dioxide Thin Films as Electron-Selective Layers for Perovskite Solar Cells [phdthesis].

Massa, G. D., Kim, H.-H., Wheeler, R. M. & Mitchell, C. A. Plant Productivity in Response to LED Lighting. 43(7), 1951–1956. doi: 10.21273/HORTSCI.43.7.1951. Publisher: American Society for Horticultural Science Section: HortScience.

Mattana, G., Loi, A., Woytasik, M., Barbaro, M., Noël, V. & Piro, B. Inkjet-Printing: A New Fabrication Technology for Organic Transistors. 2(10), 1700063. doi: 10.1002/admt.201700063. _eprint: https://onlinelibrary.wiley.com/doi/pdf/10.1002/admt.201700063.

mAuth1. (2001). mTit1. *mJour1*, 1(1), 42-43.

mAuth2. (2002). mTit2. *mJour2*, 2(2), 42-43.

McKinley, G. H. & Renardy, M. Wolfgang von Ohnesorge. 23(12), 127101. doi: 10.1063/1.3663616. Publisher: American Institute of Physics.

Medina Rodríguez, B. [Accepted: 2017-02-16T14:11:03Z Publication Title: TDX (Tesis Doctorals en Xarxa)]. Inkjet and screen printing for electronic applications [phdthesis]. Universitat de Barcelona. Retrieved on 2021-05-26 from: http://www.tdx.cat/handle/10803/400486.

Merdasa, A., Bag, M., Tian, Y., Källman, E., Dobrovolsky, A. & Scheblykin, I. G. Super-Resolution Luminescence Microspectroscopy Reveals the Mechanism of Photoinduced Degradation in CH3NH3PbI3 Perovskite Nanocrystals. 120(19), 10711–10719. doi: 10.1021/acs.jpcc.6b03512. Publisher: American Chemical Society.

Meskers, S. C. J., Duren, J. K. J. v., Janssen, R. a. J., Louwet, F. & Groenendaal, L. Infrared Detectors with Poly(3,4-ethylenedioxy thiophene)/Poly(styrene sulfonic acid) (PEDOT/PSS) as the Active Material. 15(7), 613–616. doi: 10.1002/adma.200304592. _eprint: https://onlinelibrary.wiley.com/doi/pdf/10.1002/adma.200304592.

Miao, J. & Zhang, F. Recent Progress on Photomultiplication Type Organic Photodetectors. 13(2), 1800204. doi: 10.1002/lpor.201800204. _eprint: https://onlinelibrary.wiley.com/doi/pdf/10.1002/lpor.201800204.

Miao, J., Hu, W., Jing, Y., Luo, W., Liao, L., Pan, A., Wu, S., Cheng, J., Chen, X. & Lu, W. Surface Plasmon-Enhanced Photodetection in Few Layer MoS2 Phototransistors with Au Nanostructure Arrays. 11(20), 2392–2398. doi: 10.1002/smll.201403422. _eprint: https://onlinelibrary.wiley.com/doi/pdf/10.1002/smll.201403422.

Mikhnenko, O. V., Blom, P. W. M. & Nguyen, T.-Q. Exciton diffusion in organic semiconductors. 8(7), 1867–1888. doi: 10.1039/C5EE00925A. Publisher: The Royal Society of Chemistry.

Mitzi, D. B., Feild, C. A., Harrison, W. T. A. & Guloy, A. M. Conducting tin halides with a layered organic-based perovskite structure. 369(6480), 467–469. doi: 10.1038/369467a0. Number: 6480 Publisher: Nature Publishing Group.

Miyazaki, H. & Koishikawa, Y. *patentus n°10026931B2*.

Mokhtari, F., Latifi, M. & Shamshirsaz, M. Electrospinning/electrospray of polyvinylidene fluoride (PVDF): piezoelectric nanofibers. 107(8), 1037–1055. doi: 10.1080/00405000.2015.1083300.

Morteani, A. C., Sreearunothai, P., Herz, L. M., Friend, R. H. & Silva, C. Exciton Regeneration at Polymeric Semiconductor Heterojunctions. 92(24), 247402. doi: 10.1103/PhysRevLett.92.247402. Publisher: American Physical Society.

Mueller, S., Llewellin, E. W. & Mader, H. M. The rheology of suspensions of solid particles. 466(2116), 1201–1228. doi: 10.1098/rspa.2009.0445. Publisher: Royal Society.

Muzzillo, C. P. Metal nano-grids for transparent conduction in solar cells. 169, 68–77. doi: 10.1016/j.solmat.2017.04.048.

Nakazawa, Y. K., Carter, S. A., Nothofer, H.-G., Scherf, U., Lee, V. Y., Miller, R. D. & Scott, J. C. Effects of polymer sidebranching in double- and single-layer polyfluorene light-emitting diodes. 80(20), 3832–3834. doi: 10.1063/1.1473692. Publisher: American Institute of Physics.

Nardelli, A., Deuschle, E., de Azevedo, L. D., Pessoa, J. L. N. & Ghisi, E. Assessment of Light Emitting Diodes technology for general lighting: A critical review. 75, 368–379. doi: 10.1016/j.rser.2016.11.002.

Nguyen, D. N., Clasen, C. & Van den Mooter, G. Pharmaceutical Applications of Electrospraying. 105(9), 2601–2620. doi: 10.1016/j.xphs.2016.04.024.

Nguyen, X. H., Luong, H. N., Pham, H. A., Nguyen, N. M. & Dang, V. Q. Visible photodetector based on transition metal-doped ZnO NRs/PEDOT:PSS hybrid materials. 11(57), 36340–36347. doi: 10.1039/d1ra06315d.

Noh, J. H., Im, S. H., Heo, J. H., Mandal, T. N. & Seok, S. I. Chemical Management for Colorful, Efficient, and Stable Inorganic–Organic Hybrid Nanostructured Solar Cells. 13(4), 1764–1769. doi: 10.1021/nl400349b. Publisher: American Chemical Society.

Nuyken, O., Jungermann, S., Wiederhirn, V., Bacher, E. & Meerholz, K. Modern Trends in Organic Light-Emitting Devices (OLEDs). 137(7), 811–824. doi: 10.1007/s00706-006-0490-4.

Organization name. (1999). *Norm title*. Institution and norm number. Location: Organization name.

Pan, H., Shao, H., Zhang, X. L., Shen, Y. & Wang, M. Interface engineering for high-efficiency perovskite solar cells. 129(13), 130904. doi: 10.1063/5.0038073. Publisher: American Institute of Physics.

Pan, J., Wei, C., Wang, L., Zhuang, J., Huang, Q., Su, W., Cui, Z., Nathan, A., Lei, W. & Chen, J. Boosting the efficiency of inverted quantum dot light-emitting diodes by balancing charge densities and suppressing exciton quenching through band alignment. 10(2), 592–602. doi: 10.1039/C7NR06248F. Publisher: The Royal Society of Chemistry.

Panahi, A., Pishevar, A. R. & Tavakoli, M. R. Experimental investigation of electrohydrodynamic modes in electrospraying of viscoelastic polymeric solutions. 32(1), 012116. doi: 10.1063/1.5132556. Publisher: American Institute of Physics.

Park, H., Chang, S., Zhou, X., Kong, J., Palacios, T. & Gradečak, S. Flexible Graphene Electrode-Based Organic Photovoltaics with Record-High Efficiency. 14(9), 5148–5154. doi: 10.1021/nl501981f. Publisher: American Chemical Society.

Park, N.-G. Perovskite solar cells: an emerging photovoltaic technology. 18(2), 65–72. doi: 10.1016/j.mattod.2014.07.007.

Partridge, R. H. *patentus n° 3995299A*.

Pelipenko, J., Kristl, J., Janković, B., Baumgartner, S. & Kocbek, P. The impact of relative humidity during electrospinning on the morphology and mechanical properties of nanofibers. 456(1), 125–134. doi: 10.1016/j.ijpharm.2013.07.078.

Pellet, N., Gao, P., Gregori, G., Yang, T.-Y., Nazeeruddin, M. K., Maier, J. & Grätzel, M. Mixed-Organic-Cation Perovskite Photovoltaics for Enhanced Solar-Light Harvesting. 53(12), 3151–3157. doi: https://doi.org/10.1002/anie.201309361. _eprint: https://onlinelibrary.wiley.com/doi/pdf/10.1002/anie.201309361.

Peng, H., Sun, X., Weng, W. & Fang, X. 7 - Light Emitting Based on Polymer. In Peng, H., Sun, X., Weng, W. & Fang, X. (Eds.), *Polymer Materials for Energy and Electronic Applications* (pp. 243–285). Academic Press. doi: 10.1016/B978-0-12-811091-1.00007-0.

Pitsalidis, C., Pappa, A. M., Hunter, S., Laskarakis, A., Kaimakamis, T., Payne, M. M., Anthony, J. E., Anthopoulos, T. D. & Logothetidis, S. High mobility transistors based on electrospray-printed small-molecule/polymer semiconducting blends. 4(16), 3499–3507. doi: 10.1039/C6TC00238B.

Pope, M. & Swenberg, C. E. *Electronic Processes in Organic Crystals and Polymers* (ed. Second Edition). Oxford University Press.

Protesescu, L., Yakunin, S., Bodnarchuk, M. I., Krieg, F., Caputo, R., Hendon, C. H., Yang, R. X., Walsh, A. & Kovalenko, M. V. Nanocrystals of Cesium Lead Halide Perovskites (CsPbX3, X = Cl, Br, and I): Novel Optoelectronic Materials Showing Bright Emission with Wide Color Gamut. 15(6), 3692–3696. doi: 10.1021/nl5048779. Publisher: American Chemical Society.

Pérez–Gutiérrez, E., Percino, M. J., Bernal, W., Cerón, M., Ceballos, P., Rivadeneyra, M. S., Siegler, M. A. & Thamotharan, S. Fluorescence tuning with a single dye embedded in a polymer matrix and its Application on multicolor OLEDs. 186, 108979. doi: 10.1016/j.dyepig.2020.108979.

Qu, D. Liu, F. Yu, J. Xie, W. Xu, Q. Li, X. & Huang, Y. Plasmonic core-shell gold nanoparticle enhanced optical absorption in photovoltaic devices. 98(11), 113119. doi: 10.1063/1.3559225. Publisher: American Institute of Physics.

Quan, L. N., Arquer, F. P. G. d., Sabatini, R. P. & Sargent, E. H. Perovskites for Light Emission. 30(45), 1801996. doi: 10.1002/adma.201801996.

Raengthon, N., McCue, C. & Cann, D. P. Relationship between tolerance factor and temperature coefficient of permittivity of temperature-stable high permittivity BaTiO3-Bi(Me)O3 compounds. 6, 1650002. doi: 10.1142/S2010135X16500028. ADS Bibcode: 2016JAdD....650002R.

Rahmani, S., Ashraf, S., Hartmann, R., Dishman, A. F., Zyuzin, M. V., Yu, C. K. J., Parak, W. J. & Lahann, J. Engineering of nanoparticle size via electrohydrodynamic jetting. 1(1), 82–93. doi: 10.1002/btm2.10010. _eprint: https://onlinelibrary.wiley.com/doi/pdf/10.1002/btm2.10010.

Raut, N. C. & Al-Shamery, K. Inkjet printing metals on flexible materials for plastic and paper electronics. 6(7), 1618–1641. doi: 10.1039/C7TC04804A. Publisher: The Royal Society of Chemistry.

Redecker, M., Bradley, D. D. C., Inbasekaran, M. & Woo, E. P. Nondispersive hole transport in an electroluminescent polyfluorene. 73(11), 1565–1567. doi: 10.1063/1.122205. Publisher: American Institute of Physics.

Reis, N. & Derby, B. Ink Jet Deposition of Ceramic Suspensions: Modeling and Experiments of Droplet Formation. 625. doi: 10.1557/PROC-625-117. Publisher: Cambridge University Press.

ReportLinker. Global Photodiode Sensors Market to Reach US$1.3 Billion by the Year 2026. Retrieved on 2022-10-23 from: https://www.globenewswire.com/news-release/2022/06/02/2455084/0/en/Global-Photodiode-Sensors-Market-to-Reach-US-1-3-Billion-by-the-Year-2026.html.

Rogalski, A. Infrared detectors: an overview. 43(3), 187–210. doi: 10.1016/S1350-4495(02)00140-8.

Ràfols-Ribé, J., Will, P.-A., Hänisch, C., Gonzalez-Silveira, M., Lenk, S., Rodríguez-Viejo, J. & Reineke, S. High-performance organic light-emitting diodes comprising ultrastable glass layers. 4(5). doi: 10.1126/sciadv.aar8332.

Röhr, J. A., Moia, D., Haque, S. A., Kirchartz, T. & Nelson, J. Exploring the validity and limitations of the Mott–Gurney law for charge-carrier mobility determination of semiconducting thin-films. 30(10), 105901. doi: 10.1088/1361-648X/aaabad. Publisher: IOP Publishing.

Sahu, N., Parija, B. & Panigrahi, S. Fundamental understanding and modeling of spin coating process: A review. 83(4), 493–502. doi: 10.1007/s12648-009-0009-z.

Sajid, M., Zubair, M., Doh, Y. H., Na, K.-H. & Choi, K. H. Flexible large area organic light emitting diode fabricated by electrohydrodynamics atomization technique. 26(9), 7192–7199. doi: 10.1007/s10854-015-3344-1.

Saliba, M., Matsui, T., Seo, J.-Y., Domanski, K., Correa-Baena, J.-P., Nazeeruddin, M. K., Zakeeruddin, S. M., Tress, W., Abate, A., Hagfeldt, A. & Grätzel, M. Cesium-containing triple cation perovskite solar cells: improved stability, reproducibility and high efficiency. 9(6), 1989–1997. doi: 10.1039/C5EE03874J. Publisher: The Royal Society of Chemistry.

Sampaio, P. G. V., González, M. O. A., de Oliveira Ferreira, P., da Cunha Jácome Vidal, P., Pereira, J. P. P., Ferreira, H. R. & Oprime, P. C. Overview of printing and coating techniques in the production of organic photovoltaic cells. 44(13), 9912–9931. doi: 10.1002/er.5664. _eprint: https://onlinelibrary.wiley.com/doi/pdf/10.1002/er.5664.

Santos, L. F. & Gozzi, G. Electrical Properties of Polymer Light-Emitting Devices. doi: 10.5772/64358. Publisher: IntechOpen.

Schiaffino, S. & Sonin, A. A. Formation and stability of liquid and molten beads on a solid surface. 343, 95–110. doi: 10.1017/S0022112097005831. Publisher: Cambridge University Press.

Schottky, W. Halbleitertheorie der Sperrschicht. 26(52), 843–843. doi: 10.1007/BF01774216.

Secor, E. B. & Hersam, M. C. Emerging Carbon and Post-Carbon Nanomaterial Inks for Printed Electronics. 6(4), 620–626. doi: 10.1021/jz502431r. Publisher: American Chemical Society.

Secor, E. B., Lim, S., Zhang, H., Frisbie, C. D., Francis, L. F. & Hersam, M. C. Gravure Printing of Graphene for Large-area Flexible Electronics. 26(26), 4533–4538. doi: 10.1002/adma.201401052. _eprint: https://onlinelibrary.wiley.com/doi/pdf/10.1002/adma.201401052.

Seeley, A. J. A. B. Light-emitting diodes from polyfluorenes: characterisation and stability of performance [Thesis]. University of Cambridge. Retrieved on 2020-03-04 from: https://www.repository.cam.ac.uk/handle/1810/241330.

Sellappan, R., Nielsen, M. G., González-Posada, F., Vesborg, P. C. K., Chorkendorff, I. & Chakarov, D. Effects of plasmon excitation on photocatalytic activity of Ag/TiO2 and Au/TiO2 nanocomposites. 307, 214–221. doi: 10.1016/j.jcat.2013.07.024.

Sette, D. Functional printing : from the study of printed layers to the prototyping of flexible devices [phdthesis]. Université de Grenoble. Retrieved on 2022-10-24 from: https://tel.archives-ouvertes.fr/tel-01152867.

Shafiee, A. & Atala, A. Printing Technologies for Medical Applications. 22(3), 254–265. doi: 10.1016/j.molmed.2016.01.003.

Shaheen, S. E., Radspinner, R., Peyghambarian, N. & Jabbour, G. E. Fabrication of bulk heterojunction plastic solar cells by screen printing. 79(18), 2996–2998. doi: 10.1063/1.1413501. Publisher: American Institute of Physics.

Shan, Q., Song, J., Zou, Y., Li, J., Xu, L., Xue, J., Dong, Y., Han, B., Chen, J. & Zeng, H. High Performance Metal Halide Perovskite Light-Emitting Diode: From Material Design to Device Optimization. 13(45), 1701770. doi: 10.1002/smll.201701770. _eprint: https://onlinelibrary.wiley.com/doi/pdf/10.1002/smll.201701770.

Shang, Q., Li, M., Zhao, L., Chen, D., Zhang, S., Chen, S., Gao, P., Shen, C., Xing, J., Xing, G., Shen, B., Liu, X. & Zhang, Q. Role of the Exciton–Polariton in a Continuous-Wave Optically Pumped CsPbBr3 Perovskite Laser. 20(9), 6636–6643. doi: 10.1021/acs.nanolett.0c02462. Publisher: American Chemical Society.

Shao, Y., Xiao, Z., Bi, C., Yuan, Y. & Huang, J. Origin and elimination of photocurrent hysteresis by fullerene passivation in CH3NH3PbI3 planar heterojunction solar cells. 5(1), 5784. doi: 10.1038/ncomms6784. Number: 1 Publisher: Nature Publishing Group.

Sharma, B. L. *Metal-Semiconductor Schottky Barrier Junctions and Their Applications*. Springer Science & Business Media.

Shen, T., Yuan, J., Zhong, X. & Tian, J. Dip-coated colloidal quantum-dot films for high-performance broadband photodetectors. 7(21), 6266–6272. doi: 10.1039/C9TC00079H. Publisher: The Royal Society of Chemistry.

Sima, C., Grigoriu, C. & Antohe, S. Comparison of the dye-sensitized solar cells performances based on transparent conductive ITO and FTO. 519(2), 595–597. doi: 10.1016/j.tsf.2010.07.002.

Singh, M., Haverinen, H. M., Dhagat, P. & Jabbour, G. E. Inkjet Printing—Process and Its Applications. 22(6), 673–685. doi: 10.1002/adma.200901141. _eprint: https://onlinelibrary.wiley.com/doi/pdf/10.1002/adma.200901141.

Sirringhaus, H. & Shimoda, T. Inkjet Printing of Functional Materials. 28(11), 802–806. doi: 10.1557/mrs2003.228.

Soltman, D. & Subramanian, V. Inkjet-printed line morphologies and temperature control of the coffee ring effect. 24(5), 2224–2231. doi: 10.1021/la7026847.

Song, H. J., Kim, D. H., Lee, T. H. & Moon, D. K. Emission color tuning of copolymers containing polyfluorene, benzothiadiazole, porphyrin derivatives. 48(8), 1485–1494. doi: 10.1016/j.eurpolymj.2012.06.002.

Stolterfoht, M., Wolff, C. M., Amir, Y., Paulke, A., Perdigón-Toro, L., Caprioglio, P. & Neher, D. Approaching the fill factor Shockley–Queisser limit in stable, dopant-free triple cation perovskite solar cells. 10(6), 1530–1539. doi: 10.1039/C7EE00899F. Publisher: The Royal Society of Chemistry.

Stoumpos, C. C. & Kanatzidis, M. G. The Renaissance of Halide Perovskites and Their Evolution as Emerging Semiconductors. 48(10), 2791–2802. doi: 10.1021/acs.accounts.5b00229. Publisher: American Chemical Society.

Stoumpos, C. C., Malliakas, C. D. & Kanatzidis, M. G. Semiconducting Tin and Lead Iodide Perovskites with Organic Cations: Phase Transitions, High Mobilities, and Near-Infrared Photoluminescent Properties. 52(15), 9019–9038. doi: 10.1021/ic401215x. Publisher: American Chemical Society.

Stow, C. D., Hadfield, M. G. & Ziman, J. M. An experimental investigation of fluid flow resulting from the impact of a water drop with an unyielding dry surface. 373(1755), 419–441. doi: 10.1098/rspa.1981.0002. Publisher: Royal Society.

Suganuma, K. Printing Technology. In Suganuma, K. (Ed.), *Introduction to Printed Electronics* (pp. 23–48). Springer. doi: 10.1007/978-1-4614-9625-0_2.

Sum, T. C. & Mathews, N. *Halide Perovskites: Photovoltaics, Light Emitting Devices, and Beyond*. WILEY-VCH.

Sun, X., Asadpour, R., Nie, W., Mohite, A. D. & Alam, M. A. A Physics-Based Analytical Model for Perovskite Solar Cells. 5(5), 1389–1394. doi: 10.1109/JPHOTOV.2015.2451000. Conference Name: IEEE Journal of Photovoltaics.

Sunaoshi, T., Kaji, K., Orai, Y., Schamp, C. & Voelkl, E. STEM/SEM, Chemical Analysis, Atomic Resolution and Surface Imaging At 30 kV with No Aberration Correction for Nanomaterials on Graphene Support. 22, 604–605. doi: 10.1017/S1431927616003871.

Sundararaman, R., Narang, P., Jermyn, A. S., Goddard Iii, W. A. & Atwater, H. A. Theoretical predictions for hot-carrier generation from surface plasmon decay. 5(1), 5788. doi: 10.1038/ncomms6788. Number: 1 Publisher: Nature Publishing Group.

Sundriyal, P. & Bhattacharya, S. Inkjet-Printed Electrodes on A4 Paper Substrates for Low-Cost, Disposable, and Flexible Asymmetric Supercapacitors. 9(44), 38507–38521. doi: 10.1021/acsami.7b11262. Publisher: American Chemical Society.

Surendran, A., Yu, X., Begum, R., Tao, Y., Wang, Q. J. & Leong, W. L. All Inorganic Mixed Halide Perovskite Nanocrystal–Graphene Hybrid Photodetector: From Ultrahigh Gain to Photostability. 11(30), 27064–27072. doi: 10.1021/acsami.9b06416. Publisher: American Chemical Society.

Sutherland, B. R. & Sargent, E. H. Perovskite photonic sources. 10(5), 295–302. doi: 10.1038/nphoton.2016.62.

Svane, K. L., Forse, A. C., Grey, C. P., Kieslich, G., Cheetham, A. K., Walsh, A. & Butler, K. T. How Strong Is the Hydrogen Bond in Hybrid Perovskites? 8(24), 6154–6159. doi: 10.1021/acs.jpclett.7b03106. Publisher: American Chemical Society.

Sze, S. & Lee, M. *Semiconductor Devices Physics and Technology*. John Wiley & Sons, Ltd. Retrieved from: https://pd-zdh.xaut.edu.cn/__local/A/F0/D3/EA002AB461DFDFC92BCFAD35BC4_C62E9AA9_1335DE9.pdf.

Szuromi, P. & Grocholski, B. Natural and engineered perovskites. 358(6364), 732–733. doi: 10.1126/science.358.6364.732. Publisher: American Association for the Advancement of Science Section: Introduction to special issue.

Sındıraç, C. & Akkurt, S. Microstructural investigation of the effect of electrospraying parameters on LSCF films. 45(60), 35139–35148. doi: 10.1016/j.ijhydene.2020.02.194.

Tan, Z.-K., Moghaddam, R. S., Lai, M. L., Docampo, P., Higler, R., Deschler, F., Price, M., Sadhanala, A., Pazos, L. M., Credgington, D., Hanusch, F., Bein, T., Snaith, H. J. & Friend, R. H. Bright light-emitting diodes based on organometal halide perovskite. 9(9), 687–692. doi: 10.1038/nnano.2014.149.

Tang, C. W. & VanSlyke, S. A. Organic electroluminescent diodes. 51(12), 913–915. doi: 10.1063/1.98799. Publisher: American Institute of Physics.

Tasch, S., List, E. J. W., Ekström, O., Graupner, W., Leising, G., Schlichting, P., Rohr, U., Geerts, Y., Scherf, U. & Müllen, K. Efficient white light-emitting diodes realized with new processable blends of conjugated polymers. 71(20), 2883–2885. doi: 10.1063/1.120205. Publisher: American Institute of Physics.

Taylor, G. I. Disintegration of water drops in an electric field. 280(1382), 383–397. doi: 10.1098/rspa.1964.0151. Publisher: Royal Society.

Tong, S., Gong, C., Zhang, C., Liu, G., Zhang, D., Zhou, C., Sun, J., Xiao, S., He, J., Gao, Y. & Yang, J. Fully-printed, flexible cesium-doped triple cation perovskite photodetector. 15, 389–397. doi: 10.1016/j.apmt.2019.03.001.

Tsai, H., Nie, W., Cheruku, P., Mack, N. H., Xu, P., Gupta, G., Mohite, A. D. & Wang, H.-L. Optimizing Composition and Morphology for Large-Grain Perovskite Solar Cells via Chemical Control. 27(16), 5570–5576. doi: 10.1021/acs.chemmater.5b02378. Publisher: American Chemical Society.

Tseng, H.-Y. Scaling of Inkjet-Printed Transistors using Novel Printing Techniques [phdthesis]. UC Berkeley. Retrieved on 2021-05-26 from: https://escholarship.org/uc/item/6wx787mp.

Tseng, S.-R., Lin, S.-C., Meng, H.-F., Liao, H.-H., Yeh, C.-H., Lai, H.-C., Horng, S.-F. & Hsu, C.-S. General method to solution-process multilayer polymer light-emitting diodes. 88(16), 163501. doi: 10.1063/1.2192574.

Tucker, N., Stanger, J. J., Staiger, M. P., Razzaq, H. & Hofman, K. The History of the Science and Technology of Electrospinning from 1600 to 1995. 7(2), 155892501200702S10. doi: 10.1177/155892501200702S10. Publisher: SAGE Publications Ltd STM.

Umebayashi, T., Asai, K., Kondo, T. & Nakao, A. Electronic structures of lead iodide based low-dimensional crystals. 67(15), 155405. doi: 10.1103/PhysRevB.67.155405. Publisher: American Physical Society.

Van Le, Q., Jang, H. W. & Kim, S. Y. Recent Advances toward High-Efficiency Halide Perovskite Light-Emitting Diodes: Review and Perspective. 2(10), 1700419. doi: 10.1002/smtd.201700419. _eprint: https://onlinelibrary.wiley.com/doi/pdf/10.1002/smtd.201700419.

vanOsch, T. H. J., Perelaer, J., deLaat, A. W. M. & Schubert, U. S. Inkjet Printing of Narrow Conductive Tracks on Untreated Polymeric Substrates. 20(2), 343–345. doi: https://doi.org/10.1002/adma.200701876. _eprint: https://onlinelibrary.wiley.com/doi/pdf/10.1002/adma.200701876.

Vashishtha, P., Bishnoi, S., Li, C.-H. A., Jagadeeswararao, M., Hooper, T. J. N., Lohia, N., Shivarudraiah, S. B., Ansari, M. S., Sharma, S. N. & Halpert, J. E. Recent Advancements in Near-Infrared Perovskite Light-Emitting Diodes. 2(11), 3470–3490. doi: 10.1021/acsaelm.0c00825. Publisher: American Chemical Society.

Vashishtha, P., Veldhuis, S. A., Dintakurti, S. S. H., Kelly, N. L., Griffith, B. E., Brown, A. A. M., Ansari, M. S., Bruno, A., Mathews, N., Fang, Y., White, T., Mhaisalkar, S. G. & Hanna, J. V. Investigating the structure–function relationship in triple cation perovskite nanocrystals for light-emitting diode applications. 8(34), 11805–11821. doi: 10.1039/D0TC02038A. Publisher: The Royal Society of Chemistry.

Veinot, J. G. C. & Marks, T. J. Toward the Ideal Organic Light-Emitting Diode. The Versatility and Utility of Interfacial Tailoring by Cross-Linked Siloxane Interlayers. 38(8), 632–643. doi: 10.1021/ar030210r. Publisher: American Chemical Society.

Vuuren, R. D. J.-v., Armin, A., Pandey, A. K., Burn, P. L. & Meredith, P. Organic Photodiodes: The Future of Full Color Detection and Image Sensing. 28(24), 4766–4802. doi: 10.1002/adma.201505405. _eprint: https://onlinelibrary.wiley.com/doi/pdf/10.1002/adma.201505405.

Waasdorp, R., Heuvel, O. v. d., Versluis, F., Hajee, B. & Ghatkesar, M. K. Accessing individual 75-micron diameter nozzles of a desktop inkjet printer to dispense picoliter droplets on demand. 8(27), 14765–14774. doi: 10.1039/C8RA00756J. Publisher: The Royal Society of Chemistry.

Waltman, R. J., Bargon, J. & Diaz, A. F. Electrochemical studies of some conducting polythiophene films. 87(8), 1459–1463. doi: 10.1021/j100231a035. Publisher: American Chemical Society.

Wang, C., Zhang, C., Wang, S., Liu, G., Xia, H., Tong, S., He, J., Niu, D., Zhou, C., Ding, K., Gao, Y. & Yang, J. Low-Temperature Processed, Efficient, and Highly Reproducible Cesium-Doped Triple Cation Perovskite Planar Heterojunction Solar Cells. 2(2), 1700209. doi: 10.1002/solr.201700209. _eprint: https://onlinelibrary.wiley.com/doi/pdf/10.1002/solr.201700209.

Wang, H., Zhang, X., Wu, Q., Cao, F., Yang, D., Shang, Y., Ning, Z., Zhang, W., Zheng, W., Yan, Y., Kershaw, S. V., Zhang, L., Rogach, A. L. & Yang, X. Trifluoroacetate induced small-grained CsPbBr 3 perovskite films result in efficient and stable light-emitting devices. 10(1), 665. doi: 10.1038/s41467-019-08425-5. Number: 1 Publisher: Nature Publishing Group.

Wang, L., Li, Z., Li, M., Li, S., Lu, Y., Qi, N., Zhang, J., Xie, C., Wu, C. & Luo, L.-B. Self-Powered Filterless Narrow-Band p–n Heterojunction Photodetector for Low

Background Limited Near-Infrared Image Sensor Application. 12(19), 21845–21853. doi: 10.1021/acsami.0c02827. Publisher: American Chemical Society.

Wang, N., Cheng, L., Ge, R., Zhang, S., Miao, Y., Zou, W., Yi, C., Sun, Y., Cao, Y., Yang, R., Wei, Y., Guo, Q., Ke, Y., Yu, M., Jin, Y., Liu, Y., Ding, Q., Di, D., Yang, L., Xing, G., Tian, H., Jin, C., Gao, F., Friend, R. H., Wang, J. & Huang, W. Perovskite light-emitting diodes based on solution-processed self-organized multiple quantum wells. 10(11), 699–704. doi: 10.1038/nphoton.2016.185.

Wang, S., Li, X., Wu, J., Wen, W. & Qi, Y. Fabrication of efficient metal halide perovskite solar cells by vacuum thermal evaporation: A progress review. 11, 130–140. doi: 10.1016/j.coelec.2018.10.006.

Wang, Y., Wu, J., Zhang, P., Liu, D., Zhang, T., Ji, L., Gu, X., David Chen, Z. & Li, S. Stitching triple cation perovskite by a mixed anti-solvent process for high performance perovskite solar cells. 39, 616–625. doi: 10.1016/j.nanoen.2017.07.046.

Wannier, G. H. The Structure of Electronic Excitation Levels in Insulating Crystals. 52(3), 191–197. doi: 10.1103/PhysRev.52.191. Publisher: American Physical Society.

Weber, D. CH3NH3PbX3, ein Pb(II)-System mit kubischer Perowskitstruktur / CH3NH3PbX3, a Pb(II)-System with Cubic Perovskite Structure. 33(12), 1443–1445. doi: 10.1515/znb-1978-1214. Publisher: Verlag der Zeitschrift für Naturforschung Section: Zeitschrift für Naturforschung B.

Wei, Q., Ge, Z. & Voit, B. Thermally Activated Delayed Fluorescent Polymers: Structures, Properties, and Applications in OLED Devices. 40(1), 1800570. doi: 10.1002/marc.201800570.

Wei, Z., Zhao, Y., Jiang, J., Yan, W., Feng, Y. & Ma, J. Research progress on hybrid organic–inorganic perovskites for photo-applications. 31(12), 3055–3064. doi: 10.1016/j.cclet.2020.05.016.

Wenk, H.-R. & Bulakh, A. *Minerals: Their Constitution and Origin*. Cambridge University Press.

Whitfield, P. S., Herron, N., Guise, W. E., Page, K., Cheng, Y. Q., Milas, I. & Crawford, M. K. Structures, Phase Transitions and Tricritical Behavior of the Hybrid Perovskite Methyl Ammonium Lead Iodide. 6(1), 35685. doi: 10.1038/srep35685. Number: 1 Publisher: Nature Publishing Group.

Page title. (1999a). In *Wikipedia*. Retrieved on 2013-05-16 from: https://www.wikipedia.org.

Page title. (1999b). In *Wikipedia*. Retrieved on 2013-05-16 from: https://www.wikipedia.org.

Wilhelm, O., Mädler, L. & Pratsinis, S. E. (2003). Electrospray evaporation and deposition. *Journal of Aerosol Science*, 34(7), 815–836. doi: 10.1016/S0021-8502(03)00034-X.

Williams, P. The sputtering process and sputtered ion emission. 90(2), 588–634. doi: 10.1016/0039-6028(79)90363-7.

Wu, I.-W., Chen, Y.-H., Wang, P.-S., Wang, C.-G., Hsu, S.-H. & Wu, C.-I. Correlation of energy band alignment and turn-on voltage in organic light emitting diodes. 96(1), 013301. doi: 10.1063/1.3282682. Publisher: American Institute of Physics.

Wu, M.-J., Kuo, C.-C., Jhuang, L.-S., Chen, P.-H., Lai, Y.-F. & Chen, F.-C. Bandgap Engineering Enhances the Performance of Mixed-Cation Perovskite Materials for Indoor Photovoltaic Applications. 9(37), 1901863. doi: https://doi.org/10.1002/aenm.201901863. _eprint: https://onlinelibrary.wiley.com/doi/pdf/10.1002/aenm.201901863.

Wu, Y. & Clark, R. L. Controllable porous polymer particles generated by electrospraying. 310(2), 529–535. doi: 10.1016/j.jcis.2007.02.023.

Xiao, Z., Kerner, R. A., Zhao, L., Tran, N. L., Lee, K. M., Koh, T.-W., Scholes, G. D. & Rand, B. P. Efficient perovskite light-emitting diodes featuring nanometre-sized crystallites. 11(2), 108–115. doi: 10.1038/nphoton.2016.269.

Xie, J., Jiang, J., Davoodi, P., Srinivasan, M. P. & Wang, C.-H. Electrohydrodynamic atomization: A two-decade effort to produce and process micro-/nanoparticulate materials. 125, 32–57. doi: 10.1016/j.ces.2014.08.061.

Xing, S. Chapter 10 - Nanomaterials of conducting polymers and its application in energy conversion and storage. In Ran, F. & Chen, S. (Eds.), *Advanced Nanomaterials for Electrochemical-Based Energy Conversion and Storage* (pp. 325–354). Elsevier. doi: 10.1016/B978-0-12-814558-6.00010-1.

Xiong, Z. & Liu, C. Optimization of inkjet printed PEDOT:PSS thin films through annealing processes. 9(13), 1532–1540. doi: 10.1016/j.orgel.2012.05.005.

Xu, W., Hu, Q., Bai, S., Bao, C., Miao, Y., Yuan, Z., Borzda, T., Barker, A. J., Tyukalova, E., Hu, Z., Kawecki, M., Wang, H., Yan, Z., Liu, X., Shi, X., Uvdal, K., Fahlman, M., Zhang, W., Duchamp, M., Liu, J.-M., Petrozza, A., Wang, J., Liu, L.-M., Huang, W. & Gao, F. Rational molecular passivation for high-performance perovskite light-emitting diodes. 13(6), 418–424. doi: 10.1038/s41566-019-0390-x. Number: 6 Publisher: Nature Publishing Group.

Yan, H., Huang, Q., Cui, J., Veinot, J., Kern, M. & Marks, T. High-Brightness Blue Light-Emitting Polymer Diodes via Anode Modification Using a Self-Assembled Monolayer. 15(10), 835–838. doi: 10.1002/adma.200304585.

Yang, B., Zhang, F., Chen, J., Yang, S., Xia, X., Pullerits, T., Deng, W. & Han, K. Ultrasensitive and Fast All-Inorganic Perovskite-Based Photodetector via Fast Carrier Diffusion. 29(40), 1703758. doi: 10.1002/adma.201703758. _eprint: https://onlinelibrary.wiley.com/doi/pdf/10.1002/adma.201703758.

Yang, H., Zhang, J., Zhang, C., Chang, J., Lin, Z., Chen, D., Xi, H. & Hao, Y. Effects of Annealing Conditions on Mixed Lead Halide Perovskite Solar Cells and Their Thermal Stability Investigation. 10(7). doi: 10.3390/ma10070837.

Yang, M., Han, Q., Liu, X., Han, J., Zhao, Y., He, L., Gou, J., Wu, Z., Wang, X. & Wang, J. Ultrahigh Stability 3D TI Bi2Se3/MoO3 Thin Film Heterojunction Infrared Photodetector at Optical Communication Waveband. 30(12), 1909659. doi: 10.1002/adfm.201909659. _eprint: https://onlinelibrary.wiley.com/doi/pdf/10.1002/adfm.201909659.

Yang, Z., Babu, B. H., Wu, S., Liu, T., Fang, S., Xiong, Z., Han, L. & Chen, W. Review on Practical Interface Engineering of Perovskite Solar Cells: From Efficiency to Stability. 4(2), 1900257. doi: https://doi.org/10.1002/solr.201900257. _eprint: https://onlinelibrary.wiley.com/doi/pdf/10.1002/solr.201900257.

Yao, J., Kuang Lim, L., Xie, J., Hua, J. & Wang, C.-H. Characterization of electrospraying process for polymeric particle fabrication. 39(11), 987–1002. doi: 10.1016/j.jaerosci.2008.07.003.

Yarin, A. L., Koombhongse, S. & Reneker, D. H. Taylor cone and jetting from liquid droplets in electrospinning of nanofibers. 90(9), 4836–4846. doi: 10.1063/1.1408260. Publisher: American Institute of Physics.

Yi, C., Luo, J., Meloni, S., Boziki, A., Ashari-Astani, N., Grätzel, C., Zakeeruddin, S. M., Röthlisberger, U. & Grätzel, M. Entropic stabilization of mixed A-cation ABX3 metal halide perovskites for high performance perovskite solar cells. 9(2), 656–662. doi: 10.1039/C5EE03255E. Publisher: The Royal Society of Chemistry.

Yin, W.-J., Yang, J.-H., Kang, J., Yan, Y. & Wei, S.-H. Halide perovskite materials for solar cells: a theoretical review. 3(17), 8926–8942. doi: 10.1039/C4TA05033A. Publisher: The Royal Society of Chemistry.

Yin, Z., Huang, Y., Bu, N., Wang, X. & Xiong, Y. Inkjet printing for flexible electronics: Materials, processes and equipments. 55(30), 3383–3407. doi: 10.1007/s11434-010-3251-y.

Yu, D. X. Light-Emitting Devices with Conjugated Polymers. 12(3), 1575–1594. doi: 10.3390/ijms12031575.

Yu, X., Marks, T. J. & Facchetti, A. Metal oxides for optoelectronic applications. 15(4), 383–396. doi: 10.1038/nmat4599. Number: 4 Publisher: Nature Publishing Group.

Yuan, D.-X., Yuan, X.-D., Xu, Q.-Y., Xu, M.-F., Shi, X.-B., Wang, Z.-K. & Liao, L.-S. A solution-processed bathocuproine cathode interfacial layer for high-performance bromine–iodine perovskite solar cells. 17(40), 26653–26658. doi: 10.1039/C5CP03995A. Publisher: The Royal Society of Chemistry.

Zavanelli, N., Kim, J. & Yeo, W.-H. Recent Advances in High-Throughput Nanomaterial Manufacturing for Hybrid Flexible Bioelectronics. 14(11), 2973. doi: 10.3390/ma14112973. Number: 11 Publisher: Multidisciplinary Digital Publishing Institute.

Zeleny, J. The Electrical Discharge from Liquid Points, and a Hydrostatic Method of Measuring the Electric Intensity at Their Surfaces. 3(2), 69–91. doi: 10.1103/PhysRev.3.69.

Zhang, C., Kuang, D.-B. & Wu, W.-Q. A Review of Diverse Halide Perovskite Morphologies for Efficient Optoelectronic Applications. 4(2), 1900662. doi: https://doi.org/10.1002/smtd.201900662. _eprint: https://onlinelibrary.wiley.com/doi/pdf/10.1002/smtd.201900662.

Zhang, S. B. & Wei, S.-H. Surface Energy and the Common Dangling Bond Rule for Semiconductors. 92(8), 086102. doi: 10.1103/PhysRevLett.92.086102. Publisher: American Physical Society.

Zhang, W., Eperon, G. E. & Snaith, H. J. Metal halide perovskites for energy applications. 1(6), 1–8. doi: 10.1038/nenergy.2016.48. Number: 6 Publisher: Nature Publishing Group.

Zhang, Y., Hu, G., Liu, Y., Wang, J., Yang, G. & Li, D. Suppression and Utilization of Satellite Droplets for Inkjet Printing: A Review. 10(5), 932. doi: 10.3390/pr10050932. Number: 5 Publisher: Multidisciplinary Digital Publishing Institute.

Zhang, Y.-Y., Chen, S., Xu, P., Xiang, H., Gong, X.-G., Walsh, A. & Wei, S.-H. Intrinsic Instability of the Hybrid Halide Perovskite Semiconductor CH 3 NH 3 PbI 3 \ast. 35(3), 036104. doi: 10.1088/0256-307X/35/3/036104. Publisher: IOP Publishing.

Zhao, L., Lee, K. M., Roh, K., Khan, S. U. Z. & Rand, B. P. Improved Outcoupling Efficiency and Stability of Perovskite Light-Emitting Diodes using Thin Emitting Layers. 31(2), 1805836. doi: 10.1002/adma.201805836.

Zhao, L., Rolston, N., Lee, K. M., Zhao, X., Reyes-Martinez, M. A., Tran, N. L., Yeh, Y.-W., Yao, N., Scholes, G. D., Loo, Y.-L., Selloni, A., Dauskardt, R. H. & Rand, B. P. Influence of Bulky Organo-Ammonium Halide Additive Choice on the Flexibility and Efficiency of Perovskite Light-Emitting Devices. 28(31), 1802060. doi: 10.1002/adfm.201802060.

Zhao, X. & Tan, Z.-K. Large-area near-infrared perovskite light-emitting diodes. 14(4), 215–218. doi: 10.1038/s41566-019-0559-3. Number: 4 Publisher: Nature Publishing Group.

Zhao, Y., Li, C. & Shen, L. Recent advances on organic-inorganic hybrid perovskite photodetectors with fast response. 1(2), 164–182. doi: 10.1002/inf2.12010. _eprint: https://onlinelibrary.wiley.com/doi/pdf/10.1002/inf2.12010.

Zhao, Z., Xu, C., Niu, L., Zhang, X. & Zhang, F. Recent Progress on Broadband Organic Photodetectors and their Applications. 14(11), 2000262. doi: 10.1002/lpor.202000262. _eprint: https://onlinelibrary.wiley.com/doi/pdf/10.1002/lpor.202000262.

Zheng, H., Zheng, Y., Liu, N., Ai, N., Wang, Q., Wu, S., Zhou, J., Hu, D., Yu, S., Han, S., Xu, W., Luo, C., Meng, Y., Jiang, Z., Chen, Y., Li, D., Huang, F., Wang, J., Peng, J. & Cao, Y. All-solution processed polymer light-emitting diode displays. 4, 1971. doi: 10.1038/ncomms2971.

Zheng, H., Zheng, Y., Wang, J., Wang, J., Zhang, G., Zhang, S., Liu, M., Hu, J., Li, Y., Hu, Y. & Zhang, W. Polymer light-emitting displays with printed cathodes. 358, 228–234. doi: 10.1016/j.surfcoat.2018.11.041.

Zheng, X., Wu, C., Jha, S. K., Li, Z., Zhu, K. & Priya, S. Improved Phase Stability of Formamidinium Lead Triiodide Perovskite by Strain Relaxation. 1(5), 1014–1020. doi: 10.1021/acsenergylett.6b00457. Publisher: American Chemical Society.

Zhou, S., Tang, R. & Yin, L. Slow-Photon-Effect-Induced Photoelectrical-Conversion Efficiency Enhancement for Carbon-Quantum-Dot-Sensitized Inorganic CsPbBr3 Inverse Opal Perovskite Solar Cells. 29(43), 1703682. doi: 10.1002/adma.201703682. _eprint: https://onlinelibrary.wiley.com/doi/pdf/10.1002/adma.201703682.

Zhou, Z.-L., Sheng, X., Nauka, K., Zhao, L., Gibson, G., Lam, S., Yang, C. C., Brug, J. & Elder, R. Multilayer structured polymer light emitting diodes with cross-linked polymer matrices. 96(1), 013504. doi: 10.1063/1.3284649.

Zhu, L., Yi, Y., Chen, L. & Shuai, Z. Exciton binding energy of electronic polymers: A first principles study. 07. doi: 10.1142/S0219633608003939.

Zhu, W., Masood, F., O'Brien, J. & Zhang, L. G. Highly aligned nanocomposite scaffolds by electrospinning and electrospraying for neural tissue regeneration. 11(3), 693–704. doi: 10.1016/j.nano.2014.12.001.